Investigation of Cemented Rockfill Properties Used at a Canadian Diamond Mine

By

Bob Andrea Lingga

A thesis submitted in partial fulfillment of the requirements for the degree of

Master of Science

in

Mining Engineering

Department of Civil and Environmental Engineering

University of Alberta

Abstract

Backfill utilization has been necessary for underground mining practices ever since the scarcity of economic minerals near ground surface started shallow underground mining. Economic factors inevitably realized this condition. Mine waste disposal and ground support means led to backfill utilization as a regular part of underground mining. Therefore, a study about backfill has the potential to keep the mining industry economically efficient.

As an underground mining support, suppose backfill strengths and related properties are the determining parameters that are firstly considered in an underground mining support design with backfill application. Cemented rockfill as one type of backfill distinguishes its prospective potential from other types of cemented backfills because of its higher strength of nature.

One underground mine in Northern Canada has presented the opportunity to study the cemented rockfill property of granite. In this research, the laboratory scale of cemented rockfill of granite was examined experimentally through unconfined compressive strength, splitting tensile strength, direct shear, and triaxial tests. As a result, complete strengths, elasticity, and shear properties of this particular granite cemented rockfill were obtained and are presented in this thesis. The completion of this part of the research work is expected to contribute toward cemented rockfill development of the Canadian mining sector, particularly with regard to diamond mines.

In addition, this research also uses an unconventional testing technique and practical approach to give a new perspective on producing qualitative data from large-scale cemented rockfill samples due to testing impediment normally because of the standard large size of specimens. Therefore, perhaps the finding from these two works could be of use not only to granite cemented rockfill research but to backfill research in general.

Preface

This thesis is an original work by Bob Andrea Lingga. All of the research conducted for this thesis has been conducted within the Department of Civil and Environmental Engineering under the School of Mining, University of Alberta, with Professor Derek Apel being the lead collaborator and Jan Romanowski from Rio Tinto's Diavik Diamond Mine as the industrial source. The technical apparatus referred to in Chapter 5, the shear testing apparatus, was rebuilt by myself and the triaxial apparatus newly fabricated by the competent manufacturer RocTest Company, all with the assistance and support of Professor Derek Apel.

Chapter 3 of this thesis has been submitted as B.A. Lingga, D. Apel, M. Sepehri, and X. Huawei, "Compressive and Tensile Strength Development Based on Early Age of Laboratory Scale Cemented Rockfill Used at a Canadian Diamond Mine," *International Journal of Mining and Mineral Engineering*, Submission code: IJMME-202427. **Chapter 4** of this thesis has been submitted as B.A. Lingga, D. Apel, M. Sepehri, and Y. Pu, "Assessment of Digital Image Correlation Method in Determining Elastic Properties of Large Scale Cemented Rockfill Samples," *International Journal of Mining Science and Technology*, Submission no: IJMST_2017_624. **Chapter 5** of this thesis has also been prepared and will be submitted in the meantime, with the prepared title "Study of Shear Properties on Cemented Rockfill." I was responsible for the data collection and analysis as well as the manuscript composition. Y. Pu and H. Xu assisted with the data collection. M. Sepehri contributed to manuscript edits. D. Apel was the supervisory author and was involved with concept formation and manuscript composition.

Acknowledgements

I would like to express my gratitude to my supervisor, Dr. Derek Apel, who gave me the precious opportunity to pursue my graduate study under his guidance. I came to know so many new things because of his encouragement and unlimited time provided for sharing, discussing, and solving any obstacle and in this research.

I would like to thank Dr. Mohammadali Sepehri for being a mentor and advisor who provided valuable discussions and technical guidance, which also helped me in doing my research. It is also worthwhile to mention my fellow research colleagues Xu Huawei and Yuanyuan Pu; my thanks go out to you.

Many thanks also to Mr. Jan Romanowski from Rio Tinto's Diavik Diamond Mine as the industrial source, enabling me to produce this particular thesis.

I would like to give my appreciation to all the laboratory staff of Civil and Environmental Engineering at the University of Alberta who devoted their help and attention to every aspect of my research activities in the laboratory: Rizaldy Mariano, Greg Miller, Cameron West, and Lucas Duerksen.

My deep appreciation goes to Dr. Ridho Kresna Wattimena, who is my inspiration and always will be. Thank you for being my former supervisor during my research in my undergraduate degree, introducing me to the rock mechanics world, and allowing me to attend your classes even after I was not a student anymore.

I gratefully acknowledge the funding received toward my MSc from the Indonesia Endowment Fund for Education (LPDP) scholarship. This study would not have been possible without the

professional and remarkable care provided by the scholarship council towards financially supporting my study.

And finally to my family: my parents, brothers, and sister who have been by my side throughout my studies, thank you for believing in me and for your boundless love and support. I dedicate this thesis especially to you.

Table of Contents

List of Figures

List of Tables

Chapter 1: Introduction

Backfilling is a part of mining activities which has actually been in existence for thousands of years, first described as waste rock being thrown into the openings surrounded by timber in the classic Latin manuscript "*De Re Metallica*" by Agricola (1494-1555, 1950). Rather than used as support, the aforementioned backfill back in those days was evidently used only for disposal purposes. Mining today has still been running moreover growing as a giant industry sector regardless of the fixed available resources. Accordingly, the advancement of mining progress is inevitably going deeper from the surface. Furthermore, the evolution of backfilling itself from only being used for disposal purposes has advanced to become a means of support. Hence, the properties of backfill are of interest, because these properties are the fundamental aspects to consider when initiating any related stability work.

The mining sector in Canada produces approximately 500 million tonnes of tailings and waste rock annually (Amaratunga & Yaschyshyn, 1997); there have been several studies about cemented rockfill (CRF) as the backfill material in many Canadian mines (Emad, Mitri, & Henning, 2012; Reschke, 1993; Shrestha, Tannant, Proskin, & Greer, 2008; T. R. Yu & Counter, 1983). The implication is that CRF has been taken into account as an important part of Canadian mining for decades. Therefore, along with the given opportunity to the author for studying CRF properties used at a Canadian diamond mine, perhaps the completion of this research presents one more contribution to CRF development in the Canadian mining sector, particularly in diamond mines.

This research delivers unique analyses toward a particular granite CRF with the source aggregate from one diamond mine in North Canada. In addition to the expected result of qualitative property data of a particular granite cemented rockfill, some attempts aim to discover alternative effective assessments. Particularly, assessments in obtaining strain around the crack and contact interface shear behaviour of cemented rockfill can be applied not limited only to granite CRF

1.1. Research Background

The idea is simply because cemented backfill is playing an important role in underground operations, such as for support and stability. The particular role is defined by how strong the backfill itself is. The strength depends on the material type, and rock compared to other types of backfill sources already gives a distinctive opportunity to be studied. Moreover this research allows the author to study with hard rock (granite) so the result should be expected to present the data of strength property of granite CRF.

Influence of backfill properties on backfill stability is very important for the mining engineer to generate a safe effective mine design. These properties include strength parameters of backfill (Mitchell & Roettger, 1989), such as how the uniaxial compressive strength (UCS) of the backfill is related to crushing failure; tensile strength of backfill to the flexural failure occurrence; shearing resistance at the contact wall to the rotational failure of backfill. Another property is a backfill elasticity parameter, researchers carried out that backfill with higher elastic modulus is preferable (Sinclair, Shillabeer, & Herget, 1982; Y. S. Yu & Toews, 1981; Zhu, 2002). Zhu (2002) also benchmarked the study of backfill elasticity parameters concluding that the greater Poisson's ratio the greater backfill critical height. Lastly, shear parameters of backfill, internal friction angle and cohesion, are required as input into whether

analytical methods (Arioglu, 1984; Li et al., 2004; Mitchell, Olsen, & Smith, 1982) or numerical analyses (Emad, 2013; Sainsbury & Sainsbury, 2014; Tesarik, Seymour, & Jones, 2003) are used for analyzing backfill stability.

It is common sense that the addition of cement as a binder agent in backfill is aimed at obtaining a stronger outcome product. A supporting study by Zhu (2002) emphasized the superiority of rock over hydraulic or paste as a fill in terms of strength. Emad (2013) stated that CRF is basically like concrete because of its making process and components. In concrete point of view (Malešev, Radonjanin, Lukić, & Bulatović, 2014), supposed the CRF properties are also represented its rock source properties. Supporting statement which particularly from study of rockfill (Maranha, 1990) was also found. Summarizing all the supporting statements, knowing the accurate property of granite CRF with consideration of granite as a hard rock is very advantageous for backfill research development.

There is very little specific research toward the CRF of Canadian diamond mines which normally consists of cemented hard-granitic aggregate. Moreover, as a matter of fact, the author has found in many CRF analysis reviews that the CRF properties used as inputs are merely approximate numbers. The major obstacle to producing an experimental value of CRF properties is of course the aggregate size of CRF. Because in producing credible data for CRF properties, some standards regarding CRF sample size have to be satisfied, which most of the time is impractical. Therefore, it becomes a distinctive challenge and motivation to successfully produce the CRF property from real experimental works with respect to all suggested methods through laboratory testing.

1.2. Research Objective

The primary objective of this research was to produce the complete strength and elasticity properties of granite CRF. A series of laboratory tests in accordance with standard practices were conducted. In addition, this research also tried to discover alternative convenience assessments in producing qualitative property data of large-scale specimens. Thus, the involvement of an unconventional testing instrument in analyzing strain development around the crack and a practical approach in approximating shear property of CRF interface were attempted. Therefore, this study was extended and some brief research objectives were pointed out:

- Produce physical characterization of the aggregate material, which is its particle size distribution (PSD).
- Quantify the compressive and tensile strength development of the granite CRF, particularly during its critical period. In this research, the scope of the critical period is concentrated within 7 to 28 days of age of CRF.
- Complete elasticity measurements of the granite CRF. Also, discover the potency of a non-contact system for strain development around the crack measurement.
- Obtain the complete shear properties of CRF. The assessment was divided into two experimentations: shear of intact granite CRF and shear of contact interface of granite CRF to CRF. Discover the convenient flat and smooth CRF joint interface shear testing to further approximate its natural interface contact shear properties utilizing series of suggested methods.

1.3. Research Methodology

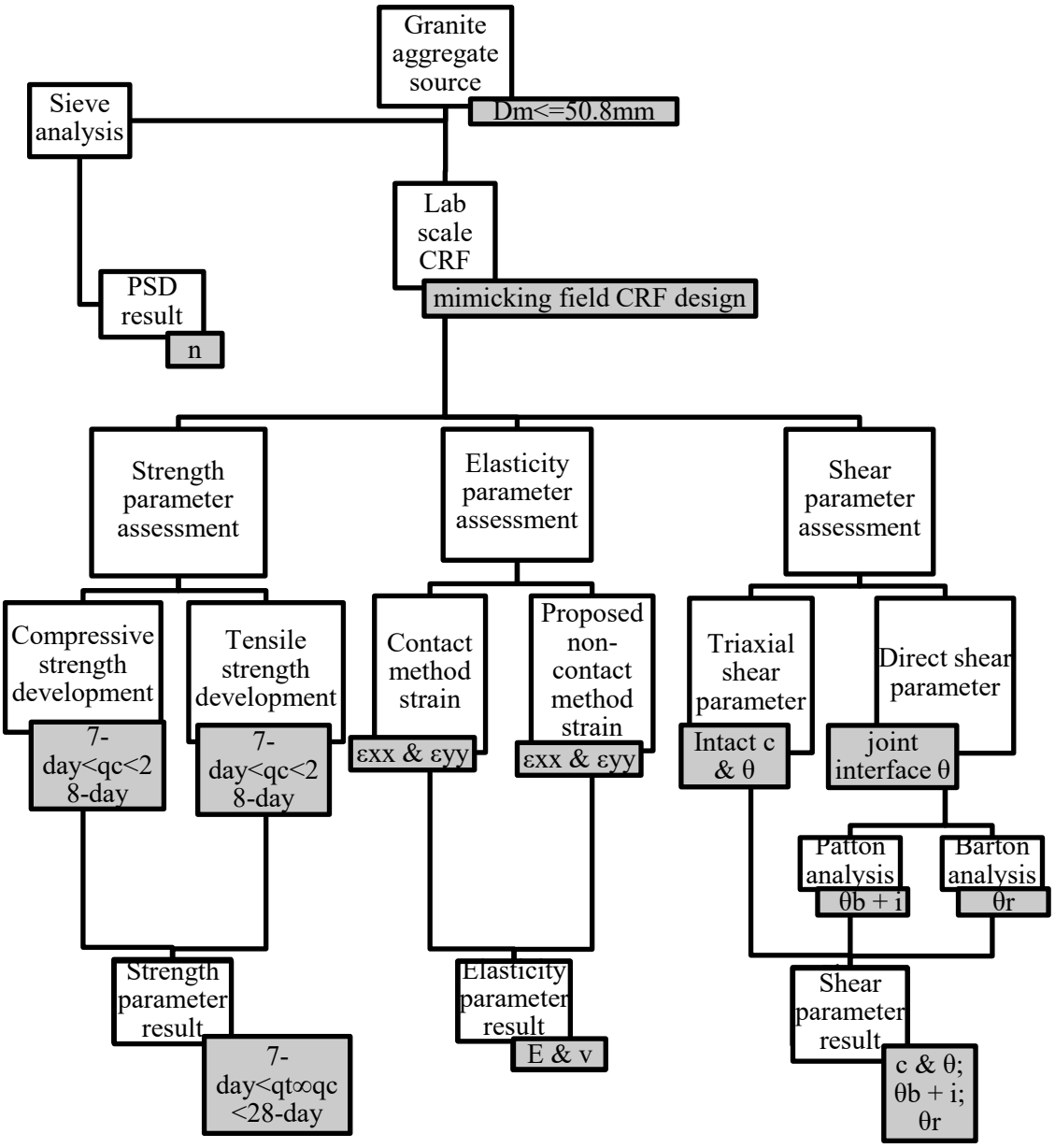

Figure 1.1. Research working flow diagram

PSD of granite aggregate was done through a sieve analysis. The result was then compared with the suggested theoretical PSD determination in cemented rockfill. In determining

optimum PSD in cemented rockfill, the only known suggested analysis (Swan, 1985) was used as a reference for comparison. This particular analysis would show the comparison of the aggregate material to the suggested one through the curve deviation.

Subsequently with the sieving analysis experiment, the specimen-making process was started. The created specimen later went for testing based on the designated strength or property assessments. The sample size was varied based on the available testing apparatus size but still met the standard sample size criteria.

The compressive and tensile strengths during the critical period when the strength of granite CRF developed were investigated. The test relied on the uniaxial compression test and tensile splitting test toward a set of samples which adequately accommodated the aggregate size. The recorded strength was divided into certain periods within 7 days of age to the maximum 28 days.

Complete elasticity properties of granite CRF were assessed by means of the elastic modulus and Poison's ratio. Large-scale CRF samples went to UCS test and the strain was recorded for further calculating the elasticity property. The strain from the unconventional method incorporating the non-contact digital image correlation (DIC) system was compared to the contact method to define its compatibility in measuring a large-scale specimen like CRF.

Shear properties of CRF to CRF interface and CRF as a mass were investigated by conducting direct shear testing on a prepared smooth contact surface between granite CRF-CRF and large-scale triaxial testing on intact granite CRF. The attempt to model shear properties of natural jointed contact surface was done by approaching and applying the known method for jointed

rock (Bandis, Lumsden, & Barton, 1981; Barton, 1973, 1976, 2013, 2016; Barton & Bandis, 1982; Barton & Choubey, 1977).

1.4. Thesis Structure

This thesis is organized into six chapters which present the work and results of each research objective within the format of a paper article. Chapter 2 focuses on the experimentation and description of the PSD of the granite aggregate and also the two different CRF mixtures that are used in this research. Chapter 3 delivers compressive and tensile strength developments of the two types of experimental granite CRFs. Chapter 4 reports the elasticity properties of the first type of granite CRF in addition to the assessment of the non-contact, digital image correlation technique for large-scale samples. Chapter 5 describes complete shear properties of contact interface and intact granite CRF. A summary of each chapter is briefly abstracted as follows.

Chapter 2: PSD of the granite aggregate that is used in the research work had been analyzed in addition to the mixing recipe of the CRF described. PSD analysis was done on the aggregate sieving result based on the suggested practice of backfill's particle distribution instead of concrete standard. There were two granite CRF mixtures used in this research which were distinguished by the proportion of water to cement and cement content in terms of weight.

Chapter 3: A study had been conducted on two different mixtures of cemented rockfill as used in the mine from where the aggregate was received from. The tests were divided based on 7, 14, 21, and 28 days of the specimen's age. The result showed the 28-day compressive (UCS) and split tensile (STS) strength differences between the two types of mixtures. Further, the

relationship between the UCS and STS of the granite CRF were formulated and presented as well.

Chapter 4: A conventional contact method using linear transducers and a non-contact method had been employed to measure axial and lateral deformations of large-scale cylindrical first type granite CRF. Results indicating similarities were discussed for further assessment of local strain development around the crack by the non-contact method.

Chapter 5: Large-scale triaxial testing had been held to accommodate the big cemented rockfill triaxial testing. Direct shear testing on a prepared flat and smooth surface had also been assessed with brief conversions and corrections to approximate the shear strength envelopes of CRF natural interface contact. The results of complete types of friction angles were basic, residual, and original, and cohesion of two types of granite CRF were presented and discussed.

Chapter 6: the overall observations, summary, and conclusions of the research as well as the future research recommendations.

References

Agricola 1494-1555, G. (1950) De re metallica / Georgius Agricola ; translated from the first Latin edition of 1556, with biographical introduction, annotations and appendices ... by Herbert Clark Hoover and Lou Henry Hoover. Edited by H. Hoover 1874-1964 and L. H. Hoover 1874-1944. New York: Dover Publications.

Amaratunga, L. M. and Yaschyshyn, D. N. (1997) 'Development of a high modulus paste fill using fine gold mill tailings', Geotechnical and Geological Engineering, 15(3), pp. 205–219. doi: 10.1007/BF00880825.

Arioglu, E. (1984) 'Design aspects of cemented aggregate fill mixes for tungsten stoping operations', Mining Science and Technology, 1(3), pp. 209–214. doi: 10.1016/S0167-9031(84)90414-6.

Bandis, S., Lumsden, A. C. and Barton, N. R. (1981) 'Experimental studies of scale effects on the shear behaviour of rock joints', in International journal of rock mechanics and mining sciences & geomechanics abstracts, pp. 1–21.

Barton, N. (1973) 'Review of a new shear-strength criterion for rock joints', Engineering Geology, 7(4), pp. 287–332. doi: 10.1016/0013-7952(73)90013-6.

Barton, N. (1976) 'Rock mechanics review. The shear strength of rock and rock joints', International Journal of Rock Mechanics Mining Science and Geomechanics Abstract, 13.

Barton, N. (2013) 'Shear strength criteria for rock, rock joints, rockfill and rock masses: Problems and some solutions', Journal of Rock Mechanics and Geotechnical Engineering. Taibah University, 5(4), pp. 249–261. doi: 10.1016/j.jrmge.2013.05.008.

Barton, N. (2016) 'Non-linear shear strength for rock, rock joints, rockfill and interfaces', Innovative Infrastructure Solutions, 1(1), p. 30. doi: 10.1007/s41062-016-0011-1.

Barton, N. and Bandis, S. (1982) 'Effects Of Block Size On The Shear Behavior Of Jointed Rock'. American Rock Mechanics Association.

Barton, N. and Choubey, V. (1977) 'The shear strength of rock joints in theory and practice', Rock Mechanics, 10(1–2), pp. 1–54. doi: 10.1007/BF01261801.

Emad, M. Z. (2013) Dynamic Performance of Cemented Rockfill under Blast-Induced Vibrations. McGill University.

Emad, M. Z., Mitri, H. S. and Henning, J. G. (2012) 'Effect of blast vibrations on the stability of cemented rockfill', International Journal of Mining, Reclamation and Environment, 26(3), pp. 233–243.

Li, L. et al. (2004) 'a 3D Analytical Solution for Evaluating Earth Pressures in Vertical Backfilled Stopes', in Proceedings of 57th Canadian Geotechnical Conference and the 5th Joint CGS–IAH Conference, pp. 24–27.

Malešev, M. et al. (2014) 'The Effect of Aggregate, Type and Quantity of Cement on Modulus of Elasticity of Lightweight Aggregate Concrete', Arabian Journal for Science and Engineering, 39(2), pp. 705–711. doi: 10.1007/s13369-013-0702-2.

Maranha, E. (ed.) (1990) Advances in Rockfill Structures. NATO ASI S. Lisbon, Portugal: Springer.

Mitchell, R. J., Olsen, R. S. and Smith, J. D. (1982) 'Model studies on cemented tailings used in mine backfill', Canadian Geotechnical Journal, 19, pp. 14–28. doi: 10.1139/t82-002.

Mitchell, R. J. and Roettger, J. J. (1989) 'Analysis and modelling of sill pillars', Innovations in mining backfill technology. Balkema, pp. 53–61.

Reschke, A. E. (1993) 'The use of cemented rockfill at Namew Lake mine, Manitoba, Canada', Minefill'93.

Sainsbury, D. and Sainsbury, B. (2014) 'Design and implementation of cemented rockfill at the Ballarat Gold Project', Mine Fill 2014 Proceeding of the 11th International Symposium on Mining with Backfill, (January 2014).

Shrestha, B. K. et al. (2008) 'Properties of cemented rockfill used in an open pit mine', in GeoEdmonton'08. Edmonton: The Canadian Geotechnical Society. Available at: http://members.cgs.ca/documents/conference2008/GEO2008/pdfs/89.pdf.

Sinclair, T. J. E., Shillabeer, J. H. and Herget, G. (1982) 'Applications of a computer model to the analysis of rock-backfill interaction in pillar recovery operations', International

Journal of Rock Mechanics and Mining Sciences & Geomechanics Abstracts, 19(4), p. 83. doi: 10.1016/0148-9062(82)90991-3.

Swan, G. (1985) 'A new approach to cemented backfill design', CIM Bulletin, 78(884), pp. 53–58.

Tesarik, D. R., Seymour, J. B. and Jones, F. M. (2003) 'Determination of in situ deformation modulus for cemented rockfill', in 10th ISRM Congress. International Society for Rock Mechanics.

Yu, T. R. and Counter, D. B. (1983) 'Backfill practice and technology at Kidd Creek Mines', CIM bulletin, 76(856), pp. 56–65.

Yu, Y. S. and Toews, N. A. (1981) Modelling of 830 Orebody of copper cliff south mine.

Zhu, Z. (2002) Analysis of Mine Backfill Behaviour and Stability. McGill.

Chapter 2: Particle Size Distribution Analysis of Granite Aggregate and the Cemented Rockfill Mix Designs Used at a Canadian Diamond Mine[1]

2.1. Introduction

The mechanical properties of backfill is known to be dependent to every mixture proportion which contained. Generally, it is obvious that any consolidated backfill has two main components: aggregate part and the binder paste part. When the aggregate and water are naturally available in the mining field, cement as a binder component other than water is still a costly material. Instead of optimizing the mixture proportion to achieve maximum strength of final product, consolidated backfill research has adopted aggregate size distribution optimization.

The aggregate within each type of cemented backfill would also be vary in terms of aggregate's particle size range. Fortunately, controlling the aggregate size variation could be undertaken together with controlled blasting activity or tailing plan and sometimes with additional backfill plan. Because this classification of cemented backfill is represented the variation of the aggregate size, an idea formulating one function to rule aggregate size distribution of the backfill was assessed (Swan, 1985).

Swan (1985) original work adopted a concrete study of the aggregate grading effects upon strength (Talbot & Richart, 1923). Talbot and Richart (1923) compared the concrete making properties of various aggregates with different amount of cement until the optimum concrete

[1] The content of this Chapter is originally appeared in the submitted papers of Chapter 3, 4, and 5. This Chapter is taken out as a thesis chapter to avoid repetition on the next following chapter.

strength in accordance with amount of cement proportionally achieved. Each grading size of aggregate formed a corresponding curvature and there was one curve which denoting the right optimal aggregate size distribution in producing highest concrete strength. Later, it was established an equation based on maximum aggregate used in form of power law function with the exponent variable as the curvature control.

The so-called Talbot curve (Talbot & Richart, 1923) was reintroduced by Swan (1985) as follow:

$$P(D) = 100\left({}^{D}/_{D_m}\right)^{n} \quad \text{.....Eq.2.1.}$$

where:

P = percentage of aggregate which passing the sieve size D by weight

Dm = the maximum aggregate size

n = an experimentally defined constant

2.2. Experimentation and Analysis

2.2.1. Particle Size Distribution Analysis

Three big batches of total approximately 6 ton granite rock aggregate 50.8 mm (2 in) and less were received from the mine as the source of material. Following the standard (ASTM C136, 2006), sampling for PSD analysis of nominal maximum size of 50.8 mm (2 in) material could be 20 kg to be assumed adequate.

In this PSD analysis experiment, a set of sieve screens utilized was built from series of 50.8 (2), 38.1(1.5), 25.4 (1), 19.05 (3/4), 12.7 (1/2), 9.525 (3/8), 4.75 [No. 4], 2 [No. 10], 0.84 [No.

20], 0.42 [No. 40], 0.25 [No. 60], 0.149 [No. 100], and 0.074 [No. 200] mm (inch) sieve openings. Considering the focus of grading to the coarse aggregate more than very fine particles, noted that the experiment did not account the grading of very fine aggregate which less than 0.074 [No. 200] mm.

Multiple sieving tests were conducted to finish 20 kg material sample due to the allowed weight limitation for once set of procedure. Figure 2.1 shows the conducted PSD test utilizing two mechanical sieve shakers. Figure 2.2 shows the recording process of the after test

Figure 2.1. Sieve shakers and the set of standard sieve frames

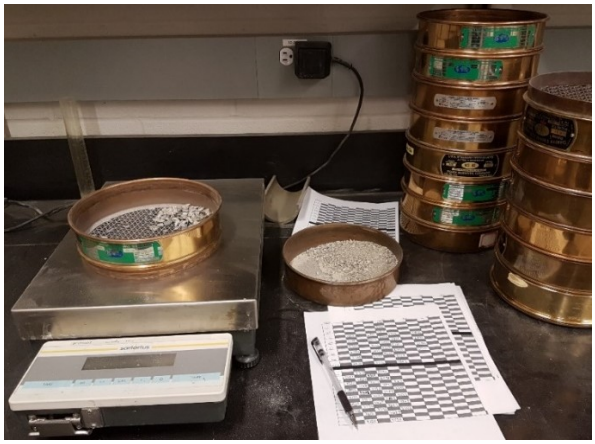

Figure 2.2. Recording process for PSD analysis

The initial PSD test result (Table 2.1) shows that the aggregate distribution is slightly rapid in transition from coarse to fine size than the optimal theory of CRF aggregates suggested by Swan (1985). Considering that the CRF particles' size of less than 10 mm is generally defined as fine aggregate, the experimental aggregate consists of 40% coarse and 60% fine aggregate by weight.

Table 2.1. Particle distribution table

Sieve Opening		**cumulative retained**	**Percent passing**
(mm)	**(in)**	**(%)**	**(%)**
50.8	2	0	100
38.1	1.5	1.88	98.12
25.4	1	13.4	86.6
19.05	0.75	21.9	78.1
12.7	0.5	34.78	65.22
9.525	0.375	44.06	55.94
4.75	0.187	57.09	42.91
2	0.079	68.05	31.95
0.84	0.033	77.03	22.97
0.42	0.017	83.91	16.09
0.25	0.01	88.63	11.37
0.149	0.006	92.29	7.71
0.074	0.003	97.29	2.71

Figure 2.3 shows the aggregate size distribution curve. The experimental granite aggregate size gradation does not follow with the one in regular concrete shown in ASTM C33M standard (ASTM C33, 2003). From the curve interpretation by using Equation 2.1, experimentally found that the suitable exponent value (n) for this granite aggregate is approximately 0.35.

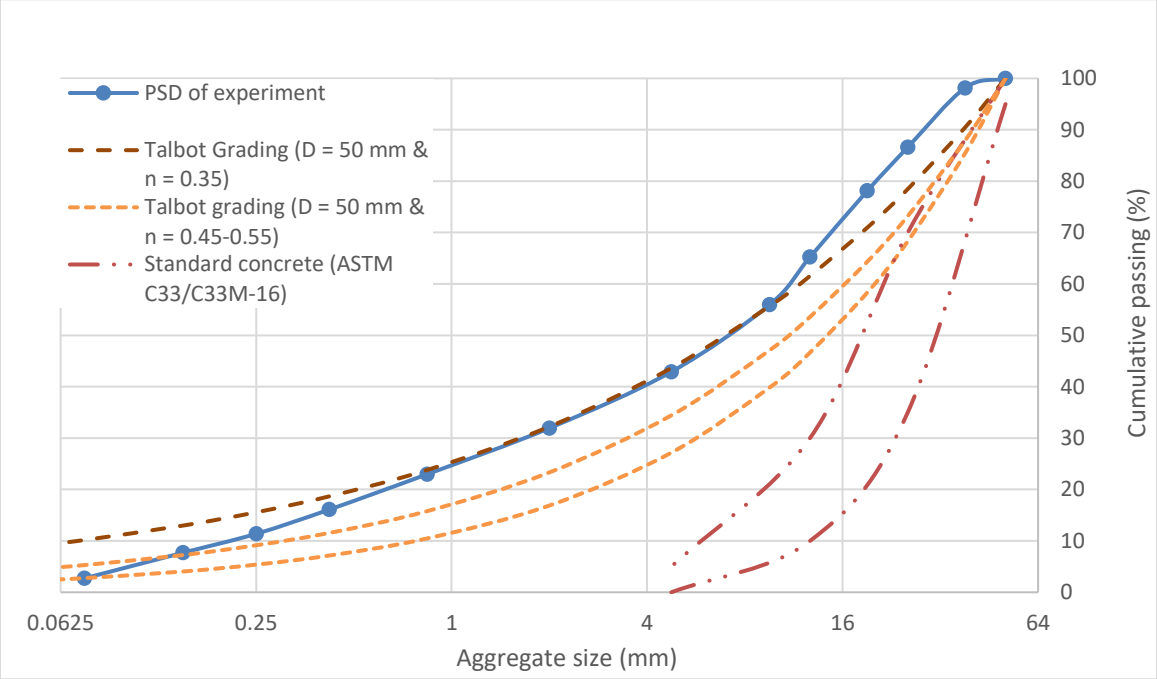

Figure 2.3. Particle size distribution of CRF aggregate

However, Swan (1985) had established an optimal n value for each type of cemented backfill. Accordingly, the optimal n for backfill was 0.5. Nevertheless, it is important to know that the rest experiment in this thesis was based on granite aggregate with n value of 0.35. The possibly greater strength and related properties of this granite CRF would be achieved if aggregate size distribution could have n value of 0.5.

2.2.2. Cemented Rockfill Mixing

Experimental specimen of this research was created in the concrete laboratory of University of Alberta. Mixture mixing utilized traditional rotary drum mechanical concrete mixers with 0.5 m^3 of maximum capacity for each. It was assumed that the laboratory specimen had an adequately same segregation level as the original field CRF.

Figure 2.4. Rotary drum concrete mixers for CRF mixing

The CRF mixture was designed based on the proportion of water to cement and cement content in terms of weight. The general-purpose Portland cement type-10 was used as the binding agent. Common practice of the admixture usage for CRF was applied so the experimental specimen generally resembled many of CRF in Canada underground mines (Sepehri, Apel, & Hall, 2017). MasterSet Delvo admixture was selected and added to the specimen mixture.

Imitating two different composition of CRF mixtures that used in the mine, the experimental specimens' mixtures are shown in Table 2.2.

Table 2.2. CRFs mix designs

Mix type	**CRF-1**	**CRF-2**
Aggregate size	< 50.8 mm	< 50.8 mm
Cement to aggregate ratio (%)	4.5	10.5
Water to cement ratio	2	1
Water to solid ratio	0.087	0.096
Admixture Delvo (L/100 kg cement)	0.475	0.675
Unit weight (kg/m3)	2358.089	2507.667
Dry-unit weight (kg/m3)	2191.442	2345.741

References

ASTM C136 (2006) ‘Standard Test Method for Sieve Analysis of Fine and Coarse Aggregates’, Annual Book of ASTM Standards, pp. 3–7. doi: 10.1520/C0136.

ASTM C33 (2003) ‘Standard Specification for Concrete Aggregates’, ASTM International, i(C), p. 11.

Sepehri, M., Apel, D. B. and Hall, R. A. (2017) ‘Prediction of mining-induced surface subsidence and ground movements at a Canadian diamond mine using an elastoplastic finite element model’, International Journal of Rock Mechanics and Mining Sciences. Elsevier Ltd, 100(October), pp. 73–82.

Swan, G. (1985) ‘A new approach to cemented backfill design’, CIM Bulletin, 78(884), pp. 53–58.

Talbot, A. N. and Richart, F. E. (1923) ‘The strength of concrete, its relation to the cement aggregates and water’. University of Illinois at Urbana Champaign.

Chapter 3: Compressive and Tensile Strengths Development Based on Early Age of Laboratory Scale Cemented Rockfill Used at a Canadian Diamond Mine[2]

3.1. Introduction

Cemented backfill is a process of returning the mining waste material with cement consolidation to the previously mined underground voids. Referring to this explanation, cemented rockfill (CRF) is a kind of a cemented backfill that incorporates waste rocks with cement as a binder. Summarized by Fall et al. (2010), cemented backfill is one of the key components of underground mining operations. It plays three important roles: it is used as a construction material, serves as a major means of ground support, and can be an effective means of mine waste disposal.

Based on the above-listed backfill roles, the utilization of cemented rockfill is economically beneficial. Yet, it has to be safe, which requires that the effective cemented rockfill composition meet the necessary strength. Therefore, unconfined compressive strength (UCS) and split tensile strength (STS) tests to judge the mechanical stabilities of CRF are of interests. First, the UCS test is relatively inexpensive and quick (Vergne, 2003). The same reason also applies to STS testing since it utilizes the same machine most of the time.

A recent study has shown the importance of the tensile strength of CRF because blast induced vibrations produce a significant tensile stress in the top most region of an exposed CRF stope

[2] The content of this Chapter has been prepared and submitted as a journal manuscript: Lingga, B. A., Apel, D. B., Sepehri, M., and Huawei, X. (2017) Compressive and Tensile Strengths Development Based on Early Age of Laboratory Scale Cemented Rockfill Used at a Canadian Diamond Mine *IJMME* (submitted)

(Emad et al., 2012). In addition, the tensile property of CRF will become a more important aspect once the mine attempting to extract the ore pillars, for example of the CRF application for underground stoping method (Figure 3.1). Therefore, a consideration of the tensile strength of CRF besides its compressive strength is also of interest.

Cemented backfill is normally designed to reach its target compressive strength after at least 28-day period (Tikou Belem, Benzaazoua, & Bussière, 2000). Based on this norm, this experiment is focused on the compressive and tensile strengths of two different CRF mixtures during that particular age period. Types of mixtures are 4.5% cement and 10.5% cement to the aggregate in terms of weight. The aggregate consists of < 50.8 mm (2 in) screened granite rocks without addition of processing tailings. Figure 3.2 shows an example of the same aggregate application in the mining field.

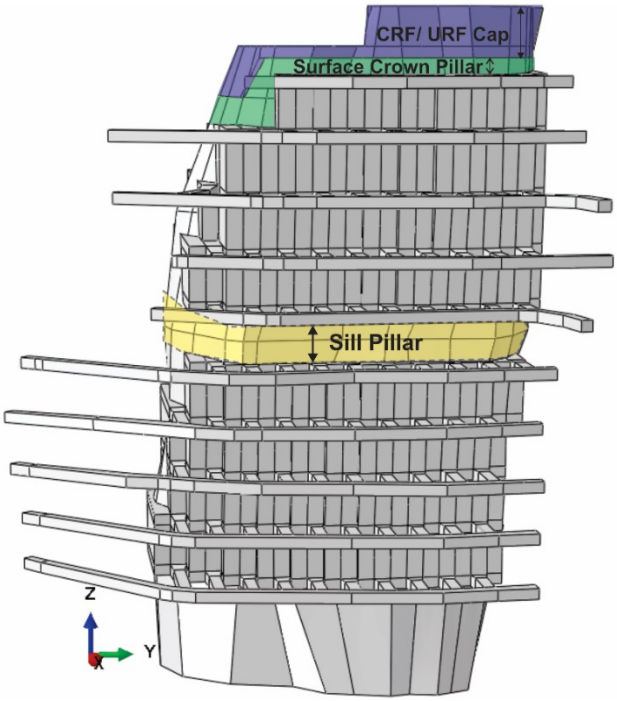

Figure 3.1. 3D geometry of stoping method with CRF after Sepehri et al. (2017)

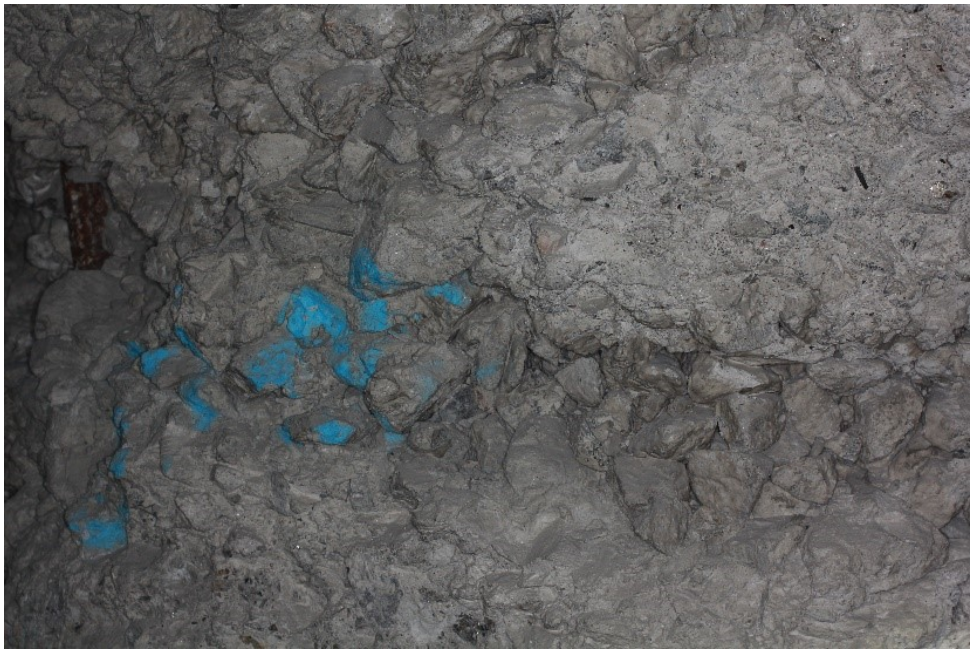

Figure 3.2. Field CRF

3.2. Material and Experimentation

Two types of specimens undergo a UCS and split tensile strength tests. The ages of specimens are divided into 7, 14, 21, and 28 days. A standard 28-day period is selected as the maximum curing age limit in this experiment. Detailed information and experimental setup are explained in the following sections.

3.2.1. Cemented Rockfill Specimen

The specimen making process followed the standard (ASTM C192/C192M, 2016). Specimens were molded within the diameter to length ratio of 152.4 x 304.8 mm (6 x 12 in) of standard cylindrical mold. The diameter accommodates three times the nominal maximum size of the coarse aggregate. After casting, all specimens were stored in a moisture room until the testing time. The humidity in the moisture room was set at 95 to 100% with 25+-2^{o} C in order to achieve the CRF's moisture content retention at approximately 8%.

3.2.2. Load Frame and Experimentation

The experiment of strength development assessment was assumed only limited between 7-28 days period. Hence, the selection of correlating formula was going to be chosen based on the observation of the experiment plot result at the first place. Therefore, all resulted strength development formulas or curvature fittings only represented development within 7-28 days. Exponential curve from age of first 24 hours until 7-day was understood but not taken in to account. The maximum period of interest, 28-day, was assumed at that point and beyond the strength of CRF is constant but the plotted curve once again did not mean to be used for extrapolation beyond 28-day.

The UCS and split tensile strength tests were performed using FORNEY FX700 compression load frame with 3.000 kN capacity. The bottom plate of the load frame is a moving part that generates force to the specimen, which is then recorded in the data logger. Each specimen confronted the axial load until reaching failure. The top loading plate was adjusted based on each kind of test. The split tensile strength test followed the standard (ASTM C496/C496M, 2011), employing 305 mm (12 in) cross-head top loading plate, in addition to a pair of thin plywood bearing strips seated between the specimen and the loading plates. The UCS test utilized the 152.4 mm (6 in) diameter unbounded caps rather than trimming the specimen's ends. This selected capping method was chosen because the frangible of CRF if it goes to the trimming table. Figure 3.3 shows the load frame and specimens of the experiment.

Figure 3.3. Load frame on UTS test setup and UCS test setup

3.3. Results and Discussions

Here is displayed first the result from all compression and split tensile tests to conveniently show the plotting data source in the following section.

Table 3.1. CRFs compressive and split tensile strengths from the experiment

		qc		qt	
	Curing Age	Samples	Mean	Samples	Mean
CRF Type	(day)	(Mpa)	(Mpa)	(Mpa)	(Mpa)
CRF-1	7	1.786	1.739	0.325	0.302
	7	1.514		0.253	
	7	1.918		0.327	
	14	2.503	2.357	0.364	0.374
	14	1.899		0.390	
	14	2.669		0.368	
	21	3.035		0.412	0.417
	21	2.655		0.389	
	21	2.845	2.845	0.450	
	28	3.451	3.351	0.408	0.410

	28	3.251		0.412	
CRF-2	7	7.069	7.294	1.240	1.305
	7	7.184		1.361	
	7	7.630		1.313	
	14	8.340	8.167	1.360	1.247
	14	7.994		1.134	
	21	7.969	8.196	1.431	1.380
	21	8.424		1.330	
	28	9.208	9.401	1.436	1.439
	28	9.594		1.443	

3.3.1. Uniaxial Compression Test Results

Figure 3.4 shows the relationship between uniaxial compressive strength, q_c, and the curing time of the backfill CRF-1 and CRF-2. Each q_c on the plot represents an average value obtained from at least two specimens. Clearly, CRF-2 has a final 28-day strength around three times of CRF-1. The strength developments of two CRF indicate a linear increment respectively. The compressive strength behaviour of this CRF-2 generally aligns with the concrete strength behaviour, which its 7-day strength is approximately 79% of the 28-day strength, while concrete is 75% of its 28-day strength. On the other hand, CRF-1's 7-day strength is only around 52% of its 28-day strength. For convenient, each sample result is available in Appendix of this Chapter.

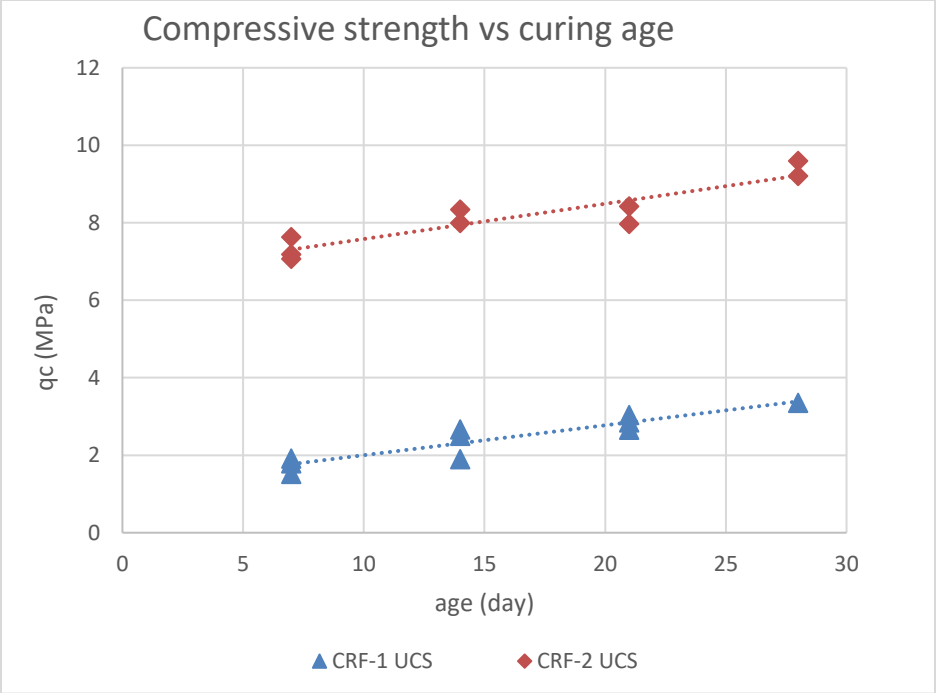

Figure 3.4. Variation in uniaxial compressive strength with curing age

A regression analysis showed that the relationship between corresponding CRF compressive strength and the curing age can be mathematically expressed as:

$q_{c1} = 0.077d + 1.229$ .....Eq.3.1.

$q_{c2} = 0.091d + 6.671$ .....Eq.3.2.

where:

q_{ci} = the CRF-i compressive strength, MPa

d = curing age, day

3.3.2. Split Tensile Test Results

The split tensile test was conducted in the same order as the UCS test. The split tensile strength and the regression plotting are shown in Figure 3.5. q_t development of CRF in this experiment

is likely linear like its compressive strength. The CRF-1's 7-day strength is approximately 73% of the 28-day strength while CRF-2's 7-day strength is around 89.5% of its 28-day strength. The comparison between the two CRFs' split tensile strength, CRF-2 has a strength approximately three times of CRF-1, similar like the compressive strength.

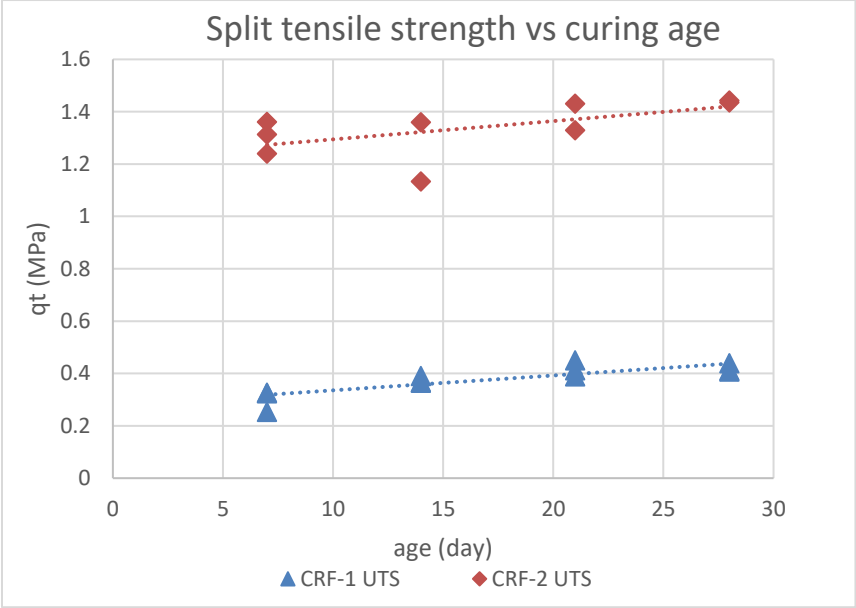

Figure 3.5. Variation in split tensile strength with curing age

For CRF's split tensile strength and the age regression, the respective mathematical model is as follows:

$q_{t1} = 0.0057d + 0.279$ .....Eq.3.3.

$q_{t2} = 0.007d + 1.225$ .....Eq.3.4.

where:

qti = the CRF-i split tensile strength, MPa

3.3.3. Compressive and Split Tensile Strength Analysis

According to the literature about CRF, it is basically similar to concrete (Emad, 2013; Tesarik et al., 2003). Therefore, a power law relationship as an analytical model for describing the tensile-compressive strength relationship of concrete supposed to be suitable for investigating the correlation (363, 2010; Oluokun, Burdette, & Deatherage, 1991). The general form of power law model can be represented as:

$q_t = K(q_c)^R$ .....Eq.3.5.

where:

R = the slope

K = values of constants at each age

Equations 3.6 and 3.7 have been derived to describe each CRF-1 and CRF-2 split tensile and compressive strength's power law best fit curve. The power law equation fitting calculations are available in Appendix of this Chapter.

$q_{t1} = 0.249(q_{c1})^{0.446}$ .....Eq.3.6.

$q_{t2} = 0.590(q_{c2})^{0.391}$ .....Eq.3.7.

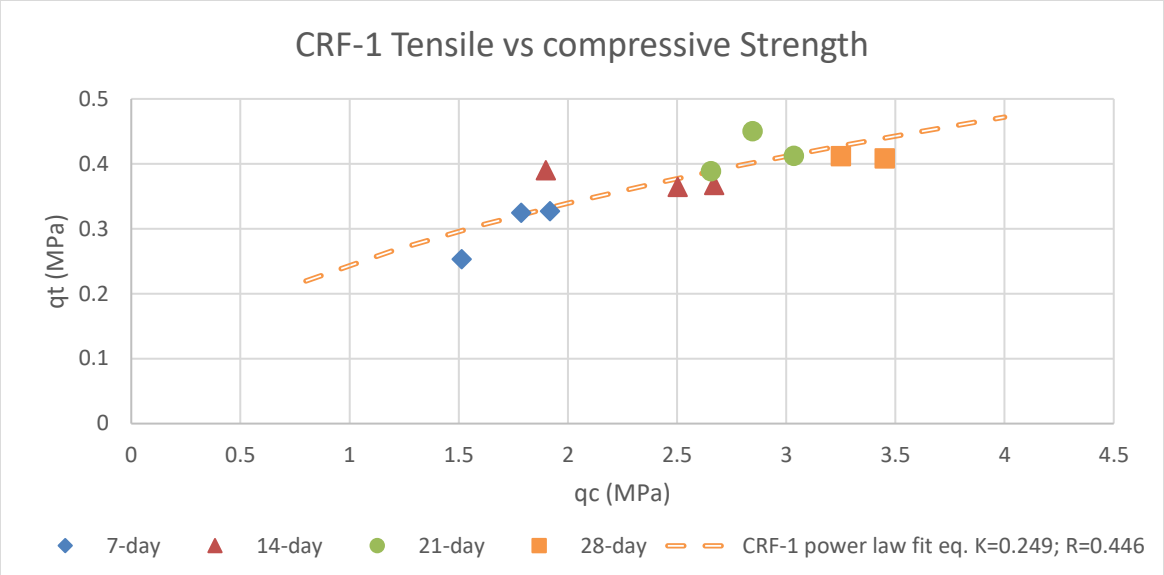

Figure 3.6. CRF-1 Split tensile to compressive strength with the projected power law best fit

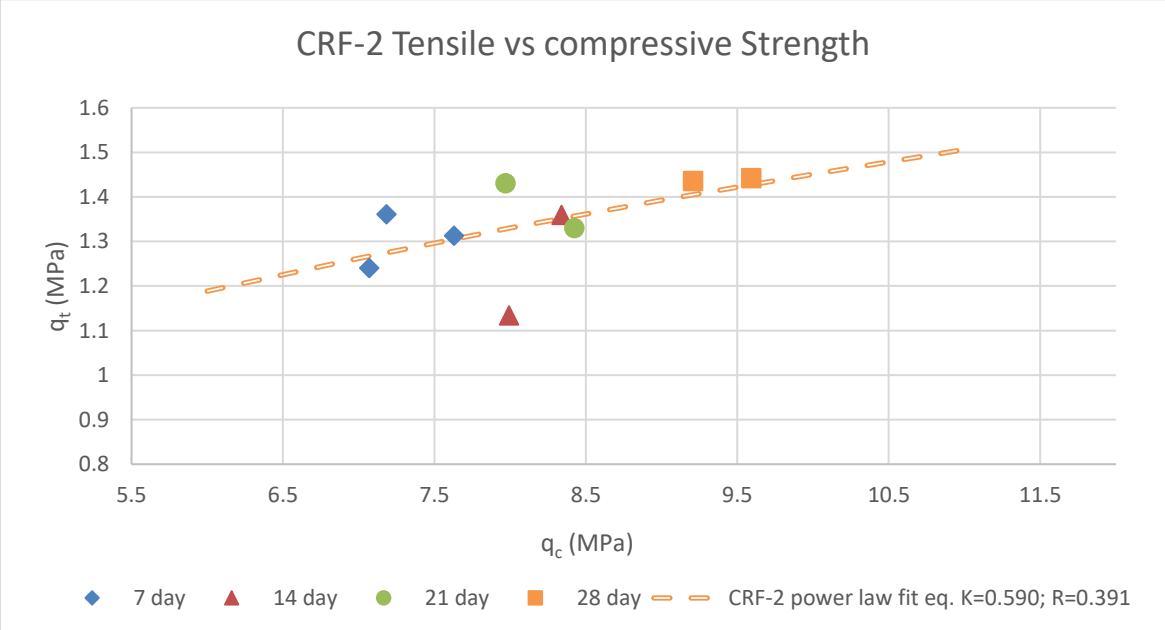

Figure 3.7. CRF-2 Split tensile to compressive strength with the projected power law best fit

The simplification of split tensile strength of CRF-1 and CRF-2 respectively are approximately ranging from 12.96 to 18.07% and 15.41 to 17.43% of the corresponding compressive strength. Table 3.2 puts out approximated values of compressive and split tensile strength developments,

ratios and comparisons based on the mathematical and analytical equations derived from the CRF experiment.

Table 3.2. Summary of CRFs compressive and split tensile strengths

age (day)	CRF-1					CRF-2				
	q_c (MPa)	$q_{c(age)}/q_{c28}$ (%)	q_t (MPa)	$q_{t(age)}/q_{t28}$ (%)	q_t/q_c (%)	q_c (MPa)	$q_{c(age)}/q_{c28}$ (%)	q_t (MPa)	$q_{t(age)}/q_{t28}$ (%)	q_t/q_c (%)
7	1.77	52.19	0.32	72.76	18.07	7.31	79.27	1.27	89.65	17.43
14	2.31	68.13	0.36	81.84	15.57	7.94	86.18	1.32	93.1	16.65
21	2.85	84.06	0.4	90.92	14.02	8.58	93.09	1.37	96.55	15.98
28	3.39	100	0.44	100	12.96	9.22	100	1.42	100	15.41

3.4. Concluding Observations

This experiment concluded that CRF-1 has 28-day compressive and split tensile strength values of about 3.39 MPa and 0.44 MPa. On the first week of age, the compressive and split tensile strengths possess, respectively, 52.19% and 72.76% of its 28-day strength with the strengths gain of 0.077 MPa and 0.0057 MPa on each day.

CRF-2 has 28-day compressive and split tensile strength values of around 9.22 MPa and 1.42 MPa. The first week of age strengths, respectively, are 79.27% and 89.65% of its 28-day strength with the compressive and split tensile strengths gain of 0.091 MPa and 0.007 MPa every day.

During 7 to 28 days, CRF-1 strength is 1/3 of CRF-2 strength, which applies to both compressive and split tensile. The split tensile strength of CRF-1 and CRF-2, respectively, are approximately ranging from 12.96 to 18.07% and 15.41 to 17.43% of the corresponding compressive strength.

The strength property is highly dependent on the testing method that is used. This experiment relied the tensile strength value based on STS test and the compressive strength value with UCS test of 2:1 diameter to length ratio cylindrical sample. Further adjustment for flexural and compressive in situ should be considered as needed.

References

363, A. C. I. C. (2010) 363R-10 Report on High-Strength Concrete. American Concrete Institute.

ASTM C192/C192M (2016) 'Standard Practice for Making and Curing Concrete Test Specimens in the Laboratory', ASTM International, pp. 1–8.

ASTM C496/C496M (2011) 'ASTM C496 Standard Test Method for Splitting Tensile Strength of Cylindrical Concrete Specimens', ASTM International, p. 5. doi: 10.1520/C0496.

Belem, T., Benzaazoua, M. and Bussière, B. (2000) 'Mechanical behaviour of cemented paste backfill', in Proc. of 53rd Canadian Geotechnical Conference, Montreal. Montreal, pp. 373–380.

Emad, M. Z. (2013) Dynamic Performance of Cemented Rockfill under Blast-Induced Vibrations. McGill University.

Emad, M. Z., Mitri, H. S. and Henning, J. G. (2012) 'Effect of blast vibrations on the stability of cemented rockfill', International Journal of Mining, Reclamation and Environment, 26(3), pp. 233–243.

Fall, M. et al. (2010) 'A contribution to understanding the effects of curing temperature on the mechanical properties of mine cemented tailings backfill', Engineering Geology. Elsevier B.V., 114(3–4), pp. 397–413. Available at: http://dx.doi.org/10.1016/j.enggeo.2010.05.016.

Oluokun, F. A., Burdette, E. G. and Deatherage, J. H. (1991) 'Splitting Tensile Strength and Compressive Strength Relationships at Early Ages', ACI Materials Journal, 88(2), pp. 115–121. Available at: http://www.concrete.org/Publications/ACIMaterialsJournal/ACIJournalSearch.aspx?m=details&ID=1859.

Sepehri, M., Apel, D. B. and Hall, R. A. (2017) 'Prediction of mining-induced surface subsidence and ground movements at a Canadian diamond mine using an elastoplastic finite element model', International Journal of Rock Mechanics and Mining Sciences. Elsevier Ltd, 100(October), pp. 73–82.

Tesarik, D. R., Seymour, J. B. and Jones, F. M. (2003) ‘Determination of in situ deformation modulus for cemented rockfill’, in 10th ISRM Congress. International Society for Rock Mechanics.

Vergne, J. (2003) Rules of thumb for the hard rock mining industry. 3rd edn, Hard rock miner’s handbook. 3rd edn. Edited by S. L. Andersen. Stantec Consulting.

Chapter 4: Assessment of Digital Image Correlation Method in Determining Elastic Properties of Large Scale Cemented Rockfill Samples[3]

4.1. Introduction

In order to produce meaningful results during the unconfined compressive strength (UCS) testing of the CRF material the prepared samples have to be large enough to maintain high ratio between the diameter of the sample and the aggregate size (ASTM C192/C192M, 2016). However, measuring the sample deformations using the traditional strain monitoring techniques such as the LVDTs is usually challenging due to the size restrictions of the most monitoring equipment. It is also not recommended to place strain gages on the surface of a CRF sample to measure its overall deformations. As such measurements would give erroneous results that highly depend on the placement of the strain gauges due to the CRF material's composition consisting of a stiff aggregate material and a soft binding agent.

The strain measurement methods that use strain gages or LVDTs are also restricted due to internal limitations and external factors, such as gage's length limitation or compressometer-extensometer's limited ring size and temperature. In addition, mounting misalignment is another cause of frequent errors during the deformation measurements. The recent sustainable and flexible measuring device working based on a digital image correlation (DIC), a non-contact technique for strain measurements is utilized together with the former contact method.

[3] The content of this Chapter has been prepared and submitted as a journal manuscript: Lingga, B. A., Apel, D. B., Sepehri, M., and Pu, Y. (2017) Assessment of Digital Image Correlation Method in Determining Elastic Properties of Large Scale Cemented Rockfill Samples *IJMST* (submitted)

In this study, the DIC system from Correlated Solutions' instruments (Correlated Solutions, 2017) has been utilized.

DIC generates the displacement data by comparing the difference in the position of a point of interest based on two different images taken from the same position in a global coordinate system. Summarized by Chu et al. (1985), the displacement function and finite strain equations in digital-correlation work after object projection onto a plane using a linear Taylor's expansion:

$$\varepsilon_{xx} \cong \frac{\partial u}{\partial x} + \frac{1}{2}\left[\left(\frac{\partial u^2}{\partial x}\right) + \left(\frac{\partial v^2}{\partial x}\right)\right] \quad \text{.....Eq.4.1.}$$

$$\varepsilon_{yy} \cong \frac{\partial v}{\partial y} + \frac{1}{2}\left[\left(\frac{\partial u}{\partial y}\right)^2 + \left(\frac{\partial v^2}{\partial y}\right)^2\right] \quad \text{.....Eq.4.2.}$$

where:

ε_{xx} = strain on x direction

ε_{yy} = strain on y direction

u, v = components of an arbitrary point displacement in the x and y direction respectively

Since the object essentially needed to be projected onto a plane, the DIC method was then mainly focused on how to obtain the true coordinate of any kind of object surface by using optical instrument. In the early 1990s (Helm, Sutton, & McNeill, 1996; Luo, Chao, Sutton, & Peters, 1993), DIC concepts finally advanced into stereovision systems that enabled obtaining the true three-dimensional (3D) position of each point on a non-planar object. 3D-DIC designates two or more pinhole cameras to collect and then compare object region images from two or more viewpoints.

For in-plane surface deformations, 3D-DIC is able to extract each component accurately, despite undergoing rigid body translation and rotation (Sutton, Yan, Tiwari, Schreier, & Orteu, 2008). This final experiment conducted by Sutton et al. proved that one set of a stereovision system, which consisted of two standard lenses interpreting matching strains (slope of linear best fit of ε_{yy} is -1.31 x 10^{-6}/mm out of plane translation) on the out of plane translation of planar object without any load application or deformation.

In 3D-DIC, monitoring is not limited to tests on only flat surface but it has been used when testing cylindrical specimens. These tests were described by several researchers who were able to obtain good results (Lu, Vendroux, & Knauss, 1997; Peters III, Sutton, Ranson, Poplin, & Walker, 1989; SANTOS, PITANGUEIRA, RIBEIRO, & CARRASCO, 2016). However, it is still difficult to find literature on testing large CRF specimens with investigations of crack development by the 3D-DIC.

In this chapter, conventional fixed mounted LVDTs and string potentiometers are reported the elasticity property assessment of CRF, in addition to utilization of 3D-DIC method during CRF specimens testing for possibility of local strain and crack development investigations.

4.2. Materials and Experimental Setup

The UCS test was conducted for six CRF specimens of 4.5% cement content and 304.8 mm (12 in) in diameter. During the test, the deformations were recorded by DIC system using VID-3D software (Correlated Solutions, 2010). In addition, two fix-mounted LVDTs, three string potentiometers were recording the lateral and vertical deformations. Detailed information and experimental setup are explained in the sections below.

4.2.1. Cemented Rockfill Specimen

The specimens were molded with the diameter to length ratio of 309.8 mm to 609.6 mm. The diameter accommodates more than three times the nominal maximum size of the coarse aggregate, which is 50.8 mm (2 in). The molds in this experiment were made from Sonotube. Each CRF mixture was vibrated using the vibrating rod – this was done every one third of height of the mold during the pouring process. Prior to testing, specimens were cured indoors for 28 days. This time was selected so that the backfill could reach its targeted compressive strength values (Tikou Belem et al., 2000).

The specimens were finished by capping the top and bottom surfaces, and spray painting the white and black speckles onto the samples surface. The capping process utilized high-strength gypsum paste that follows standard (ASTM C617/C617M − 12, 2012) to ensure the uniform load distribution applied on the specimen. While the black-white speckles are used by the DIC cameras to track the deformation of multiple points painted onto the specimen surface. Figure 4.1 and 4.5 respectively shows the ready sample and the selected points of interest on the tested specimen.

Figure 4.1. 12 x 24 in ready for testing specimen

4.2.2. Experimental Setup

4.2.2.1.Load Frame and Contact Method Setup

The UCS tests were performed under constant displacement control using MTS loading frame with the 6,230 kN capacity. Each specimen was loaded using the axial load till reaching failure. The initial load was applied first on each sample for seating the specimen on the loading plates.

Two LVDTs were each placed at diametrically opposite points about mid-height of the specimen. These two LVDTs recorded the lateral deformation to the data logger; this data was then converted to be the lateral strains. Similar LVDT setup was used to measure the vertical deformations. The axial strain was calculated from the average of three string potentiometers attached from the bottom to the top cap of the MTS frame. Figure 4.2 shows the setup of this contact method; unfortunately, the third string potentiometer could not be shown as it was placed behind the sample.

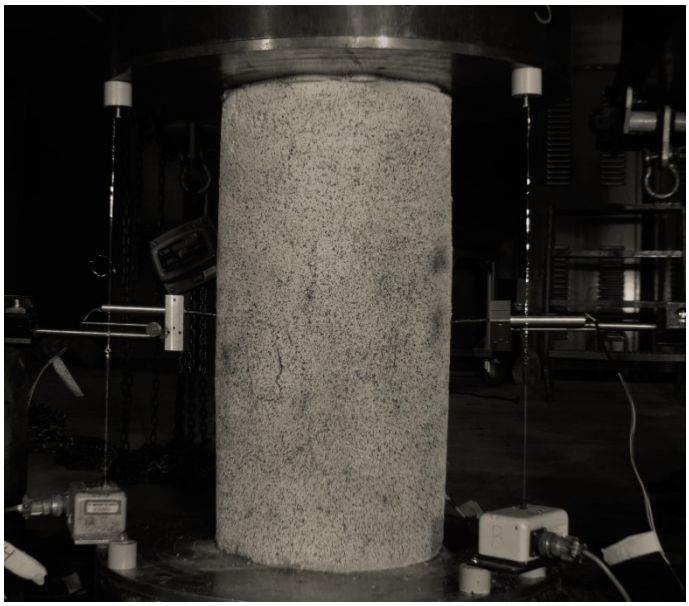

Figure 4.2. Setup of LVDTs and string potentiometers

4.2.2.2.3D-DIC Setup

As illustrated in Figure 4.4, two cameras (one stereovision system) were set up in front of the specimen, covering approximately half of the cylinder surface. Incorporating Fujinon 1:1.4/12.5 mm lenses and Point Grey cameras generated a resolution of 2,448 x 2,048 pixels. Adequate illumination by indoor lamps and two additional task lamps was used to depict each distinctive image. Each of the images was captured with the rate of one image every two seconds. The cameras were calibrated before the tests using a calibrating board with 12 x 9 grid on 25 mm spacing (Figure 4.3).

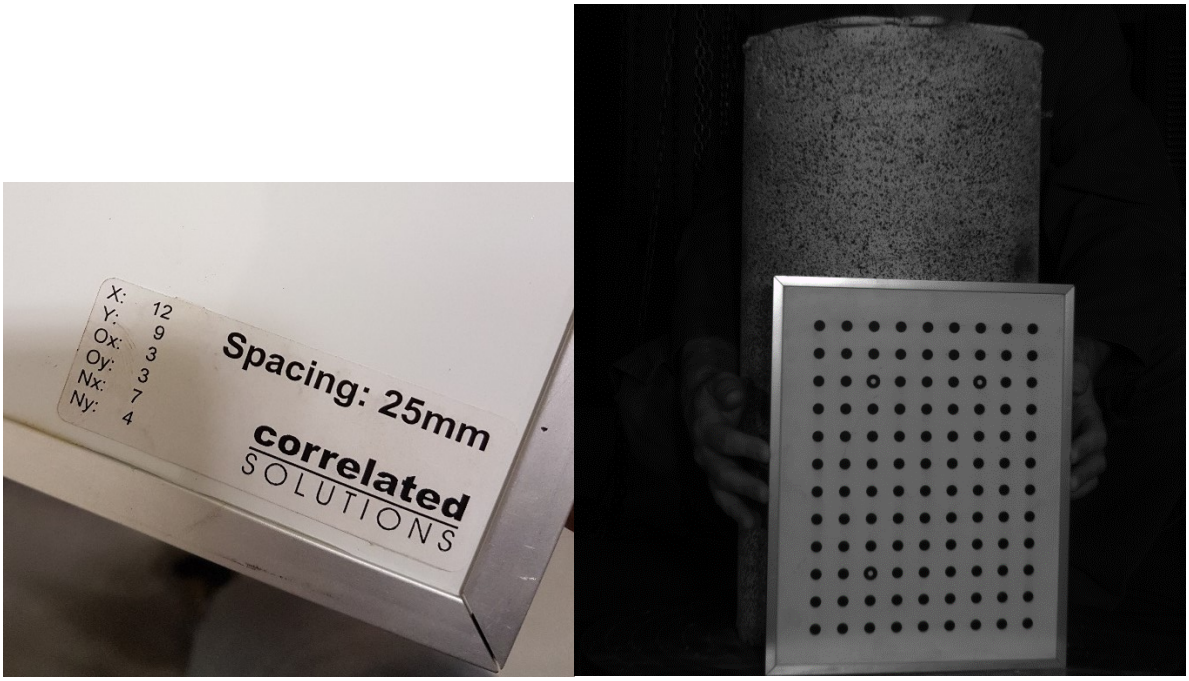

Figure 4.3. Calibrating board and calibration process

The image correlation process was run using the VIC-3D 2009 software. The procedure started with first creating an area of interest (AOI) that covered the specimen surface in the reference image and placing the start point around the bottom (fixed part) of the specimen as the AOI. During the second step, the subset and step size were defined. The suggested subset size of 21

was used to give an optimal match confidence of 0.01 pixel, while a ‘step size’ of five was chosen with the consideration of processing time. The third step consisted of running the correlation.

The original correlation outcome was then converted into cylindrical interpretation by applying cylindrical transformation option in VIC-3D software. Next, the rigid body motion was removed – this feature was also provided by the software. Afterwards, the strain can be properly computed to represent both axial strain and lateral strain. Five consecutive points along the perimeter in line with the LVDT height became the points of interest and produced the average axial and lateral strain to be analyzed for this experiment (see Figure 4.5).

Figure 4.4a. Placement of 3D-DIC instruments, specimen, and load frame

Figure 4.4b. Detailed setup of 3D-DIC instruments, camera, and lens

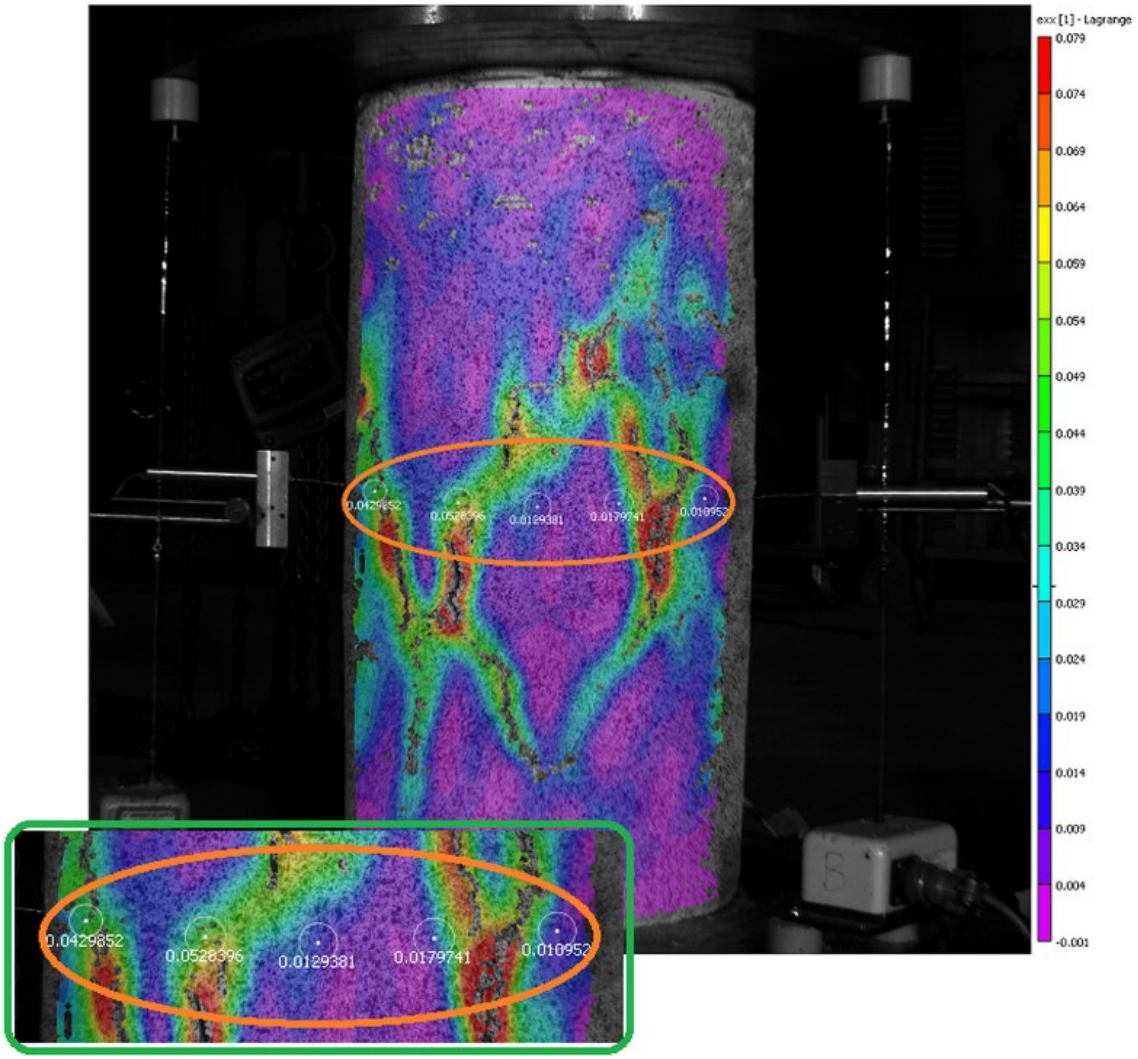

Figure 4.5. Five discs point of interest along the perimeter line of the specimen's mid-height, p1-p5 (left to right). ε_{xx} contour from one of the deformed 1st specimen (CRF-1a) after failure

4.2.3. Modulus of Elasticity and Poisson's Ratio Calculations

Theoretically, modulus of elasticity is calculated based on tangent modulus. Accordingly, strain component is calculated around the fixed 50% of the maximum strength, as it normally used in rock testing. Based on standard (ASTM D7012-14, 2014). This is simply the slope of stress-axial strain.

$$E_t = \Delta\sigma_{50} \,/\, \Delta\varepsilon_{yy_{50}} \quad \text{.....Eq.4.3.}$$

where:

E_t = tangent modulus of elasticity, MPa

$\Delta\sigma_{50}$ = stress difference corresponding at fixed percentages around 50% of UCS, MPa

$\Delta\ \varepsilon_{yy50}$ = axial strain difference corresponding at fixed percentages around 50% of UCS

Following the same standard, Poisson's ratio is theoretically calculated by dividing the slope of the stress-axial strain to the slope of stress-lateral strain.

$$v = -\Delta\varepsilon_{xx_{50}} / \Delta\varepsilon_{yy_{50}} \quad \text{.....Eq.4.4.}$$

where:

v = Poisson's ratio

$\Delta\ \varepsilon_{xx50}$ = lateral strain difference corresponding at fixed percentages around 50% of UCS

$\Delta\ \varepsilon_{yy50}$ = strain difference corresponding at fixed percentages around 50% of UCS

In this study, the magnitudes of Poisson's ratio and elastic modulus slopes are generated using linear best-fitting line method from 35-65% of the UCS.

4.3. Results and Discussion

4.3.1. Typical Stress-Strain Relationship of the Experimental Results

The following two figures (Figure 4.6 and 4.7) represent the typical stress-strain transcription of this experiment. Even though both figures were produced by the experimental specimen in Figure 4.5 (CRF-1a), all the experimental specimens indicated a similarity. Each disc point of interest of 3D-DIC method was initially lying in the same order with the contact method then gradually departing to a particular extent.

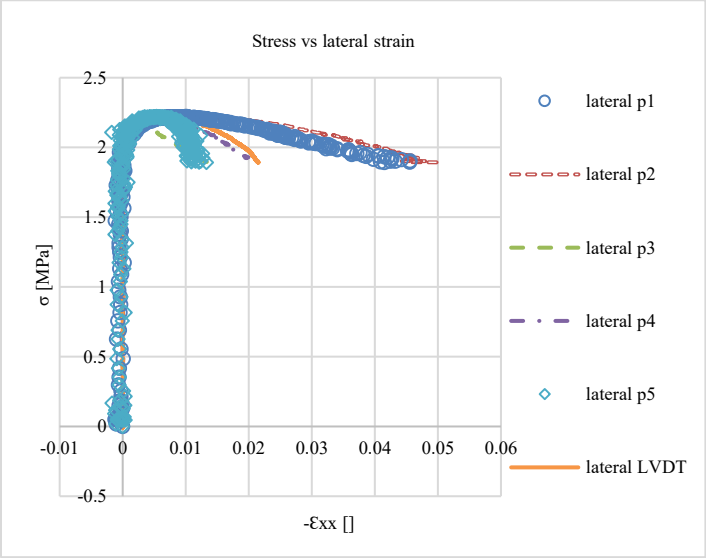

Figure 4.6. Stress-lateral strain CRF-1a

Figure 4.6 shows stress-lateral strains measured by the LVDT and the 3D-DIC monitor that followed strains at the selected 5 points of interest in the mid-section of the sample. Each of the recorded 3D-DIC's stress-lateral strain curve reasonably follows the curve recorded by the LVDT. Only p1 and p2 recoded stress-strain curves that diverged far from the LVDT recorded trend. The divergence was caused by the fractures adjacent to those two points of interests that were developing during the test (see Figure 4.5).

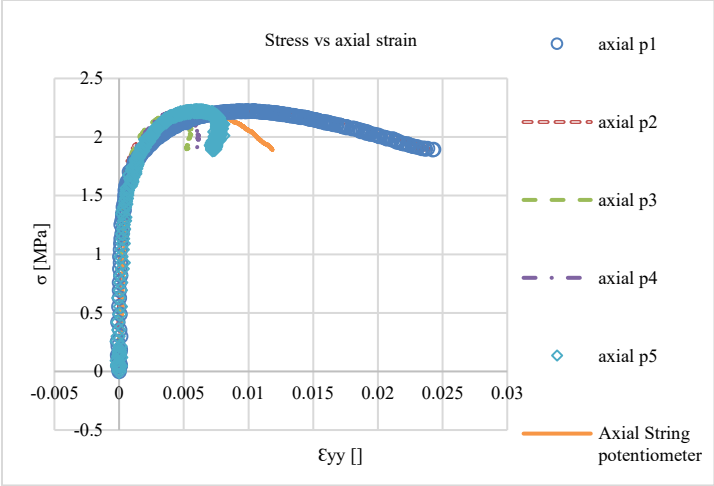

Figure 4.7. Stress-axial strain CRF-1a

Figure 4.7 shows an axial stress-strain relationship graph during the test. The axial stress-strain curves recorded by both methods also show a very good agreement between the two measurement methods. Furthermore, 3D-DIC shows a consistency of its p1 and p2 that diverged far from string potentiometer strain, similar to the lateral strain comparison case.

As illustrated in both Figure 4.6 and 4.7, strains from all points of interests ”generally” show a consistency with and conformity to the contact method. Some ”visible” deviations become greater after passing the peak strength, this is understandable because of the heterogeneity of the concrete system. Asserting that the microcracking at the aggregate-paste interface does exist (Meyers, 1969), it initiates random propagation of paste cracks along the load application during the test. At the end of the test, each part of the specimen’s surface actually ends at different strain value.

Figure 4.8 and 4.9 summarizes the other stress-strain transcriptions from rest of tested samples. As previously explained from Figure 4.6 and 4.7, some far-off deviation curves between 3D-DIC and contact method are resulted because of the heterogeneity of CRF system and this

emphasized the advantage of non-contact system for measuring the local strain around the developing crack.

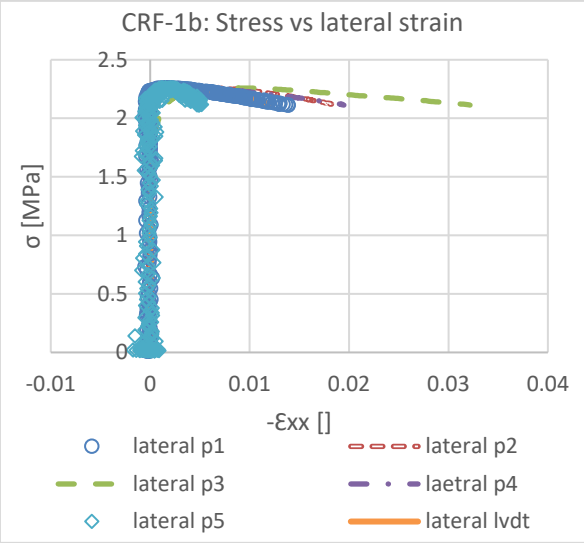

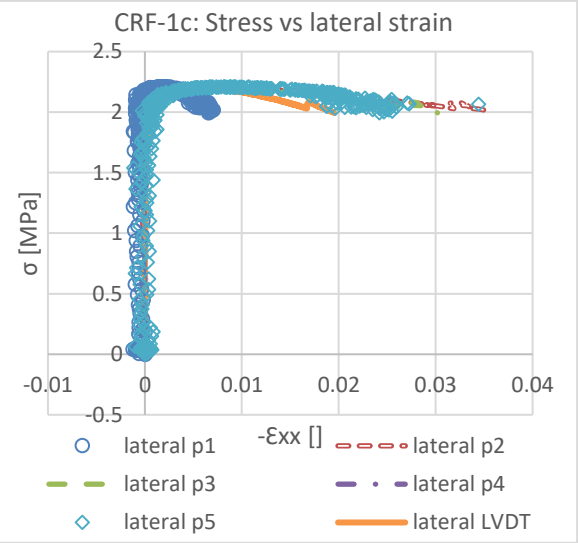

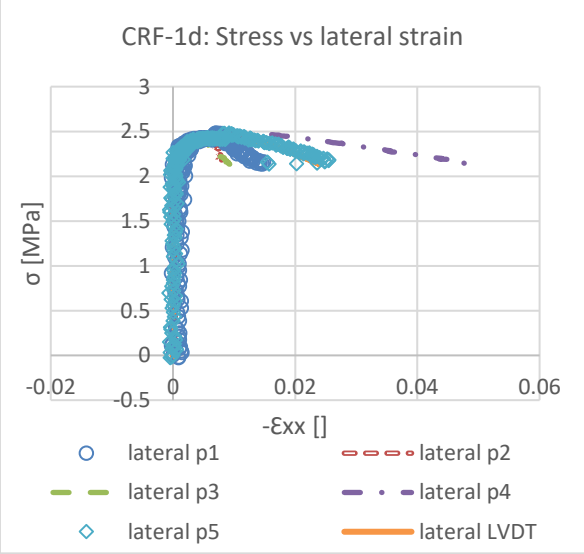

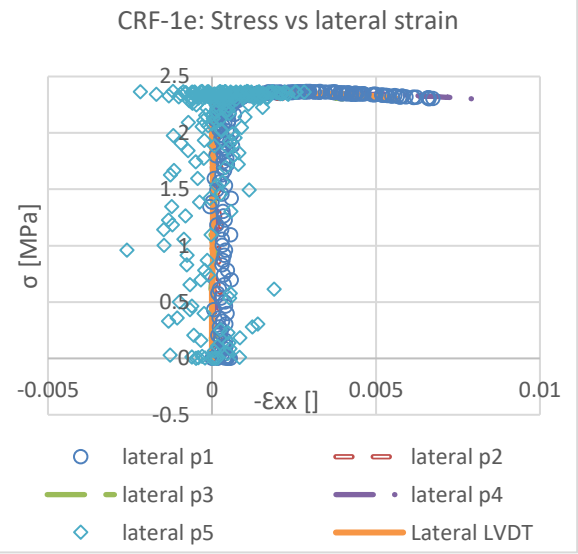

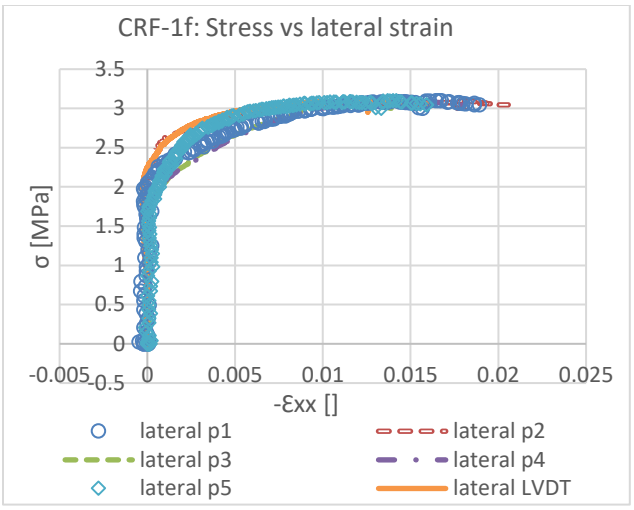

Figure 4.8. Stress-lateral strain CRF (1b-1f)

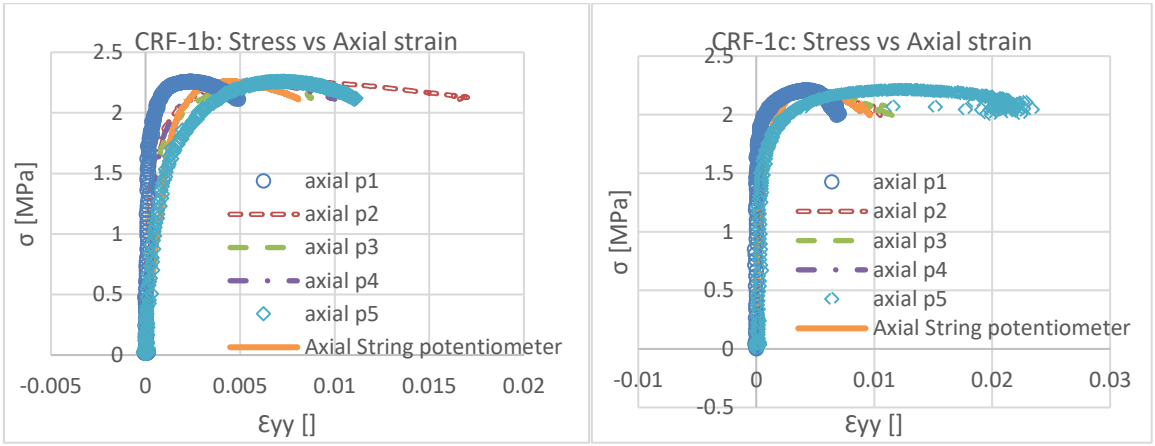

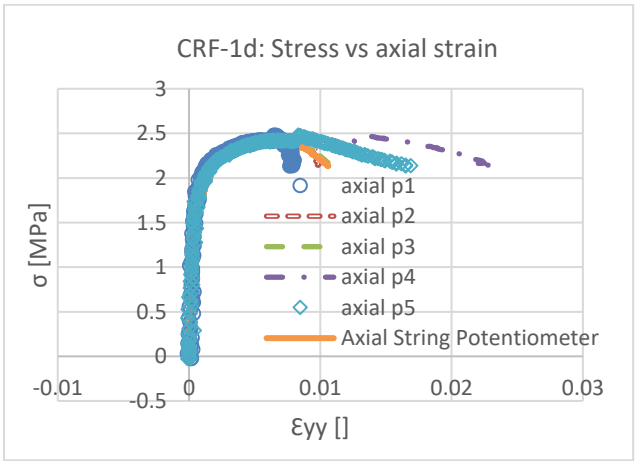

Figure 4.9. Stress-axial strain CRF (1b-1d)

4.3.2. Analysis of Strain Correspondence Between Contact and DIC Methods

The analysis shown in Figure 4.10 was derived from the same specimen as shown in Figure 4.5, CRF-1a, in which the 3D-DIC Ɛyy and string potentiometer Ɛyy respectively are the Y and X axis. The axial strain correspondence between 3D-DIC and string potentiometer is represented in terms of the slope magnitude of a linear fit-line from average five discs point of interest 3D-DIC Ɛyy to string potentiometer Ɛyy, taken along the real-time test while each scatter path is solely a Ɛyy matching plotting between one disc point of interest 3D-DIC and contact method. The plot is recorded until the specimen reaches the UCS. CRF-1a concludes that 3D-DIC axial strain is 6.04% higher than axial strain from string potentiometer in general.

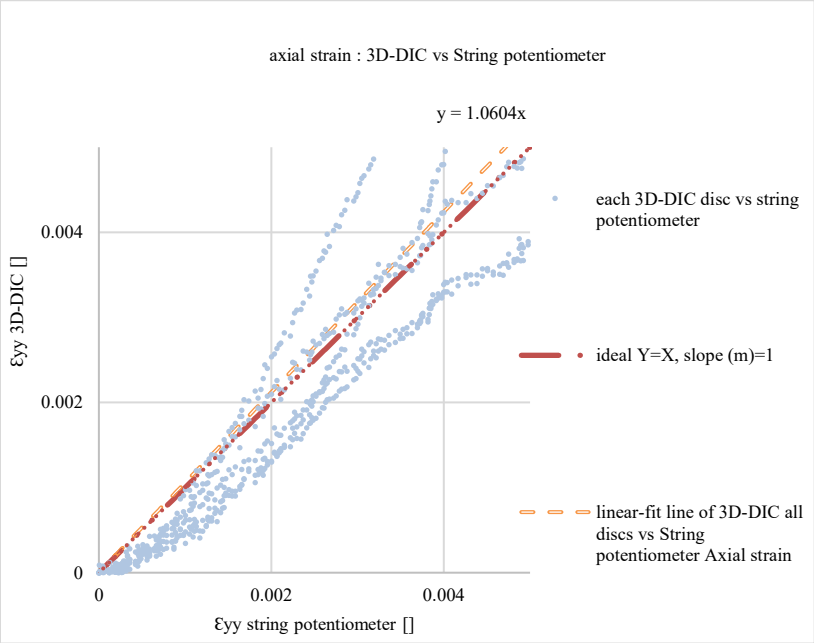

Figure 4.10. Axial strain ratio 3D-DIC to string potentiometer, CRF-1a

Applying this matching analysis to the rest of sample testing result, the summary of experimental specimens' result between the two methods for lateral and axial strain respectively are given in Figure 4.11 and 4.12. Detailed graph of the rest of samples is available

in Appendix of this Chapter. The mean differences of 5.1% and 14.5% were found for lateral and axial strain respectively (see Table 4.1).

Table 4.1. Mean difference of strain between contact and non-contact methods

CRF 4.5%	**Linear-fit ratio between 3D-DIC and Contact method**	
specimen#	**lateral strain ratio (gradient)**	**axial strain ratio (gradient)**
CRF-1a	0.925	1.0604
CRF-1b	1.273	1.1827
CRF-1c	0.852	1.1163
CRF-1d	0.826	1.219
CRF-1e	1.083	
CRF-1f	1.349	
mean	1.05132	1.1446

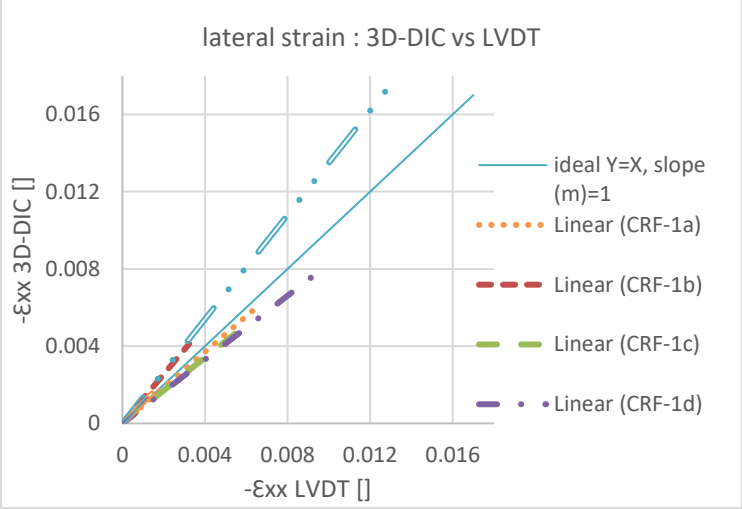

Figure 4.11. Lateral strain ratio 3D-DIC to LVDT

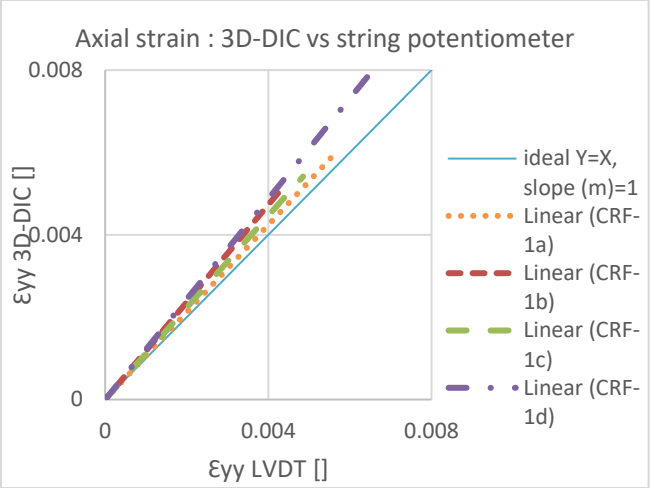

Figure 4.12. Axial strain ratio 3D-DIC to string potentiometer

These two figures also show the range of strain until failure at UCS (i.e., the length of axes) for this particularly large 4.5% CRF. The lateral strain and axial strain at failure are approximately 0.01 and 0.006. Back calculating these values to the specimen dimension (diameter and length), then to the mean value of strain ratio difference from both measurement methods (Table 4.1), will approximate the maximum (at UCS) difference of 3D-DIC to conventional method in magnitude of µm. Therefore, the maximum difference between both methods for large-scale CRF specimen in this experiment is 156 µm for the lateral and 529 µm for the axial.

4.3.3. Strain Measurement Finding of Non-Planar Out of Plane Deformation from 3D-DIC

During the analysis of strain using non-contact method, there is an indication of the scattered or distorted behavior of out of plane strain reading is happening along particular $0<|\varepsilon|<0.0005$ (see Figure 4.13) and then after the scatter path starts merging. This ε of 0.0005 may be the minimum strain accuracy for out of plane deformation reading of a non-planar object. Comparing with Sutton et al. (2008) who was previously mentioned (Section 4.1,

Introduction), his experiment resulted a detection of strain of 0.00000134/mm out of plane translation but without real deformation (only a magnification effect from moving the object toward the two cameras) of a 'planar object'.

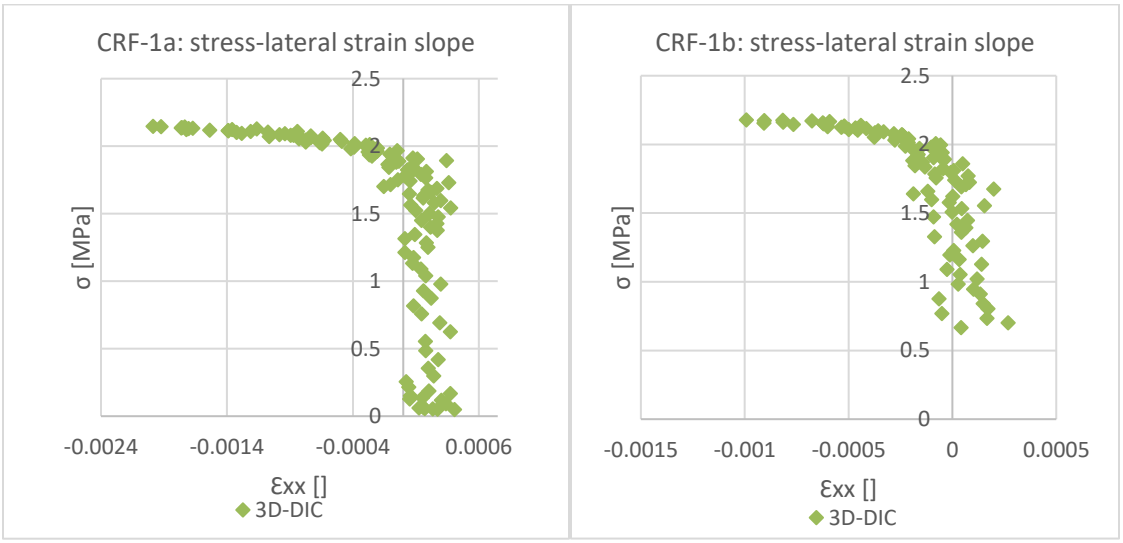

(a) (b)

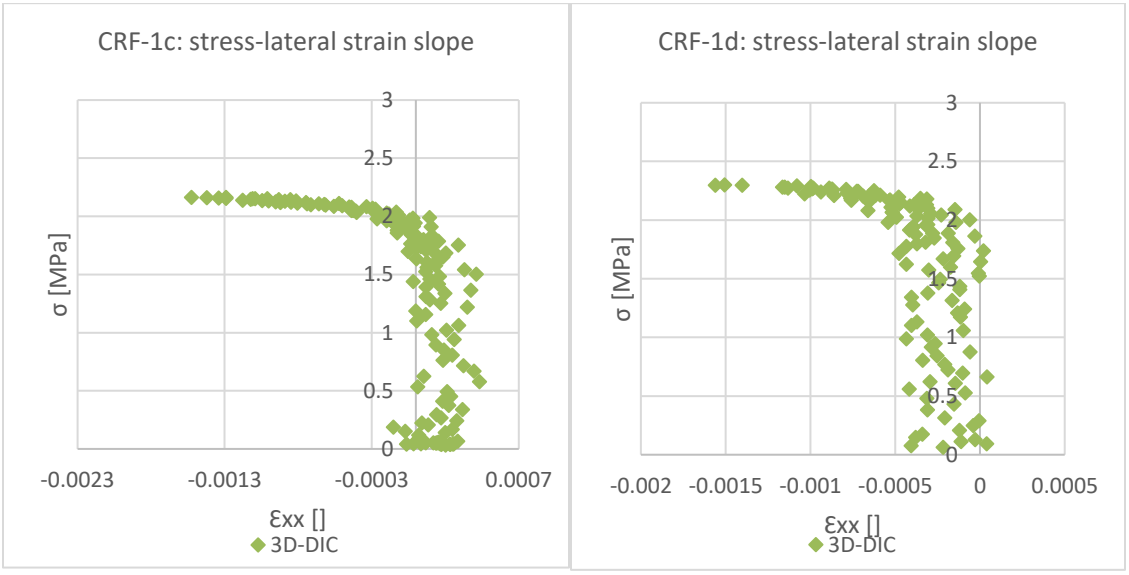

(c) (d)

Figure 4.13. Extended linear line best-fit, stress-lateral strain slope matching

4.3.4. Modulus of Elasticity and Poisson's Ratio Analyses

As mentioned in the Section 4.2.3, E and *v* are determined by the linear best-fitting technique toward the contact method strain measurement. The next set of figures show the interpretation of E from four CRF specimens (1a-1d). On Figure 4.14, E value is denoted by the gradient of the trend line equation and used as the numerator for later *v* calculation. Figure 4.15 denotes the gradient of trend line equation as later used as the denominator for *v* calculation.

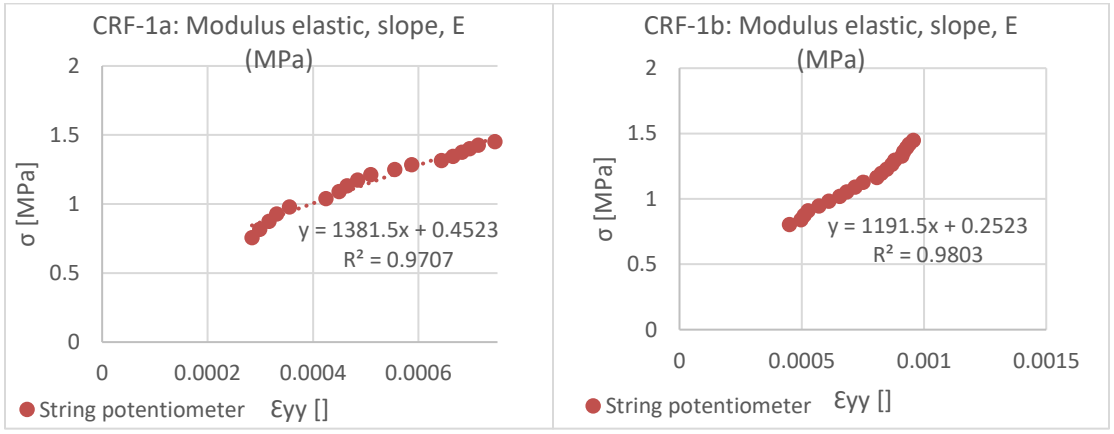

(a) (b)

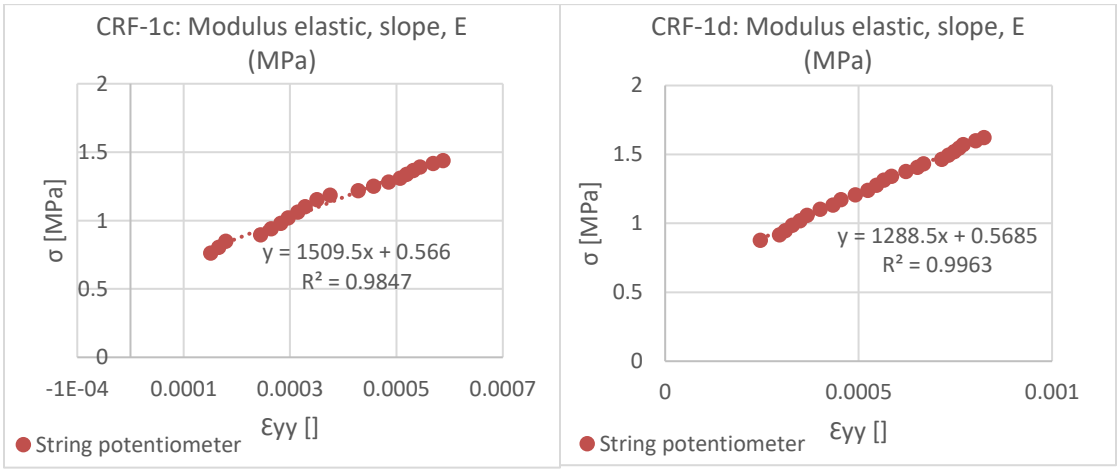

(c) (d)

Figure 4.14. Linear line best-fit, elastic modulus determination

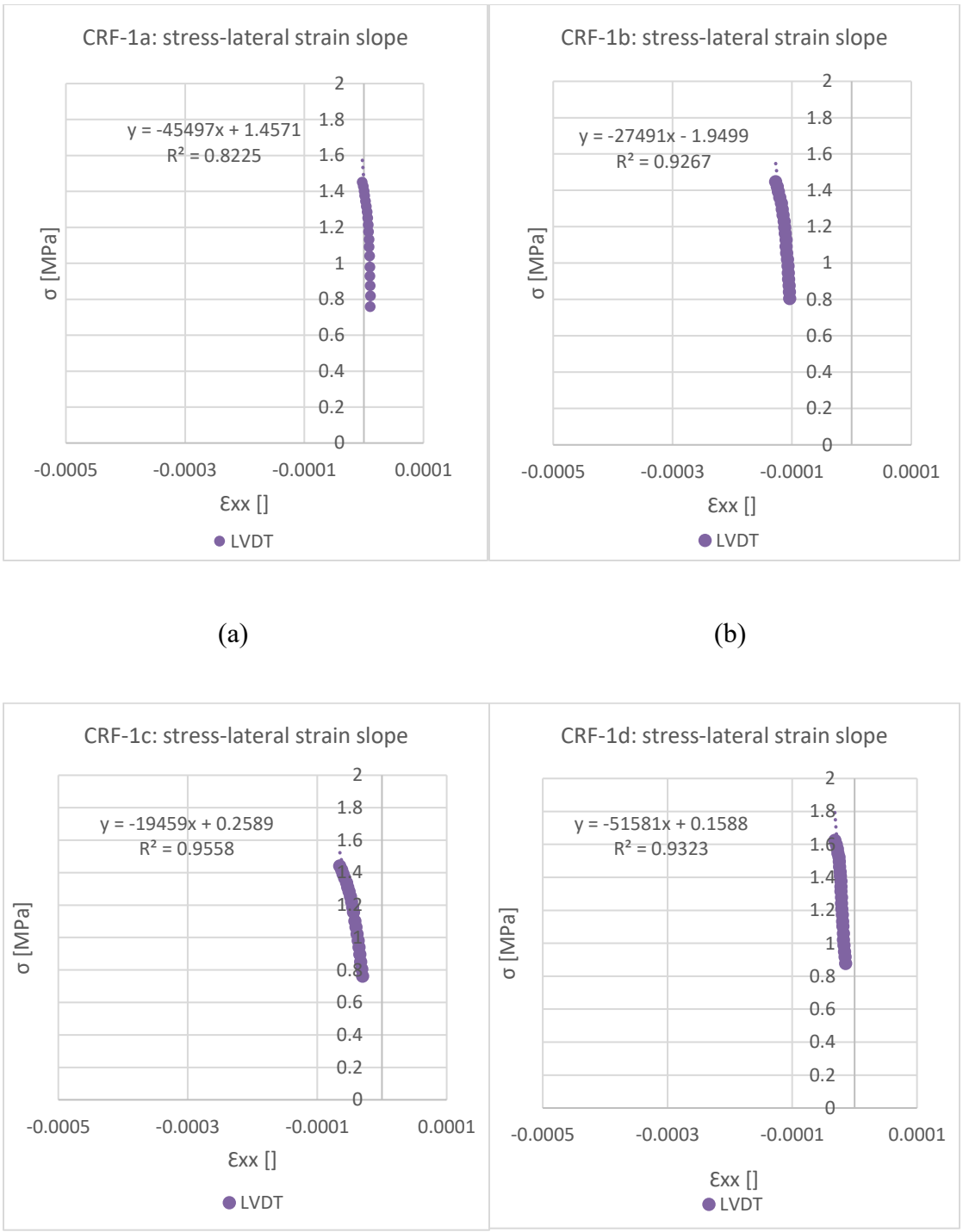

(a) (b)

(c) (d)

Figure 4.15. Linear line best-fit, stress-lateral strain slope determination

From corresponding stress-axial strain and stress-lateral strain each specimen slopes (Figure 4.14 and 4.15), the complete E and *v* are displayed in the following Table 4.2.

Table 4.2. Measured E and v of granite CRF

CRF 4.5%	**Contact method measurement**	
specimen#	**E (Gpa)**	***v***
CRF-1a	1.382	0.03038
CRF-1b	1.192	0.04336
CRF-1c	1.51	0.0776
CRF-1d	1.289	0.02499
mean	1.343	0.044
stdev	0.136	0.024
max	1.51	0.0776
min	1.192	0.02499
range	0.318	0.05261

4.4. Concluding observations

According to the results of this experiment, one stereovision system with five points of interests laid out its strain transcription in the same order as the conventional LDVT and string potentiometer methods. Mean differences of 5.1% and 14.5% were found for respectively lateral and axial strain differences between two methods. To the consideration of large specimen size, this difference would likely be acceptable. Therefore, the non-contact method is suitable for calculating the local strain of a large-scale specimen like CRF and suitable for investigating strain behavior around the crack.

Some accuracy limitation for out of plane strain recording of non-planar object by 3D-DIC system is pointed out. Out of plane strain of approximately 0.0005 for non-planar object may be the minimum accurate strain that 3D-DIC can record.

The elasticity property of the first type of mixture, granite CRF-1, has been attained through the experiment. The measured elastic modulus is ranging from 1.192 to 1.51 GPa and the Poisson's ratio is from 0.025 to 0.078.

The user understanding and comprehension of what to examine in the experiment is strongly recommended. In general, non-contact method by 3D-DIC is preferred to be used for large scale specimen like CRF's local strain or crack development observations. However, elasticity properties of granite CRF may still be calculated by using conventional contact method.

References

ASTM C192/C192M (2016) 'Standard Practice for Making and Curing Concrete Test Specimens in the Laboratory', ASTM International, pp. 1–8.

ASTM C617/C617M − 12 (2012) 'Standard Practice for Capping Cylindrical Concrete Specimens', ASTM International, 98(Reapproved), pp. 1–6.

ASTM D7012-14 (2014) 'Standard test method for compressive strength and elastic moduli of intact rock core specimens under varying states of stress and temperatures', ASTM International, pp. 1–9. doi: 10.1520/D7012-14E01.

Belem, T., Benzaazoua, M. and Bussière, B. (2000) 'Mechanical behaviour of cemented paste backfill', in Proc. of 53rd Canadian Geotechnical Conference, Montreal. Montreal, pp. 373–380.

Chu, T. C., Ranson, W. F. and Sutton, M. A. (1985) 'Applications of digital-image-correlation techniques to experimental mechanics', Experimental Mechanics, 25(3), pp. 232–244.

Correlated Solutions (2010) Vic-3D 2010 Reference Manual.

Correlated Solutions (2017) Correlated Solutions – Products. Available at: http://correlatedsolutions.com/products/ (Accessed: 22 November 2017).

Helm, J. D., Sutton, M. A. and McNeill, S. R. (1996) 'Improved three-dimensional image correlation for surface displacement measurement', Society of Photo-Optical Instrumentation Engineers, 35(7), pp. 1911–1920. Available at: http://opticalengineering.spiedigitallibrary.org/article.aspx?doi=10.1117/1.600624.

Lu, H., Vendroux, G. and Knauss, W. G. (1997) 'Surface deformation measurements of a cylindrical specimen by digital image correlation', Experimental Mechanics, 37(4), pp. 433–439.

Luo, P. F. et al. (1993) 'Accurate measurement of three-dimensional deformations in deformable and rigid bodies using computer vision', Experimental Mechanics, 33(2), pp. 123–132.

Meyers, B. L. (1969) 'Relationship between Time-Dependent Deformation and Microcracking of Plain Concrete', ACI Journal Proceedings, 66(1). Available at:

http://www.concrete.org/Publications/ACIMaterialsJournal/ACIJournalSearch.aspx?m=details&ID=7342.

Peters III, W. H. et al. (1989) ‘Whole-field experimental displacement analysis of composite cylinders’, Experimental Mechanics, 29(1), pp. 58–62.

SANTOS, A. H. A. et al. (2016) ‘Concrete modulus of elasticity assessment using digital image correlation’, Revista IBRACON de Estruturas e Materiais, 9(4), pp. 587–594. Available at: http://www.scielo.br/scielo.php?script=sci_arttext&pid=S1983-41952016000400587&lng=en&tlng=en.

Sutton, M. A. et al. (2008) ‘The effect of out-of-plane motion on 2D and 3D digital image correlation measurements’, Optics and Lasers in Engineering, 46(10), pp. 746–757.

Chapter 5: Study on Shear Properties of Cemented Rockfill[4]

5.1. Introduction

Backfill utilization has been necessary for the recent underground mining sector. As economic resources are being found deeper due to the fact that surface reserves are almost mined out; therefore, backfill utilization even incorporates binder material such as cement to provide more strength. While a number of studies have carried out investigations on compression and tension strengths of cemented backfills, there have not yet been studies on the shear properties and strength of backfill. However, in regards to backfill as a stability support, one has stated, there is no really useful stability analysis for design if the shearing strength of the product has been calculated incorrectly (Marachi, Chan, & Seed, 1972).

In many Canadian underground mines, the use of cemented rockfill as backfill material is a common practice (Emad et al., 2012; Reschke, 1993; Shrestha et al., 2008; T. R. Yu & Counter, 1983). Especially in cut-and-fill or blasthole stoping operations, which are usually divided by primary and secondary stopes, shear properties play an important role. While working on filling the primary stopes, shear interactions occur between the adjacent ore or rock walls and the placed CRF. A number of studies have verified that the interaction may be mutually supported (Tikov Belem & Benzaazoua, 2008; Mitchell, 1989). On the other hand, mining advancement from primary to secondary stopes are supposed to exhibit shear interaction

[4] This Chapter has been prepared and will be submitted in the meantime as a journal article, with the prepared title: Study of Shear Properties on Cemented Rockfill.

between primary CRF and placed CRF at the secondary stope. Therefore, this experiment's purpose is to assess the CRF-CRF shear interaction.

Shear interaction in the case of CRF can be separated into interface between CRF-CRF and interparticle of CRF by means of the mass. The adoption of shear interaction between CRF-CRF interfaces has been explained in the previous paragraph. A case of sliding failure on the CRF's free-face during the adjacent ore extraction could be the shear interaction between interparticle or CRF mass. Figure 5.1 shows the mining sequence where the shear interactions of CRF mostly take place.

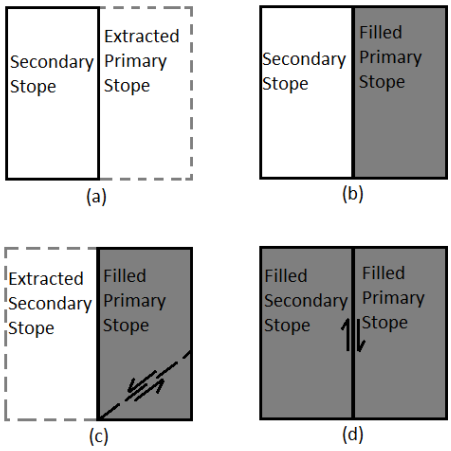

Figure 5.1. Mining sequence: (a) primary stope mined, (b) primary stope after backfilling, (c) secondary stope mined and generated interparticle or CRF mass shear at exposed primary stope, (d) Secondary stope after backfilling with CRF-CRF interface shear interaction

In rock engineering practice, these two shear interactions are simply the shear of discontinuity and shear of an unbroken material. Based on this fact, the direct shear and triaxial tests may be used to investigate the shear properties of CRF. Despite the triaxial test of CRF not commonly being conducted due to the limited availability of a large triaxial cell for accommodating CRF sample size, this study delivers triaxial results of 152.4 mm (6 in) in diameter CRF samples.

Direct shear strength of CRF-CRF interface in this study is based on a flat and smooth surface approach. Samples in this study are laboratory-created CRF of granite aggregate rock retrieved from a diamond mine in Northern Canada.

Noted that this study treats CRF as a solid mass instead of loose aggregate accumulation. CRF incorporates a binder which in setting the CRF behaves like concrete or rock more than regular compacted or non-compacted rockfill. This understanding is important to clarify Barton's shear strength criteria (2013, 2016) that is used later in this study. Experimental work in this study follows Barton's shear strength of rock joints experiment instead of his shear strength of rockfill interfaces experiment, which was about loose or non-cemented rockfill.

Direct shear and triaxial tests were conducted on two different types of specimens. In this experiment, each sample was tested after 28-day curing age. This time was selected so that the CRF should completely set and represent its optimum shear strength. Further details are explained in the following sections.

5.2. Theory, Material and Experimentations

5.2.1. Shear Strength Criteria

Theoretically, a rock's shear strength is expressed with the Coulomb relationship:

$$\tau = c + \sigma \tan \varphi \quad \text{.....Eq.5.1.}$$

where τ, c, σ, and ø are shear strength, cohesion, normal stress and internal friction angle respectively. For rock joints, it is theoretically preferred to use the above equation without cohesion value, thus the Equation 5.1 for rock joints becomes:

$$\tau = \sigma \tan \varphi \quad \text{.....Eq.5.2.}$$

However, Equation 5.2 only meets the criteria when any joint's contact is smooth, clean, and planar. Then, the generated shear strength envelope is supposed to be linear. However, in reality, any naturally occurring joint is most likely undulating. In addition is the fact that envelope plotting from the experimental shear strength test is also non-linear.

Various empirical approximations predicting the non-linearity of a rock joint's shear strength envelope due to its naturally non-planar characteristic with curve-fitting were found to be more reliable. The initial attempts to interpret the shear strength of rough joints resulted in a bilinear model of shear strength envelope (Newland & Allely, 1957; Patton, 1966), given with Equation 5.3:

$$\tau = \sigma_n' \tan(\varphi_b + i) \quad \text{.....Eq.5.3.}$$

Where σ_n', $ø_b$, and i are effective normal stress, basic friction angle, and asperity inclination angle.

Patton configured the relationship between deviation of the shear strength envelope of a joint and $ø_b$ plus i. The experiment of a wide range of normal stress variations toward a non-planar (artificially controlled undulation) interface sample resulting in a deviating shear envelope plot compared with the smooth surface proved Patton's hypothesis.

Further development of the non-linear shear strength envelope of a joint from bilinear to be more precise as curvilinear had been claimed (Bandis et al., 1981; Barton, 1973, 1976, 2013, 2016; Barton & Bandis, 1982; Barton & Choubey, 1977):

$$\tau = \sigma_n' \tan\left[JRC\left(\log_{10}{}^{JCS}/_{\sigma_n'}\right) + \varphi_b\right] \quad \text{.....Eq.5.4.}$$

$$\tau = \sigma_n' \tan\left[JRC\left(\log_{10}{}^{JCS}/_{\sigma_n'}\right) + \varphi_r\right] \text{.....Eq.5.5.}$$

$$\tau = \sigma_n' \tan\left[JRC_n\left(\log_{10}{}^{JCS_n}/_{\sigma_n'}\right) + \varphi_r\right] \text{.....Eq.5.6.}$$

Equation 5.4 has JRC (joint roughness coefficient) and JCS (joint-wall compression strength), which are the first two terms that are introduced by Barton on his earlier study. On the development, consideration upon weathering of the natural joint and the difference between a prepared flat surface and natural surface due to residual shear, Barton and Choubey substituted $ø_b$ in Equation 5.4 with $ø_r$ (residual friction angle) as in Equation 5.5. Further, Equation 5.6 developed by Bandis et al. after Barton and Choubey used JRC_n and JCS_n to take into account the field scale effect as the derivative of JRC and JCS.

Barton explained the curvilinearity of the shear strength envelope was affected by how rock behaves under stress. A series of triaxial tests indicated the brittle-ductile behaviour of rock as elastoplastic material bends the shear strength envelope (see Figure 5.2).

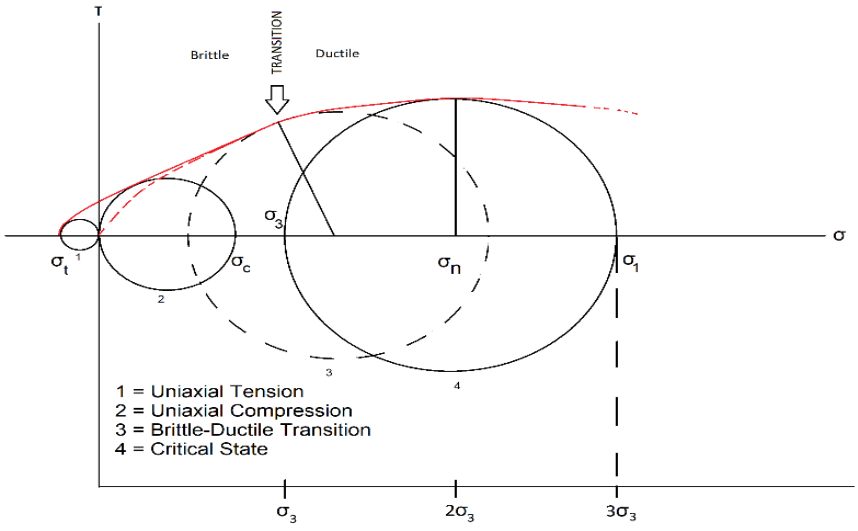

Figure 5.2. Bending of shear strength envelope due to brittle-ductile transition obtained from triaxial tests result, after Barton (2013)

Zhao (1997) proposed an equation (Equation 5.7) based on Barton and Choubey's model (Equation 5.5) by adding a correction factor of interface matching factor or joint matching factor (JMC) to the JRC. He considered the field condition when usually the joint interface is not completely matching as a fresh joint. Therefore, he also used the term residual friction angle instead of basic friction angle.

$$\tau = \sigma_n' \tan\left[JMC.JRC\left(\log_{10}{}^{JCS}/_{\sigma_n'}\right) + \varphi_r\right] \quad \text{.....Eq.5.7.}$$

5.2.2. Cemented Rockfill Specimen

To meet the standard sample size regarding the nominal maximum aggregate size, the mold with a diameter to length ratio of 152.4 x 304.8 mm (6 x 12 in) was used (ASTM C192/C192M, 2016). Prepared samples for the triaxial test were then stored at the moisture chamber with 95 to 100% humidity and 25+-2^{o} C temperature, while the samples for the direct shear test were placed indoors. The purpose of dry cured direct shear samples was to mimic the field condition when joints are mostly dry due to air exposure. As suggested by Barton (1976), the surface condition for the test may be dry or wet according to the desired application, and Zhao (1997) also did his experiment with dry samples.

5.2.3. Load Frame and Experimentation

5.2.3.1.Triaxial Apparatus and Testing

In university of Alberta, Rock Mechanics laboratory, a special fabricated 152.4 mm (6 in) in diameter Hoek Triaxial Cell by RocTest (2017) was used to accommodate triaxial samples on this study. The loading frames incorporated a 1,000 ton capacity servo-hydraulic INSTRON machine to generate the axial load and a syringe hydraulic pump ISCO Model 100DX to

provide the confining pressure. Data gathered from the test was recorded by a data acquisition system. Figure 5.3 shows the triaxial cell on the loading frame that was used in the experiment.

Figure 5.3. 154.2 mm Diameter Hoek triaxial cell and 1,000 ton capacity loading frame INSTRON

The experiment generally followed standard method A (ASTM D7012-14, 2014). The test was run on a controlled 0.3 mm axial displacement per minute setup until the specimen reached failure. Three samples each of CRF-1 and CRF-2 were tested under different confining pressures.

5.2.3.2.Direct Shear Apparatus and Testing

The test utilized the Golder Association direct shear machine with constant normal load (CNL) (Hencher & Richards, 1982) in the same laboratory (see Figure 5.4). The machine incorporated

one linear position (LP) transducer for normal displacement, two LP transducers for shear displacement, and one pressure transducer for the shear stress. The two horizontal LP transducer were each placed at one side of the yoke. Test outcomes of three LP transducers and one pressure transducer were automatically recorded by the data acquisition system.

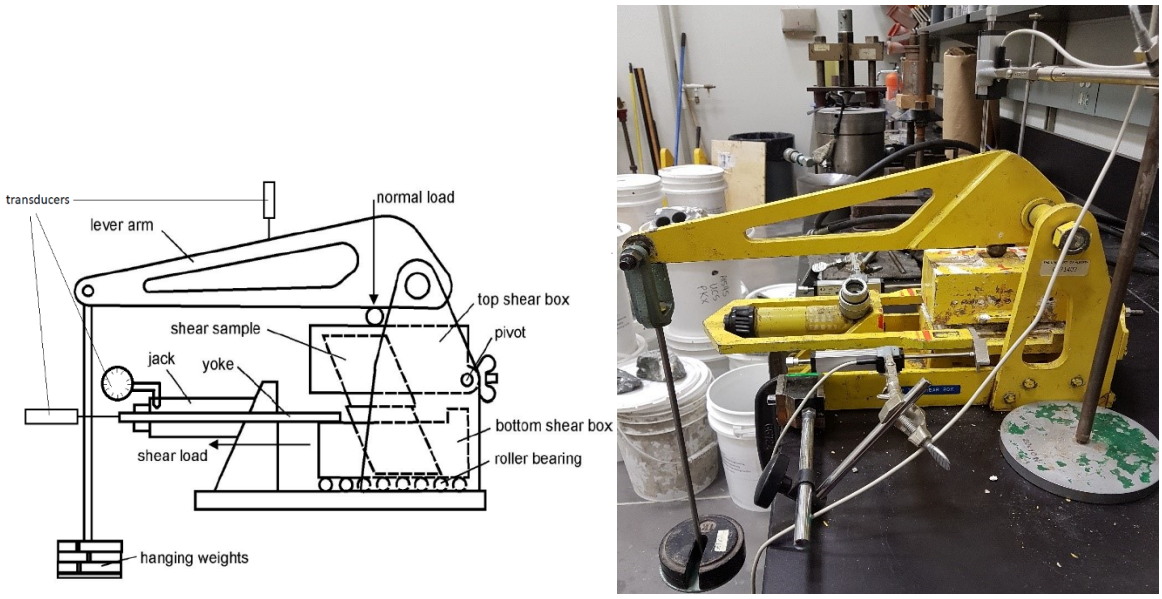

(a) (b)

Figure 5.4. Direct shear machine: (a) schematic, (b) actual direct shear apparatus

With respect to the limited dimensions of the shear box apparatus, all direct shear samples were further prepared to fit the shear box. Dry-cured cylindrical samples were then cut to be rectangular bars with a 78 x 127 mm flat and smooth contact area. The shear direction traveled along the longest cross-sectional dimension. Following the standard (ASTM D5607-16, 2016) that 10 times of the maximum asperity height along the shear surface should be the minimum least cross-sectional areas, the experiment's prepared smooth and flat sample's interface (i.e. with asperity height approaching zero) should satisfy. Bonding the specimen to the shear box utilized plaster of Paris as the encapsulating material.

The experiment applied the multistage direct shear test with the repositioning procedure to create three plots of shear-normal stress paths from each of the two samples of CRF-1 and CRF-2. The decreasing nominal contact area whether because of increasing shear displacement during each test or catastrophic damages from the previous test-stage was taken into account for the calculation of effective stress. The expected experimental result should be best described by Figure 5.5, a suggested method for rock joints direct shear test in the laboratory by Muralha et al. (2014), indicating a slight inclination of shear stress along each test-stage as the effect of decreasing contact area.

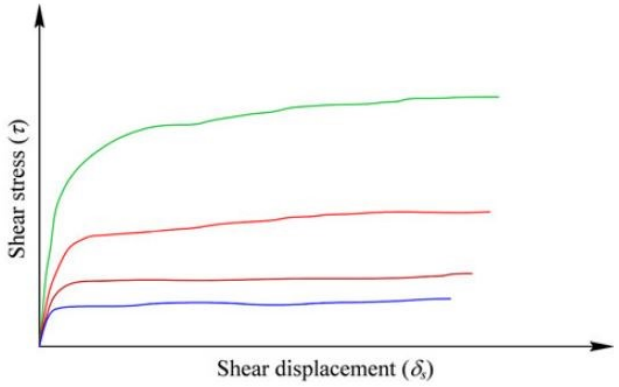

Figure 5.5. Example of multi-stage shear test under different CNL with repositioning after Muralha et al. (2014)

5.3. Result and Discussions

5.3.1. Interparticle Shear Strength of CRF

A set of triaxial tests were conducted for a total of six samples, three samples of each CRF type. Additional unconfined compressive strength (UCS, σ_c) of each CRF type was also included in the triaxial plotting (taken from the results in Chapter 2) to add one more Coulomb circle. The previous tests in Chapter 2 resulted in σ_c of CRF-1 and CRF-2 were 3.39 and 9.22 MPa respectively. The σ_c was also used for the next triaxial tests' confining pressure (σ_3)

determinations, as the following triaxial tests' σ_3 was supposed to not exceed 45% of the σ_c value. In addition, σ_c was also used as the JCS value of Barton's shear strength input in the next section of this study.

Table 5.1 shows the result of triaxial tests of the experiment. Further, the CRF interparticle shear strength envelope is generated with the Coulomb relationship based on Equation 5.1 using RocData 5.0 Software. The software is used to find the best fit shear strength envelope of each CRF (see Figures 5.6 and 5.7).

Table 5.1 Triaxial test results data

	# of Test	CRF-1			CRF-2		
		σ_3 (MPa)		σ_1 (MPa)	σ_3 (MPa)		σ_1 (MPa)
		Set	Actual		Set	Actual	
Specimen testing	1	0	0	3.39	0	0	9.22
	2	0.75	0.74	8.55	1.5	1.49	19.41
	3	1	1.05	10.93	2.5	2.57	22.24
	4	1.5	1.49	12.16	3.5	3.49	28.25
RocData 5.0	C	0.761			2.163		
	Ø(°)	45.9			42.78		

Best-fit cohesions and internal friction angles from RocData are then put into Equation 5.1 to model the Coulomb relationship of both shear strength envelopes of interparticle CRF as follows:

$\tau_{CRF-1} = 0.761 + \sigma \tan 45.90^{o}$ .....Eq.5.8.

$\tau_{CRF-2} = 2.163 + \sigma \tan 42.78^{o}$ .....Eq.5.9.

The triaxial result assessed with the Coulomb relationship for the CRF gives an understanding of interparticle shear strength of CRF-1, which has a cohesion of 0.761 MPa and internal

friction angle of 45.90°; CRF-2 has c equal to 2.163 MPa and ø equal to 42.78°. For the same aggregate size and proportion but different material strength (CRF-1 < CRF-2), it is indicated that CRF-1 has a slightly higher internal friction angle than CRF-2, but CRF-1 has a lower cohesion than CRF-2.

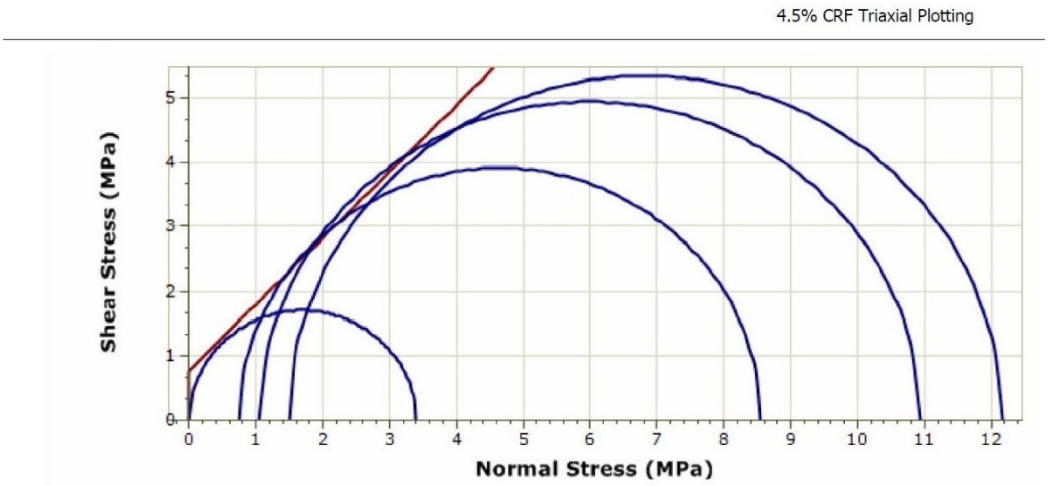

Figure 5.6. Interparticle shear strength envelopes of CRF-1 by RocData

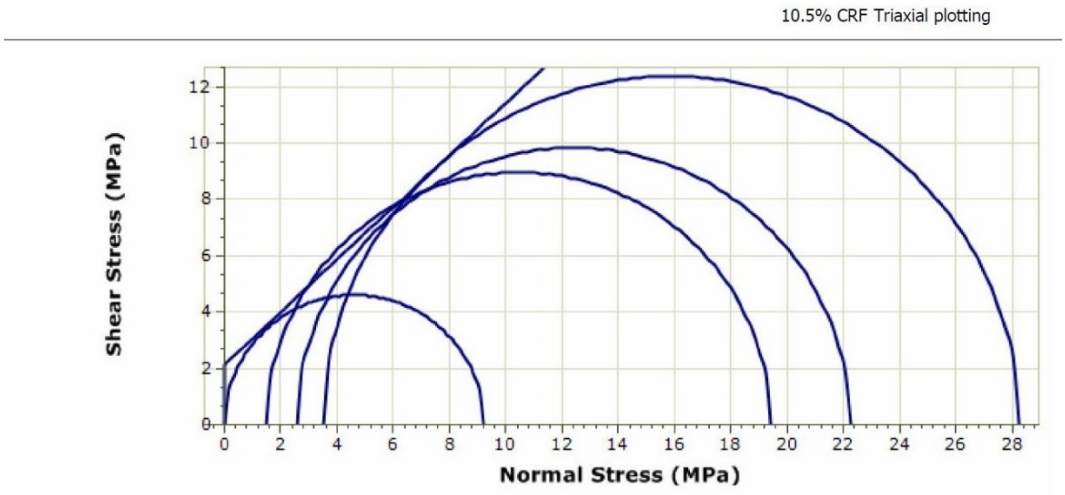

Figure 5.7. Interparticle shear strength envelopes of CRF-2 by RocData

The failure mode of CRF under the shear triaxial test indicated a high angle of failure plane. The high angle of failure plane occurred not only to CRF-1 but also to CRF-2. The following Figure 5.8 shows the failure angle resulting from the experiment. The CRF-1 specimen is on the left and the CRF-2 is on the right side of the figure.

Figure 5.8. Mode of failure of CRF under triaxial test

5.3.2. Interface Shear Strength of CRF-CRF

The three stages of direct shear tests with the applied normal loads respectively are 1 kN, 1.6 kN, and 2 kN assessed for a total of four direct shear samples. Generated normal load from the hanging weights are assumed giving the uniform normal load to the nominal area throughout the test. The plots of shear stress-displacement are shown on Figure 5.9, 5.10, 5.11, and 5.12. The resulted plots are very similar with the work of Muralha et al. (Figure 5.5). Figure 5.13 shows the final plotting of shear strength envelopes from direct shear test results.

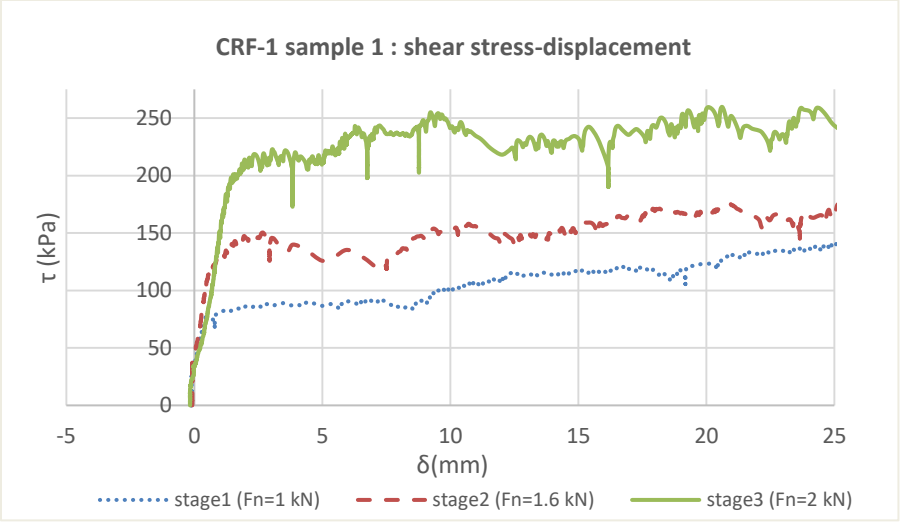

Figure 5.9. Shear stress-displacement of CRF-1 sample 1

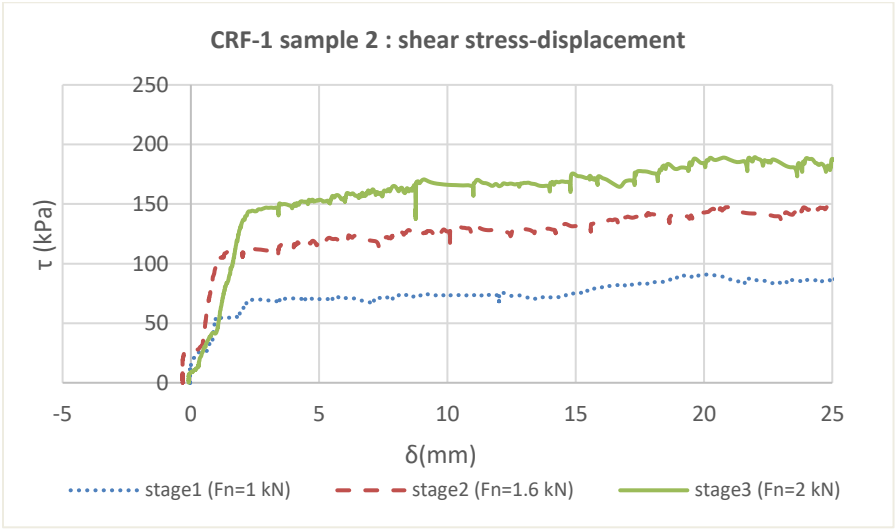

Figure 5.10. Shear stress-displacement of CRF-1 sample 2

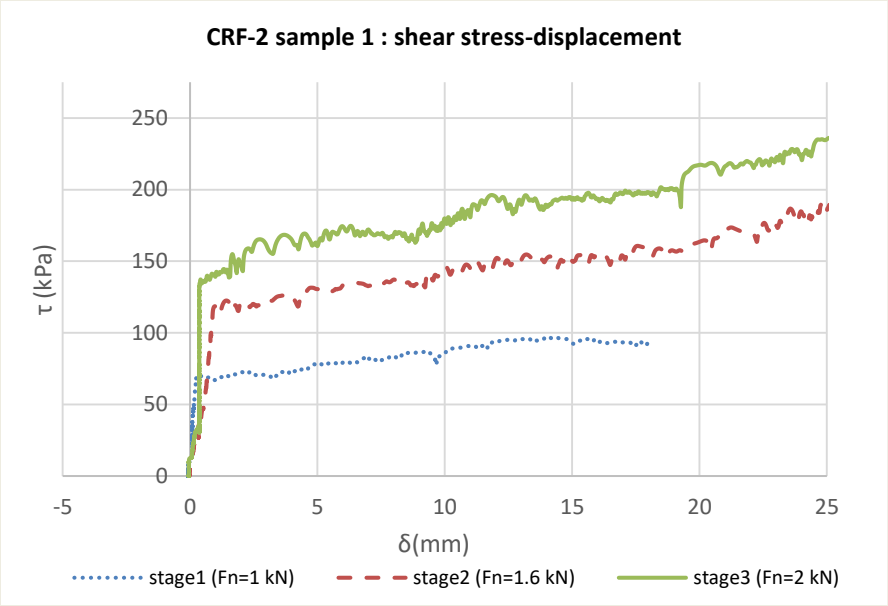

Figure 5.11. Shear stress-displacement of CRF-2 sample 1

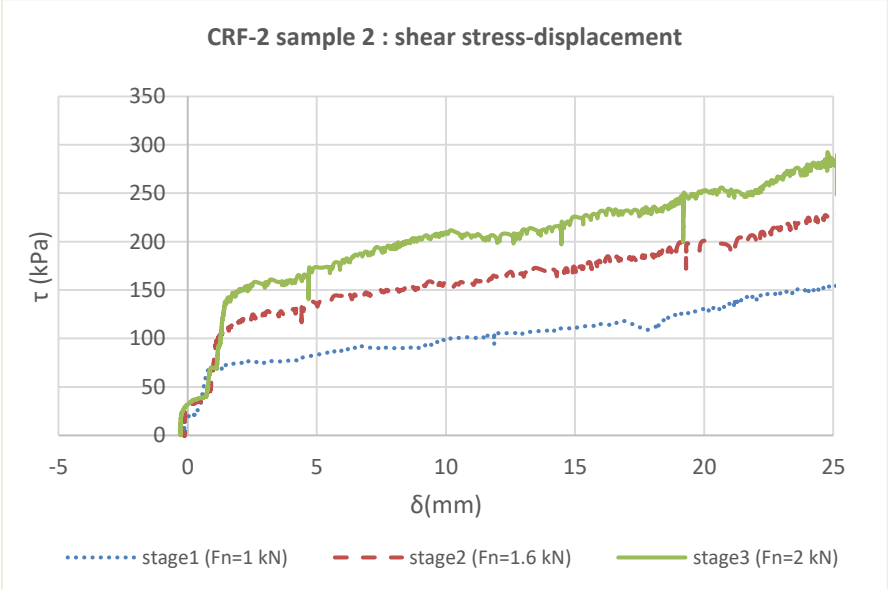

Figure 5.12. Shear stress-displacement of CRF-2 sample 2

Thus, the shear strength envelopes of the flat and smooth interfaces of CRF-CRF based on Equation 5.2 in terms of σ_n' and $\o_b$ are:

$\tau_{CRF-1} = \sigma_n' \tan \varphi_{b_1}$ or $\tau_{CRF-1} = \sigma_n' \tan 39.91^o$ .....Eq.5.10.

$\tau_{CRF-2} = \sigma_n' \tan \varphi_{b_2}$ or $\tau_{CRF-2} = \sigma_n' \tan 41.83^o$ .....Eq.5.11.

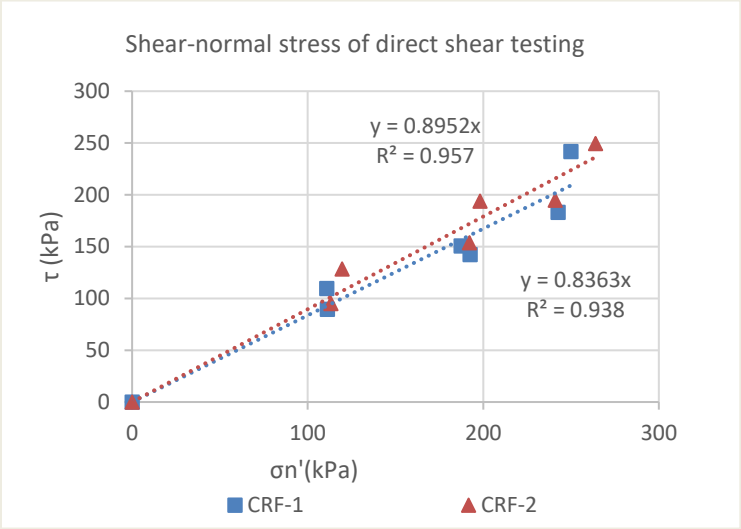

Figure 5.13. Shear strength envelopes of flat and smooth interfaces CRF-CRF

In this study, the assessment of Patton and Barton's shear strength criteria were approximated from the artificial tension fracture of corresponding CRF. Considering the nature of the particular CRF, binder-aggregate bonding in granite CRF was assumed weaker than the granite aggregate itself. Therefore, the natural joint of granite CRF may be identical to the artificial tension fracture, thereby satisfying with CRF-CRF interfaces as well.

Figure 5.14. *i* measurement using profiler

Table 5.2. *i* measurement data

i angle (°)						
#	CRF-1			CRF-2		
	Minimum	Maximum	Mean	Minimum	Maximum	Mean
1	21.38	65.39	43.385	9.42	54.98	32.2
2	7.79	49.21	28.5	5.53	28.59	17.06
3	11.97	30.79	21.38	16.45	41.49	28.97
4	23.65	54.62	39.135	24.15	28.94	26.545
5	23.84	55.1	39.47	9.53	45.44	27.485
6	24.02	43.47	33.745	12.39	37.81	25.1
7	15.77	63.07	39.42	9.61	57.59	33.6
8	9.61	43.97	26.79	18.81	40.31	29.56
9	13.9	56.9	35.4	7.64	58.64	33.14
10	8.57	30.58	19.575	15.58	32.09	23.835
11	10.96	44.56	27.76	15.59	34.78	25.185
12	18.19	30.31	24.25	9.21	70.13	39.67
13	11.34	43.02	27.18	12.64	66.34	39.49
14	20.55	64.69	42.62	15.38	58.96	37.17
15	11.35	58.36	34.855	13.05	52.85	32.95
Average			32.231			30.13

A set of asperity inclination angle (i) measurements were recorded using the profile gauge; captured and then computed using the software MB-Ruler to give more precision angle values, (see Table 5.2 and Figure 5.14). The average i value was then back-calculated to each CRF to model Patton's shear strength criteria. Combining the average i value with basic friction angle of each CRF from Equations 5.10 and 5.11 gave Patton's shear strength of CRF-CRF interfaces shown in Equations 5.12 and 5.13.

$\tau_{CRF-1} = \sigma_n' \tan(\varphi_{b_1} + i_1)$ or $\tau_{CRF-1} = \sigma_n' \tan(72.14^o)$.....Eq.5.12.

$\tau_{CRF-2} = \sigma_n' \tan(\varphi_{b_2} + i_2)$ or $\tau_{CRF-1} = \sigma_n' \tan(71.96^o)$.....Eq.5.13.

Clarifying Patton's model, Equations 5.12 and 5.13 respectively are basically the first part of the linear envelope of each CRF type; Equations 5.10 and 5.11 respectively are the second part of the linear envelope.

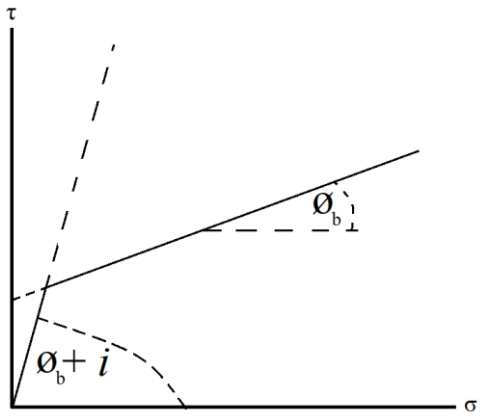

Figure 5.15. Patton's bilinear shear strength envelope

This CRF-CRF "smooth and planar interface" experiment indicates a limitation in modelling Patton's bilinear shear strength criteria in terms of the intersection point between the two linear envelopes determination (see illustration in Figure 5.15). Nevertheless, this direct shear of

smooth and planar together with tensile fracture asperity inclination measurements of CRF-CRF interface still can produce $ø_b$, and *i*.

While Patton's experiment claimed that $ø_r$ was compared favourably with $ø_b$ (always within 1.5° of $ø_b$) and both were often identical, the author's study of CRF attempted to model the $ø_r$ with Barton and Choubey's $ø_r$ estimation formula (Equation 5.14). Where r and R are the Schmidt rebound number on wet joint surfaces and dry flat-smooth surfaces, respectively.

$$\varphi_r = (\varphi_b - 20) + 20\left({}^{r}/_{R}\right) \quad \text{.....Eq.5.14.}$$

Table 5.3. Schmidt rebound number measurement data

#	CRF-1						CRF-2					
	r			R			r			R		
	Set 1	Set 2	Set 3	Set 1	Set 2	Set 3	Set 1	Set 2	Set 3	Set 1	Set 2	Set 3
1	=<10	=<10	=<10	=<10	=<10	=<10	10	10	10	10	14	10
2	=<10	=<10	=<10	=<10	=<10	=<10	11	12	11	11	16	11
3	=<10	=<10	=<10	=<10	=<10	=<10	11	13	11	15	17	14
4	=<10	=<10	=<10	=<10	=<10	=<10	11	13	12	16	17	15
5	=<10	=<10	=<10	=<10	=<10	=<10	11	14	12	20	20	16
6	=<10	=<10	=<10	=<10	=<10	=<10	14	15	12	20	20	18
7	=<10	=<10	=<10	=<10	=<10	=<10	15	15	13	20	21	18
8	=<10	=<10	=<10	=<10	=<10	=<10	18	17	14	20	22	18
9	=<10	=<10	=<10	=<10	=<10	=<10	18	19	16	22	23	22
10	=<10	=<10	=<10	=<10	=<10	=<10	22	19	20	22	26	30
Average of highest 5	10	10	10	10	10	10	17	17	15	21	22	21
Average	10			10			16			21		

A set of Schmidt rebound number measurements were conducted using a L-type PROCEQ concrete Schmidt Hammer and followed by averaging the highest five data as suggested by

Barton (2013, 2016) and Choubey (1977) (see Table 5.3). The correction for the average r and R values of CRF-1 were both 10. Here because of the particular test on CRF-1, neither r nor R could reach the smallest rebound number on the Schmidt, which was 10. Calculated using Equation 5.14, the residual friction angles of CRF-CRF interfaces 4 are:

$$\varphi_{r_{CRF-1}} = 39.91^{o} \quad \text{.....Eq.5.15.}$$

$$\varphi_{r_{CRF-2}} = 37.07^{o} \quad \text{.....Eq.5.16.}$$

The estimation of JRC was assessed using a surface profiler to interpret the artificial tension fracture's profile of both CRF, then by matching them into available graphic and chart methods (Barton & Choubey, 1977). The result simply gave a JRC of 20 (maximum value). A JRC value of 20 for this experiment seemed obvious considering the joint surfaces consisted of 50.8 mm or less coarse aggregate undulating out.

The JCS estimation was assumed equal to the UCS value as in Chapter 2, which was σ_c value. Therefore, combinations of residual friction angles (Equation 5.15 and 5.16), JRC values, and JCS values created Barton's shear strength of CRF-CRF interfaces shown next in Equation 5.17 and 5.18, where τ and σ_n' are in term of MPa.

$$\tau_{CRF-1} = \sigma_n' \tan\left[20\left(\log_{10} {}^{3.39}/_{\sigma_n'}\right) + 39.91^{o}\right] \quad \text{.....Eq.5.17.}$$

$$\tau_{CRF-2} = \sigma_n' \tan\left[20\left(\log_{10} {}^{9.22}/_{\sigma_n'}\right) + 37.07^{o}\right] \quad \text{.....Eq.5.18.}$$

Figure 5.16 is the extrapolation of Barton's shear strength envelopes of CRF-CRF interfaces in this study. The plot is extrapolated by using Equation 5.17 and 5.18.

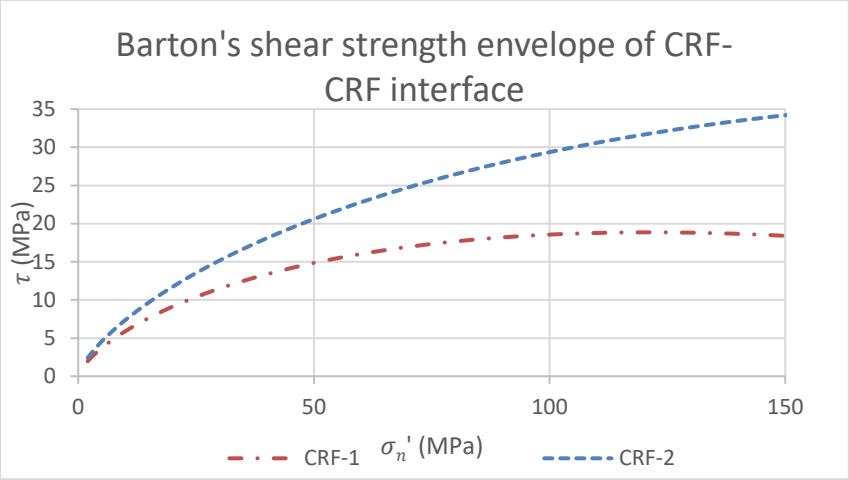

Figure 5.16. Barton's shear strength envelopes of CRF-CRF interfaces

Barton's shear strength assessment shows that the CRF-1 envelope is yielding earlier than CRF-2, i.e., CRF-1's transition zone is surpassed earlier than CRF-2 in the same effective normal stress state. In simple terms, CRF-2 is stronger than CRF-1. In the previous Patton's shear strength assessment, however, it is impossible to determine which CRF type has a higher shear strength because intersection points could not be determined while $ø_b$, and *i* were almost identical.

The situation is understandable because Barton's shear strength criteria is highly affected by JCS since the logarithmic function has to be multiplied by JRC. CRF-1 has JCS around one-third of CRF-2's JCS (CRF-1's σ_c=JCS=3.9 MPa; CRF-2's σ_c=JCS=9.22 MPa). Even when $ø_r$ and JRC between both are not significantly different, Barton's shear strength criteria and procedure are able to model the shear strength of the CRF-CRF interface from only the direct shear of smooth and planar surface testing.

Analysis of the basic and the residual friction angle differences of the CRF-1 experiments confirm with Patton's experiment where $ø_r$ and $ø_b$ are identical, although in the case of CRF-

2, $ø_r$ differs from $ø_b$ around 4.75° which is slightly off from 1.5°. It can be concluded that for granite CRF, $ø_r$ and $ø_b$ are likely not similar to each other.

A comparison between triaxial test results and direct shear test results are shown in Table 5.4. The experimental result confirms that the Barton shear strength assessment is successfully describing CRF shear property similar with the triaxial test. The shear strength of CRF-2 is higher than CRF-1 (in the triaxial test it is indicated by the higher cohesion; in Barton's it is indicated by the higher envelope), and the friction angle characteristic between them indicates that CRF-1 has a higher angle than CRF-2 (Barton's is denoted by residual friction angle).

Table 5.4. The shear properties of granite CRF Summary

		CRF-1	CRF-2	
Triaxial test	**C (MPa)**	0.761	2.163	Coulomb
	Ø (°)	45.9	42.78	
Direct shear test	**Ør (°)**	39.91	37.07	Barton
	Øb (°)	39.91	41.83	Patton
	Øb + i (°)	72.14	71.96	

5.4. Concluding observations

Some general conclusions can be drawn from the results of this study. First, shear behaviour of CRF in underground mining practices can be divided into two; CRF-CRF interface and CRF interparticle, which can be assessed with direct shear testing of CRF contacts and triaxial testing of intact CRF. Second, direct shear testing to assess shear strength envelopes of CRF-CRF interfaces can be done through testing on prepared flat and smooth CRF-CRF surfaces with conversions and corrections, preferably using Barton's shear strength criteria.

Two types of CRF with the same aggregate size and distribution but different unconfined compressive strengths indicate insignificant differences either between their basic friction angles or basic friction angle plus the asperity angle. But, the residual friction angle between both may be different. Therefore, it is preferred to use the residual friction angle instead of the basic friction angle in any shear strength assessment of jointed CRF.

There is an indication of CRF shear property where CRF is of different strengths but made from the same aggregate size and distribution: the stronger one tends to have a higher cohesion but a lower friction angle than the other.

References

ASTM C192/C192M (2016) ‘Standard Practice for Making and Curing Concrete Test Specimens in the Laboratory’, ASTM International, pp. 1–8.

ASTM D5607-16 (2016) ‘Standard Test Method for Performing Laboratory Direct Shear Strength Tests of Rock Specimens Under Constant Normal Force’, ASTM International, 4, pp. 1–9. doi: 10.1520/D5607-16.

ASTM D7012-14 (2014) ‘Standard test method for compressive strength and elastic moduli of intact rock core specimens under varying states of stress and temperatures’, ASTM International, pp. 1–9. doi: 10.1520/D7012-14E01.

Bandis, S., Lumsden, A. C. and Barton, N. R. (1981) ‘Experimental studies of scale effects on the shear behaviour of rock joints’, in International journal of rock mechanics and mining sciences & geomechanics abstracts, pp. 1–21.

Barton, N. (1973) ‘Review of a new shear-strength criterion for rock joints’, Engineering Geology, 7(4), pp. 287–332. doi: 10.1016/0013-7952(73)90013-6.

Barton, N. (1976) ‘Rock mechanics review. The shear strength of rock and rock joints’, International Journal of Rock Mechanics Mining Science and Geomechanics Abstract, 13.

Barton, N. (2013) ‘Shear strength criteria for rock, rock joints, rockfill and rock masses: Problems and some solutions’, Journal of Rock Mechanics and Geotechnical Engineering. Taibah University, 5(4), pp. 249–261. doi: 10.1016/j.jrmge.2013.05.008.

Barton, N. (2016) ‘Non-linear shear strength for rock, rock joints, rockfill and interfaces’, Innovative Infrastructure Solutions, 1(1), p. 30. doi: 10.1007/s41062-016-0011-1.

Barton, N. and Bandis, S. (1982) ‘Effects Of Block Size On The Shear Behavior Of Jointed Rock’. American Rock Mechanics Association.

Barton, N. and Choubey, V. (1977) ‘The shear strength of rock joints in theory and practice’, Rock Mechanics, 10(1–2), pp. 1–54. doi: 10.1007/BF01261801.

Belem, T. and Benzaazoua, M. (2008) 'Design and application of underground mine paste backfill technology', Geotechnical and Geological Engineering. doi: 10.1007/s10706-007-9154-3.

Emad, M. Z., Mitri, H. S. and Henning, J. G. (2012) 'Effect of blast vibrations on the stability of cemented rockfill', International Journal of Mining, Reclamation and Environment, 26(3), pp. 233–243.

Hencher, S. R. and Richards, L. R. (1982) 'The basic frictional resistance of sheeting joints in Hong Kong granite', Hong Kong Engineer, 11(2), pp. 21–25.

Marachi, N. D., Chan, C. K. and Seed, H. B. (1972) 'Evaluation of properties of rockfill materials', Journal of Soil Mechanics & Foundations Div, 98(1), pp. 95–114. Available at: http://cedb.asce.org/CEDBsearch/record.jsp?dockey=0127333.

Mitchell, R. J. (1989) 'Model studies on the stability of confined fills', Canadian Geotechnic Conference, 26, pp. 210–216. doi: 10.1139/t89-030.

Muralha, J. et al. (2014) 'ISRM Suggested Method for Laboratory Determination of the Shear Strength of Rock Joints: Revised Version', Rock Mechanics and Rock Engineering, 47(1), pp. 291–302. doi: 10.1007/s00603-013-0519-z.

Newland, P. L. and Allely, B. H. (1957) 'Volume changes during drained triaxial tests on granular materials', Geotechnique, 7, pp. 17–34. doi: 10.1680/geot.1957.7.1.17.

Patton, F. D. (1966) 'Multiple modes of shear failure in rock', 1st International Congress on Rock Mechanics, pp. 509–513.

Reschke, A. E. (1993) 'The use of cemented rockfill at Namew Lake mine, Manitoba, Canada', Minefill'93.

RocTest (2017) 'HTC - HOEK Triaxial Cell HTC - HOEK Triaxial Cell. Testing Equipment'. RockTest, pp. 1–2. Available at: https://roctest.com/wp-content/uploads/2017/01/E50011-160131-HTC-HOEK-Cell__.pdf.

Shrestha, B. K. et al. (2008) 'Properties of cemented rockfill used in an open pit mine', in GeoEdmonton'08. Edmonton: The Canadian Geotechnical Society. Available at: http://members.cgs.ca/documents/conference2008/GEO2008/pdfs/89.pdf.

Yu, T. R. and Counter, D. B. (1983) ‘Backfill practice and technology at Kidd Creek Mines’, CIM bulletin, 76(856), pp. 56–65.

Zhao, J. (1997) ‘Joint surface matching and shear strength part B.pdf’, 34(2), pp. 173–178. doi: 10.13732/j.issn.1008-5548.2005.04.002.

Chapter 6: Conclusions and Further Research

This research aims to deliver the complete strength and shear properties of granite cemented rockfill as it used at a Canadian diamond mine which with the aggregate source came from, through a laboratory scale experiment. In addition, this research also uses an unconventional testing technique and practical approach to give a new perspective on producing qualitative data from large-scale cemented rockfill samples due to testing impediments normally from the standard large size of specimens.

6.1. Conclusions

Details for the research on the subjects mentioned above can be found in their entirety from Chapter 2 to Chapter 5. To summarize, the findings, key observations, and conclusions of this research are:

1. In Chapter 2, the result of the particle size distribution analysis of experimental granite aggregate showed that the aggregate distribution is slightly rapid in the transition from coarse to fine size than the optimal theory of CRF aggregates. Experimental granite aggregate was shown to have a curvature control constant (n) value of 0.35.
2. In Chapter 3, compression and tensile strengths of two types of CRF were examined. From 7 to 28 days, CRF-1 strength is 1/3 of CRF-2 strength, which applies to both compressive and split tensile strengths. 28-day compressive and split tensile strength values of CRF-1 are about 3.39 MPa and 0.44 MPa respectively, and for CRF-2 are 9.22 MPa and 1.42 MPa. In the first week of age, CRF-1 compressive and split tensile strengths possess, respectively, 52.19% and 72.76% of their 28-day strength with a strength gain of 0.077 MPa and 0.0057 MPa on each day; CRF-2 respectively is

79.27% and 89.65% of its 28-day strength with a compressive and split tensile strength gain of 0.091 MPa and 0.007 MPa every day.

3. In Chapter 4, the elasticity property of the first type of mixture, granite CRF-1, was attained through the experiment. The measured elastic modulus ranged from 1.192 to 1.51 GPa and the Poisson's ratio from 0.025 to 0.078. The proposed non-contact technique in displaying CRF granite strain may be used as local strain observation tools. Nevertheless, this experiment pointed out an indicated minimum accurate strain that 3D-DIC could measure from out of plane strain of non-planar object, which was 0.0005.
4. In Chapter 5, shear behaviour of the granite CRF-CRF interface and interparticle showed a conformity with Barton shear criteria and Coulomb criteria. Therefore, attaining shear properties from natural interface contact of CRF-CRF from conveniently prepared flat and smooth CRF-CRF surfaces based on Barton's conversions and corrections could be used in the granite CRF case. Together with the result from triaxial testing, the complete shear properties of the experimental granite CRF are:
    - CRF-1 joint interface shearing has basic friction angle equal to the residual friction angle (39.91^{o}); on the other hand, the CRF-2 basic friction angle is slightly lower (37.07^{o}), but its residual friction angle is higher (41.83^{o}). Shear within CRF-1 interparticle shows a cohesion of 0.761 MPa and a friction angle of 45.9^{o}; on the other hand, CRF-2 has higher cohesion (2.163 MPa) and a slightly lower friction angle (42.78^{o}).

- Two types of CRF with the same aggregate size and distribution but different unconfined compressive strengths indicate insignificant differences either between their basic friction angles or basic friction angle plus the asperity angle. However, the residual friction angle between both may be different. Therefore, it is preferred to use the residual friction angle instead of basic friction angle in any shear strength assessment of jointed CRF.
- There is an indication of CRF shear property in the case of CRFs with different strengths but made from the same aggregate size and distribution: the stronger one tends to have a higher cohesion but a lower friction angle than the other.

6.2. Future Research

This research has produced qualitative data on the properties of the particular granite cemented rockfill used at a diamond mine in Northern Canada. In addition to research findings that are applicable to granite cemented rockfill, some alternative applications for rockfill property research have been delivered with credible results. Hence, future research can focus on continuing to apply these research findings to be applied on any stability analysis starting from the mentioned literature. Research can be narrowed down further by conducting an investigation to CRF in the mine based on the stability result to validate the optimum utilization of the current CRF and make future designs or recommendations.

Bibliography

363, A. C. I. C. (2010). *363R-10 Report on High-Strength Concrete*. American Concrete Institute.

Agricola 1494-1555, G. (1950). *De re metallica / Georgius Agricola ; translated from the first Latin edition of 1556, with biographical introduction, annotations and appendices ... by Herbert Clark Hoover and Lou Henry Hoover*. (H. Hoover 1874-1964 & L. H. Hoover 1874-1944, Eds.). New York: Dover Publications.

Amaratunga, L. M., & Yaschyshyn, D. N. (1997). Development of a high modulus paste fill using fine gold mill tailings. *Geotechnical and Geological Engineering*, *15*(3), 205–219. https://doi.org/10.1007/BF00880825

Arioglu, E. (1984). Design aspects of cemented aggregate fill mixes for tungsten stoping operations. *Mining Science and Technology*, *1*(3), 209–214. https://doi.org/10.1016/S0167-9031(84)90414-6

ASTM C136. (2006). Standard Test Method for Sieve Analysis of Fine and Coarse Aggregates. *Annual Book of ASTM Standards*, 3–7. https://doi.org/10.1520/C0136

ASTM C192/C192M. (2016). Standard Practice for Making and Curing Concrete Test Specimens in the Laboratory. *ASTM International*, 1–8.

ASTM C33. (2003). Standard Specification for Concrete Aggregates. *ASTM International*, *i*(C), 11.

ASTM C496/C496M. (2011). ASTM C496 Standard Test Method for Splitting Tensile Strength of Cylindrical Concrete Specimens. *ASTM International*, 5. https://doi.org/10.1520/C0496

ASTM C617/C617M − 12. (2012). Standard Practice for Capping Cylindrical Concrete Specimens. *ASTM International*, *98*(Reapproved), 1–6.

ASTM D5607-16. (2016). Standard Test Method for Performing Laboratory Direct Shear Strength Tests of Rock Specimens Under Constant Normal Force. *ASTM International*,

4, 1–9. https://doi.org/10.1520/D5607-16.

ASTM D7012-14. (2014). Standard test method for compressive strength and elastic moduli of intact rock core specimens under varying states of stress and temperatures. *ASTM International*, 1–9. https://doi.org/10.1520/D7012-14E01.

Bandis, S., Lumsden, A. C., & Barton, N. (1981). Experimental studies of scale effects on the shear behaviour of rock joints. In *International journal of rock mechanics and mining sciences & geomechanics abstracts* (Vol. 18, pp. 1–21).

Barton, N. (1973). Review of a new shear-strength criterion for rock joints. *Engineering Geology*, *7*(4), 287–332. https://doi.org/10.1016/0013-7952(73)90013-6

Barton, N. (1976). Rock mechanics review. The shear strength of rock and rock joints. *International Journal of Rock Mechanics Mining Science and Geomechanics Abstract*, *13*.

Barton, N. (2013). Shear strength criteria for rock, rock joints, rockfill and rock masses: Problems and some solutions. *Journal of Rock Mechanics and Geotechnical Engineering*, *5*(4), 249–261. https://doi.org/10.1016/j.jrmge.2013.05.008

Barton, N. (2016). Non-linear shear strength for rock, rock joints, rockfill and interfaces. *Innovative Infrastructure Solutions*, *1*(1), 30. https://doi.org/10.1007/s41062-016-0011-1

Barton, N., & Bandis, S. (1982). Effects Of Block Size On The Shear Behavior Of Jointed Rock. American Rock Mechanics Association.

Barton, N., & Choubey, V. (1977). The shear strength of rock joints in theory and practice. *Rock Mechanics*, *10*(1–2), 1–54. https://doi.org/10.1007/BF01261801

Belem, T., & Benzaazoua, M. (2008). Design and application of underground mine paste backfill technology. *Geotechnical and Geological Engineering*. https://doi.org/10.1007/s10706-007-9154-3

Belem, T., Benzaazoua, M., & Bussière, B. (2000). Mechanical behaviour of cemented paste backfill. In *Proc. of 53rd Canadian Geotechnical Conference, Montreal* (pp. 373–380).

Montreal.

Chu, T. C., Ranson, W. F., & Sutton, M. A. (1985). Applications of digital-image-correlation techniques to experimental mechanics. *Experimental Mechanics*, *25*(3), 232–244.

Correlated Solutions. (2010). *Vic-3D 2010 Reference Manual*.

Correlated Solutions. (2017). Correlated Solutions – Products. Retrieved November 22, 2017, from http://correlatedsolutions.com/products/

Emad, M. Z. (2013). *Dynamic Performance of Cemented Rockfill under Blast-Induced Vibrations*. McGill University.

Emad, M. Z., Mitri, H. S., & Henning, J. G. (2012). Effect of blast vibrations on the stability of cemented rockfill. *International Journal of Mining, Reclamation and Environment*, *26*(3), 233–243.

Fall, M., Célestin, J. C., Pokharel, M., & Touré, M. (2010). A contribution to understanding the effects of curing temperature on the mechanical properties of mine cemented tailings backfill. *Engineering Geology*, *114*(3–4), 397–413. Retrieved from http://dx.doi.org/10.1016/j.enggeo.2010.05.016

Helm, J. D., Sutton, M. A., & McNeill, S. R. (1996). Improved three-dimensional image correlation for surface displacement measurement. *Society of Photo-Optical Instrumentation Engineers*, *35*(7), 1911–1920. Retrieved from http://opticalengineering.spiedigitallibrary.org/article.aspx?doi=10.1117/1.600624

Hencher, S. R., & Richards, L. R. (1982). The basic frictional resistance of sheeting joints in Hong Kong granite. *Hong Kong Engineer*, *11*(2), 21–25.

Li, L., Aubertin, M., Belem, T., Simon, R., James, M., & Bussière, B. (2004). a 3D Analytical Solution for Evaluating Earth Pressures in Vertical Backfilled Stopes. In *Proceedings of 57th Canadian Geotechnical Conference and the 5th Joint CGS–IAH Conference* (pp. 24–27).

Lu, H., Vendroux, G., & Knauss, W. G. (1997). Surface deformation measurements of a

cylindrical specimen by digital image correlation. *Experimental Mechanics*, *37*(4), 433–439.

Luo, P. F., Chao, Y. J., Sutton, M. A., & Peters, W. H. (1993). Accurate measurement of three-dimensional deformations in deformable and rigid bodies using computer vision. *Experimental Mechanics*, *33*(2), 123–132.

Malešev, M., Radonjanin, V., Lukić, I., & Bulatović, V. (2014). The Effect of Aggregate, Type and Quantity of Cement on Modulus of Elasticity of Lightweight Aggregate Concrete. *Arabian Journal for Science and Engineering*, *39*(2), 705–711. https://doi.org/10.1007/s13369-013-0702-2

Marachi, N. D., Chan, C. K., & Seed, H. B. (1972). Evaluation of properties of rockfill materials. *Journal of Soil Mechanics & Foundations Div*, *98*(1), 95–114. Retrieved from http://cedb.asce.org/CEDBsearch/record.jsp?dockey=0127333

Maranha, E. (Ed.). (1990). *Advances in Rockfill Structures* (NATO ASI S). Lisbon, Portugal: Springer.

Meyers, B. L. (1969). Relationship Between Time-Dependent Deformation and Microcracking of Plain Concrete. *ACI Journal Proceedings*, *66*(1). Retrieved from http://www.concrete.org/Publications/ACIMaterialsJournal/ACIJournalSearch.aspx?m=details&ID=7342

Mitchell, R. J. (1989). Model studies on the stability of confined fills. *Canadian Geotechnic Conference*, *26*, 210–216. https://doi.org/10.1139/t89-030

Mitchell, R. J., Olsen, R. S., & Smith, J. D. (1982). Model studies on cemented tailings used in mine backfill. *Canadian Geotechnical Journal*, *19*, 14–28. https://doi.org/10.1139/t82-002

Mitchell, R. J., & Roettger, J. J. (1989). Analysis and modelling of sill pillars. *Innovations in Mining Backfill Technology. Balkema, …*, 53–61. Retrieved from http://scholar.google.com/scholar?hl=en&btnG=Search&q=intitle:Analysis+and+modelling+of+sill+pillars#0

Muralha, J., Grasselli, G., Tatone, B., Blümel, M., Chryssanthakis, P., & Yujing, J. (2014). ISRM Suggested Method for Laboratory Determination of the Shear Strength of Rock Joints: Revised Version. *Rock Mechanics and Rock Engineering*, *47*(1), 291–302. https://doi.org/10.1007/s00603-013-0519-z

Newland, P. L., & Allely, B. H. (1957). Volume changes during drained triaxial tests on granular materials. *Geotechnique*, *7*, 17–34. https://doi.org/10.1680/geot.1957.7.1.17

Oluokun, F. A., Burdette, E. G., & Deatherage, J. H. (1991). Splitting Tensile Strength and Compressive Strength Relationships at Early Ages. *ACI Materials Journal*, *88*(2), 115–121. Retrieved from http://www.concrete.org/Publications/ACIMaterialsJournal/ACIJournalSearch.aspx?m=details&ID=1859

Patton, F. D. (1966). Multiple modes of shear failure in rock. *1st International Congress on Rock Mechanics*, 509–513.

Peters III, W. H., Sutton, M. A., Ranson, W. F., Poplin, W. P., & Walker, D. M. (1989). Whole-field experimental displacement analysis of composite cylinders. *Experimental Mechanics*, *29*(1), 58–62.

Reschke, A. E. (1993). The use of cemented rockfill at Namew Lake mine, Manitoba, Canada. *Minefill'93*.

RocTest. (2017). HTC - HOEK Triaxial Cell HTC - HOEK Triaxial Cell. Testing Equipment. RockTest. Retrieved from https://roctest.com/wp-content/uploads/2017/01/E50011-160131-HTC-HOEK-Cell__.pdf

Sainsbury, D., & Sainsbury, B. (2014). Design and implementation of cemented rockfill at the Ballarat Gold Project. *Mine Fill 2014 Proceeding of the 11th International Symposium on Mining with Backfill*, (January 2014).

SANTOS, A. H. A., PITANGUEIRA, R. L. S., RIBEIRO, G. O., & CARRASCO, E. V. M. (2016). Concrete modulus of elasticity assessment using digital image correlation. *Revista IBRACON de Estruturas E Materiais*, *9*(4), 587–594. Retrieved from

http://www.scielo.br/scielo.php?script=sci_arttext&pid=S1983-41952016000400587&lng=en&tlng=en

Sepehri, M., Apel, D. B., & Hall, R. A. (2017). Prediction of mining-induced surface subsidence and ground movements at a Canadian diamond mine using an elastoplastic finite element model. *International Journal of Rock Mechanics and Mining Sciences*, *100*(October), 73–82.

Shrestha, B. K., Tannant, D. D., Proskin, S., & Greer, J. R. & S. (2008). Properties of cemented rockfill used in an open pit mine. In *GeoEdmonton'08*. Edmonton: The Canadian Geotechnical Society. Retrieved from http://members.cgs.ca/documents/conference2008/GEO2008/pdfs/89.pdf

Sinclair, T. J. E., Shillabeer, J. H., & Herget, G. (1982). Applications of a computer model to the analysis of rock-backfill interaction in pillar recovery operations. *International Journal of Rock Mechanics and Mining Sciences & Geomechanics Abstracts*, *19*(4), 83. https://doi.org/10.1016/0148-9062(82)90991-3

Sutton, M. A., Yan, J. H., Tiwari, V., Schreier, H. W., & Orteu, J. J. (2008). The effect of out-of-plane motion on 2D and 3D digital image correlation measurements. *Optics and Lasers in Engineering*, *46*(10), 746–757.

Swan, G. (1985). A new approach to cemented backfill design. *CIM Bulletin*, *78*(884), 53–58.

Talbot, A. N., & Richart, F. E. (1923). *The strength of concrete, its relation to the cement aggregates and water*. University of Illinois at Urbana Champaign.

Tesarik, D. R., Seymour, J. B., & Jones, F. M. (2003). Determination of in situ deformation modulus for cemented rockfill. In *10th ISRM Congress*. International Society for Rock Mechanics.

Vergne, J. (2003). *Rules of thumb for the hard rock mining industry*. (S. L. Andersen, Ed.), *Hard rock miner's handbook* (3rd ed.). Stantec Consulting.

Yu, T. R., & Counter, D. B. (1983). Backfill practice and technology at Kidd Creek Mines. *CIM Bulletin*, *76*(856), 56–65.

Yu, Y. S., & Toews, N. A. (1981). *Modelling of 830 Orebody of copper cliff south mine*.

Zhao, J. (1997). Joint surface matching and shear strength part B.pdf, *34*(2), 173–178. https://doi.org/10.13732/j.issn.1008-5548.2005.04.002

Zhu, Z. (2002). *Analysis of Mine Backfill Behaviour and Stability*. McGill.

Appendix of Chapter 3

		qc		qt	
CRF Type	Curing Age (day)	Samples (Mpa)	Mean (Mpa)	Samples (Mpa)	Mean (Mpa)
CRF-1	7	1.786	1.739	0.325	0.302
	7	1.514		0.253	
	7	1.918		0.327	
	14	2.503	2.357	0.364	0.374
	14	1.899		0.390	
	14	2.669		0.368	
	21	3.035		0.412	0.417
	21	2.655		0.389	
	21	2.845	2.845	0.450	
	28	3.451	3.351	0.408	0.410
	28	3.251		0.412	
CRF-2	7	7.069	7.294	1.240	1.305
	7	7.184		1.361	
	7	7.630		1.313	
	14	8.340	8.167	1.360	1.247
	14	7.994		1.134	
	21	7.969	8.196	1.431	1.380
	21	8.424		1.330	
	28	9.208	9.401	1.436	1.439
	28	9.594		1.443	

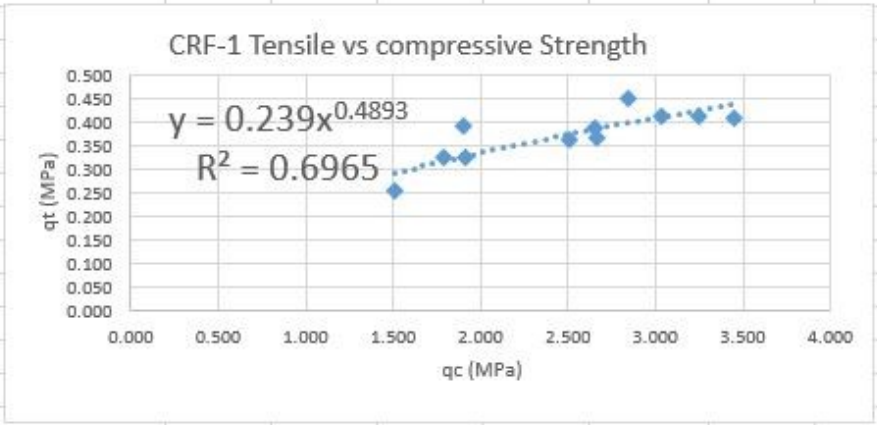

Table on the left shows the experimental data of STS and UCS result.

Charts on the right, each plot represents STS-UCS of corresponding CRF type from 7 to 28 days. The power trendline generated in the chart is an initial estimation and will be validated further with 'Solver' tool in Microsoft Excel.

K and R value determinations: Step 1

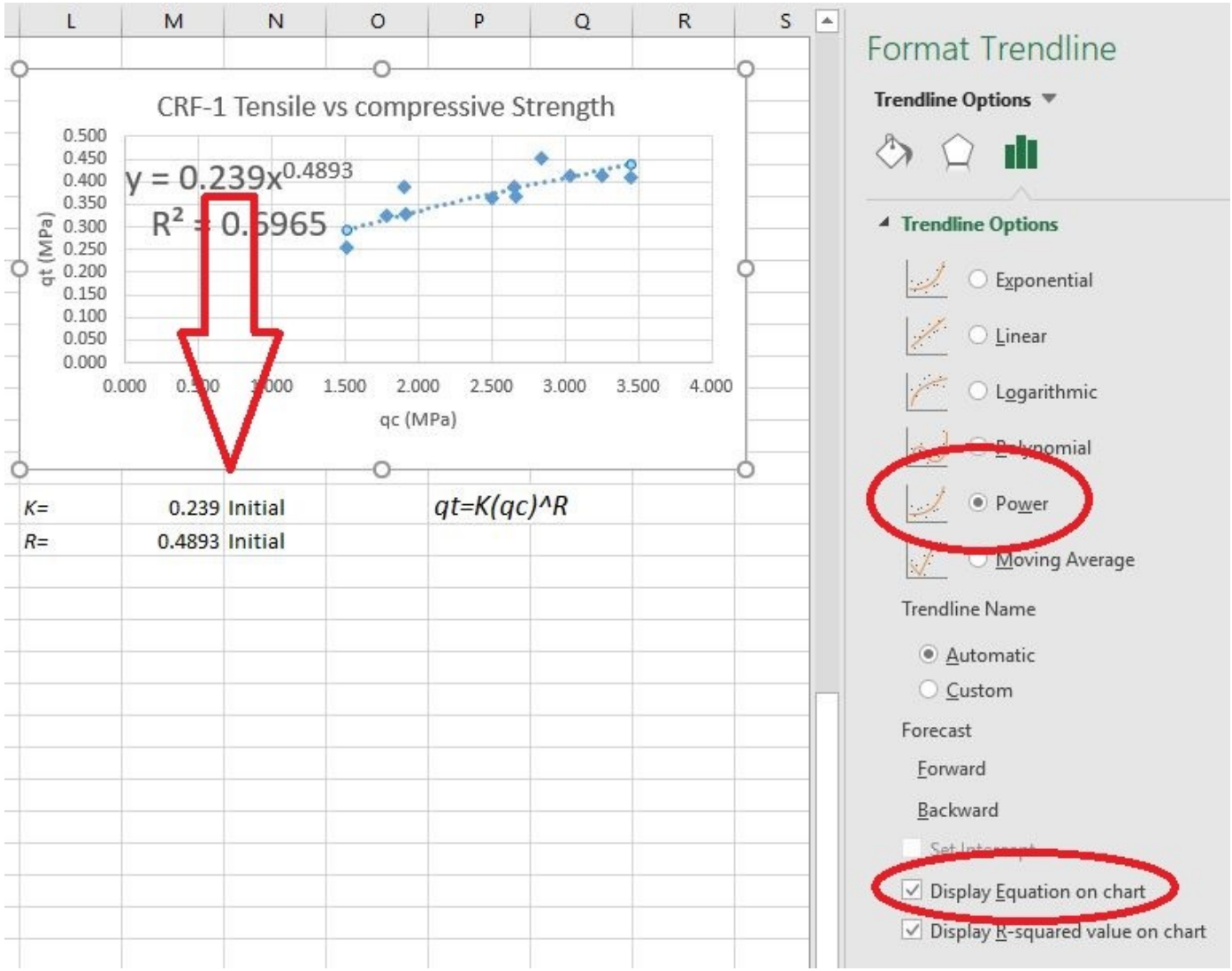

Step 2

	Curing Age	qc Samples	qc Mean	qt Samples	qt Mean	qt = y (with qc as x) MODEL
CRF Type	(day)	(Mpa)	(Mpa)	(Mpa)	(Mpa)	
CRF-1	7	1.786	1.739	0.325	0.302	0.317458114 =$M$68*C58^$M$69
	7	1.514		0.253		0.292761906
	7	1.918		0.327		0.328657008
	14	2.503	2.357	0.364	0.374	0.374445762
	14	1.899		0.390		0.327097815
	14	2.669		0.368		0.386392826
	21	3.035		0.412	0.417	0.411473049
	21	2.655		0.389		0.385383107
	21	2.845	2.845	0.450		0.398650875
	28	3.451	3.351	0.408	0.410	0.438141479
	28	3.251		0.412		0.425527669
CRF-2	7	7.069	7.294	1.240	1.305	
	7	7.184		1.361		
	7	7.630		1.313		
	14	8.340	8.167	1.360	1.247	
	14	7.994		1.134		
	21	7.969	8.196	1.431	1.380	
	21	8.424		1.330		
	28	9.208	9.401	1.436	1.439	
	28	9.594		1.443		

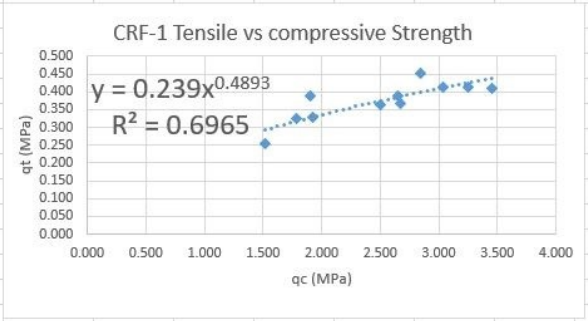

K=	0.239	Initial	*qt=K(qc)^R*
R=	0.4893	Initial	
minimum=	0.009785	=SUMPRODUCT(E58:E68-G58:G68,E58:E68-G58:G68)	Initial

The 'minimum' is the vector difference between qt model and samples. Later, Solver tool usage are intented to more reduce this 'minimum' value

Step 3

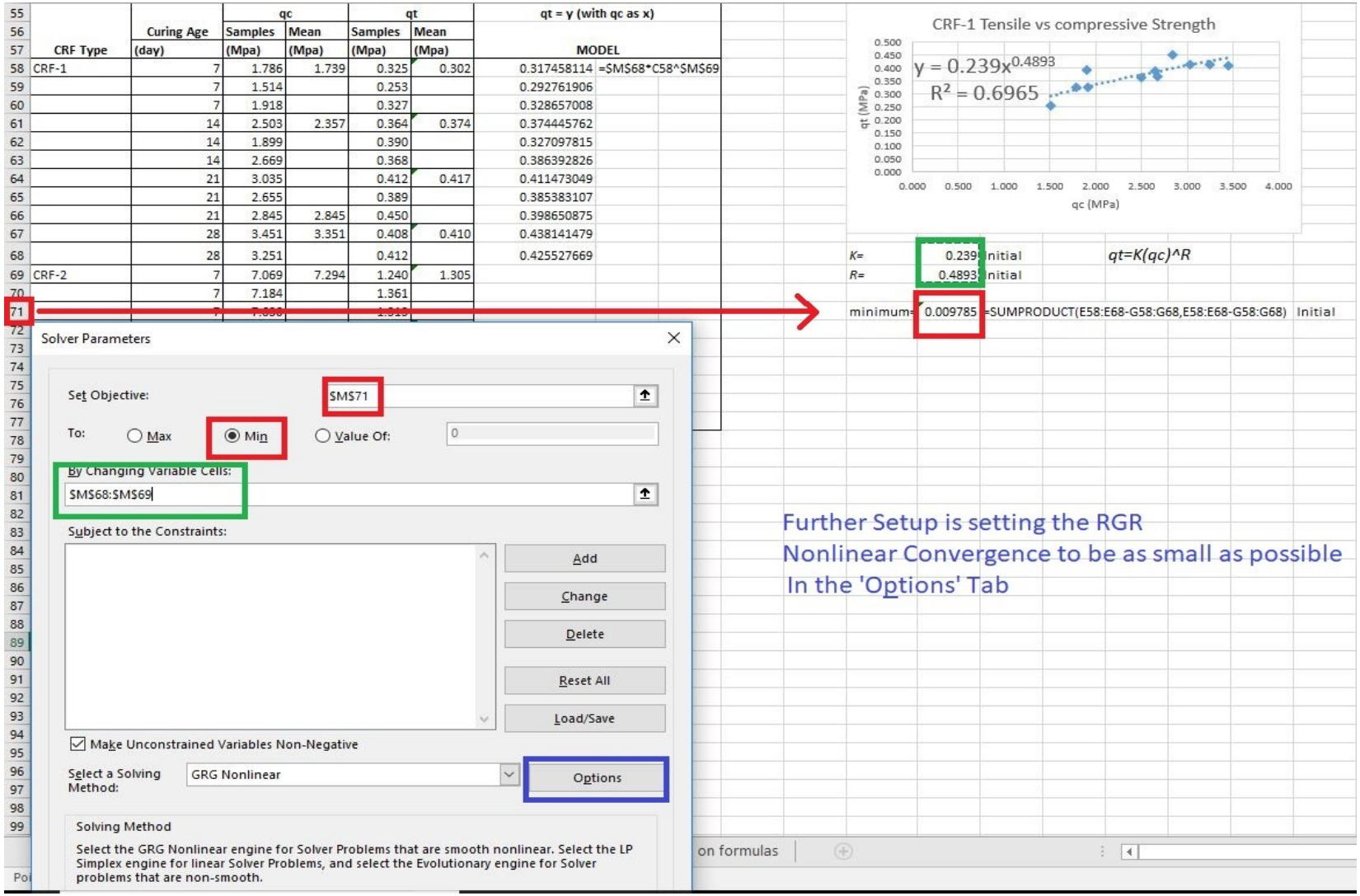

	CRF Type	Curing Age (day)	qc Samples (Mpa)	qc Mean (Mpa)	qt Samples (Mpa)	qt Mean (Mpa)	qt = y (with qc as x) MODEL
58	CRF-1	7	1.786	1.739	0.325	0.302	0.317458114 =$M$68*C58^$M$69
59		7	1.514		0.253		0.292761906
60		7	1.918		0.327		0.328657008
61		14	2.503	2.357	0.364	0.374	0.374445762
62		14	1.899		0.390		0.327097815
63		14	2.669		0.368		0.386392826
64		21	3.035		0.412	0.417	0.411473049
65		21	2.655		0.389		0.385383107
66		21	2.845	2.845	0.450		0.398650875
67		28	3.451	3.351	0.408	0.410	0.438141479
68		28	3.251		0.412		0.425527669
69	CRF-2	7	7.069	7.294	1.240	1.305	
70		7	7.184		1.361		

Step 4

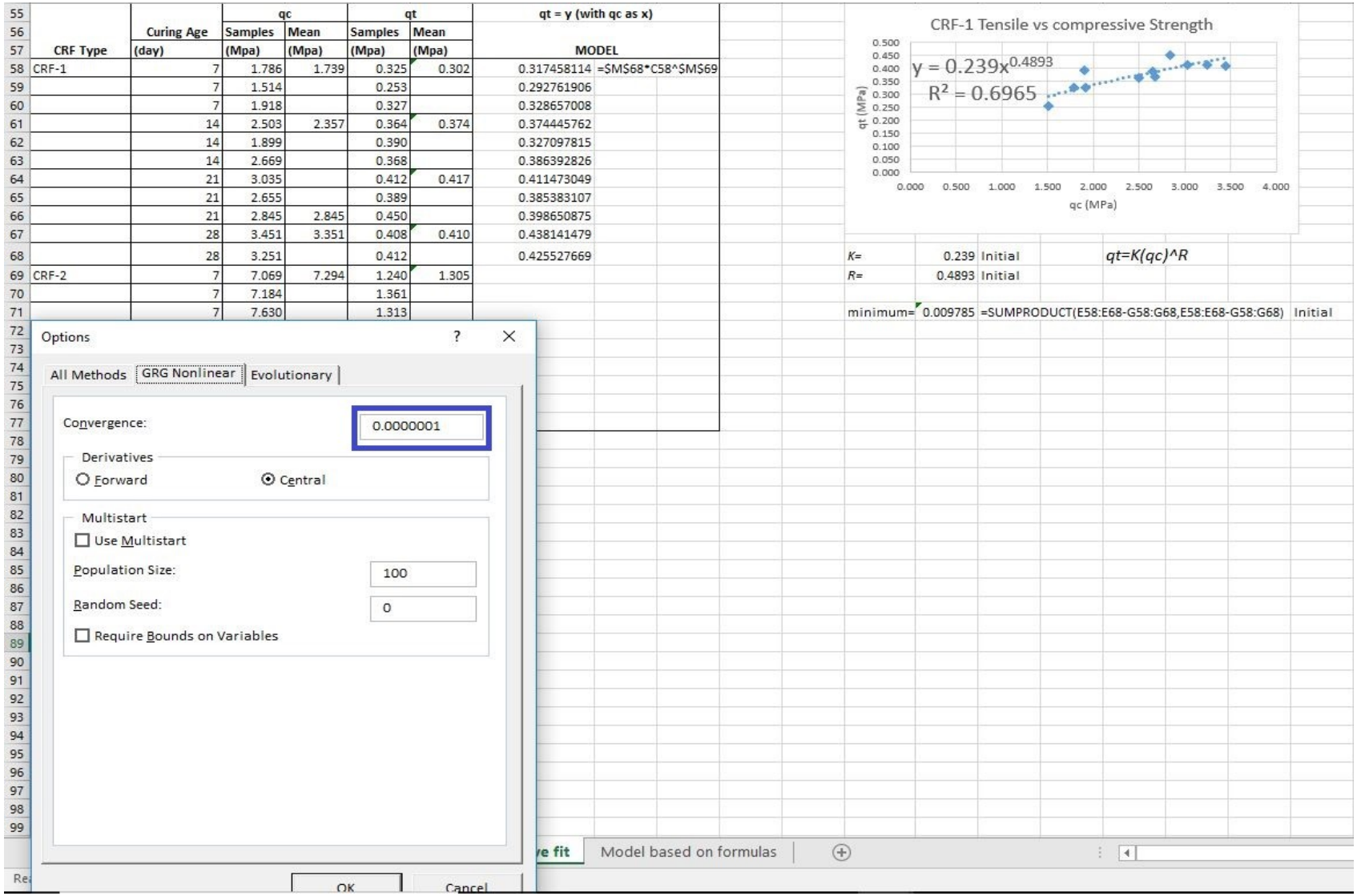

	Curing Age	qc Samples	qc Mean	qt Samples	qt Mean	qt = y (with qc as x)
CRF Type	(day)	(Mpa)	(Mpa)	(Mpa)	(Mpa)	MODEL
CRF-1	7	1.786	1.739	0.325	0.302	0.317458114 =$M$68*C58^$M$69
	7	1.514		0.253		0.292761906
	7	1.918		0.327		0.328657008
	14	2.503	2.357	0.364	0.374	0.374445762
	14	1.899		0.390		0.327097815
	14	2.669		0.368		0.386392826
	21	3.035		0.412	0.417	0.411473049
	21	2.655		0.389		0.385383107
	21	2.845	2.845	0.450		0.398650875
	28	3.451	3.351	0.408	0.410	0.438141479
	28	3.251		0.412		0.425527669
CRF-2	7	7.069	7.294	1.240	1.305	
	7	7.184		1.361		
	7	7.630		1.313		

K=	0.239	Initial	qt=K(qc)^R
R=	0.4893	Initial	
minimum=	0.009785	=SUMPRODUCT(E58:E68-G58:G68,E58:E68-G58:G68)	Initial

Options

All Methods | GRG Nonlinear | Evolutionary

Convergence: 0.0000001

Derivatives
Forward Central

Multistart
Use Multistart
Population Size: 100
Random Seed: 0
Require Bounds on Variables

OK Cancel

Model based on formulas

Step 5: Result

	Curing Age	qc		qt		qt = y (with qc as x)
		Samples	Mean	Samples	Mean	
CRF Type	(day)	(Mpa)	(Mpa)	(Mpa)	(Mpa)	MODEL
CRF-1	7	1.786	1.739	0.325	0.302	0.323127589 =$M$68*C58^$M$69
	7	1.514		0.253		0.300117881
	7	1.918		0.327		0.333509231
	14	2.503	2.357	0.364	0.374	0.375645138
	14	1.899		0.390		0.332065709
	14	2.669		0.368		0.386562463
	21	3.035		0.412	0.417	0.409385775
	21	2.655		0.389		0.385640933
	21	2.845	2.845	0.450		0.397733193
	28	3.451	3.351	0.408	0.410	0.43352077
	28	3.251		0.412		0.422121822
CRF-2	7	7.069	7.294	1.240	1.305	
	7	7.184		1.361		
	7	7.630		1.313		

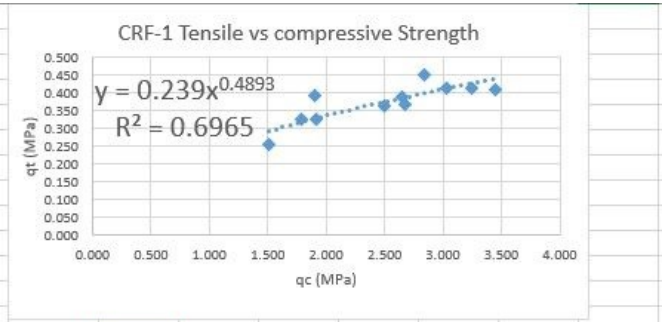

K=	0.249411	qt=K(qc)^R
R=	0.446317	
minimum=	0.009605	=SUMPRODUCT(E58:E68-G58:G68,E58:E68-G58:G68)

Solver Results

Solver found a solution. All Constraints and optimality conditions are satisfied.

Reports: Answer, Sensitivity, Limits

(•) Keep Solver Solution

( ) Restore Original Values

☐ Return to Solver Parameters Dialog ☐ Outline Reports

OK | Cancel | Save Scenario...

Solver found a solution. All Constraints and optimality conditions are satisfied.

When the GRG engine is used, Solver has found at least a local optimal solution. When Simplex LP is used, this means Solver has found a global optimal solution.

Solver tools give slightly 'minimum' value from initially 0.00978 to become 0.009605 with the new K and R value

this K and R value is used in the thesis equation (eq. 3.6) istead of the initial from trendline tool.

This procedure is repeated for CRF-2 as well

Appendix of Chapter 4

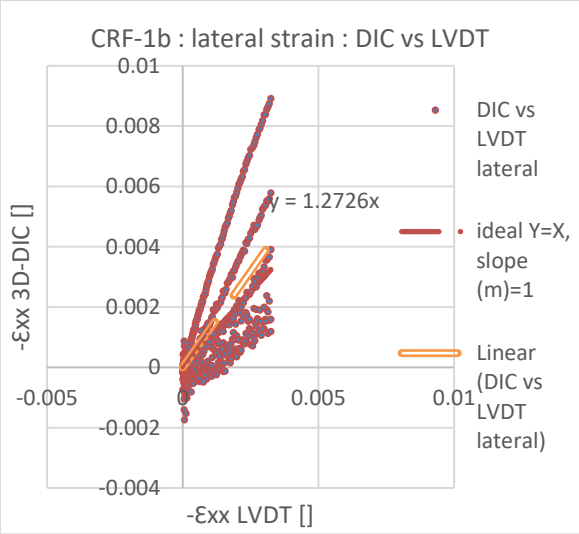

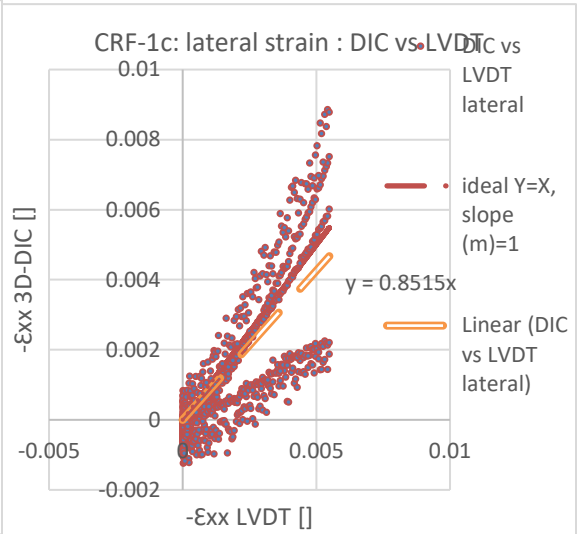

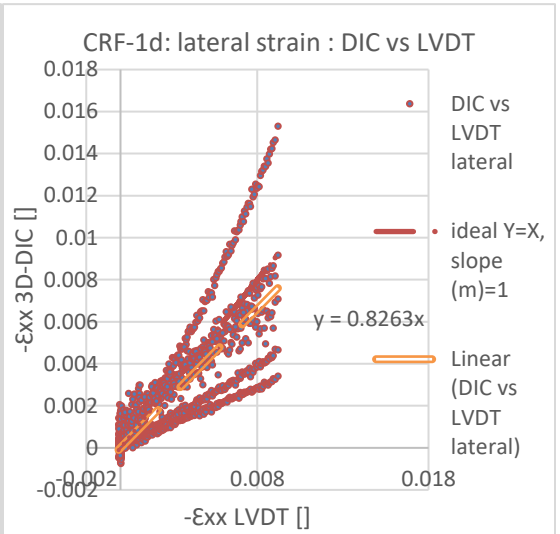

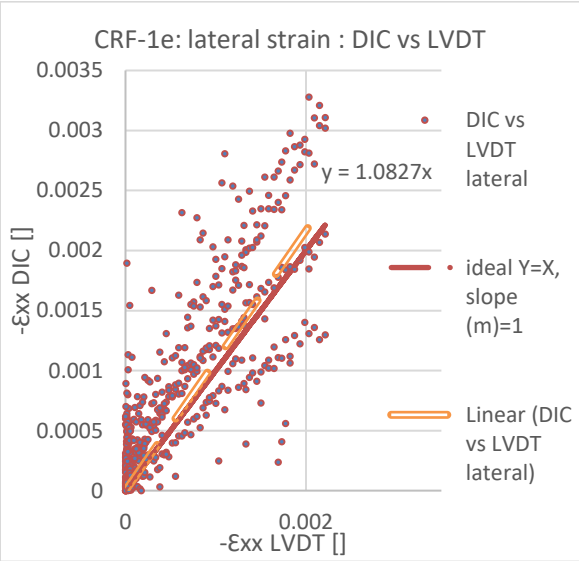

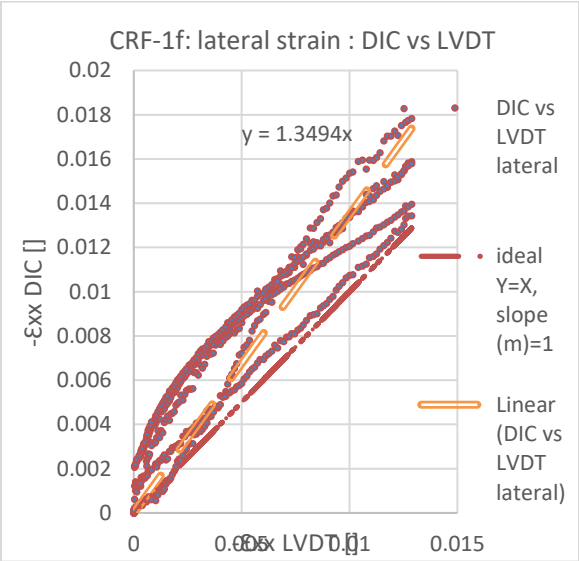

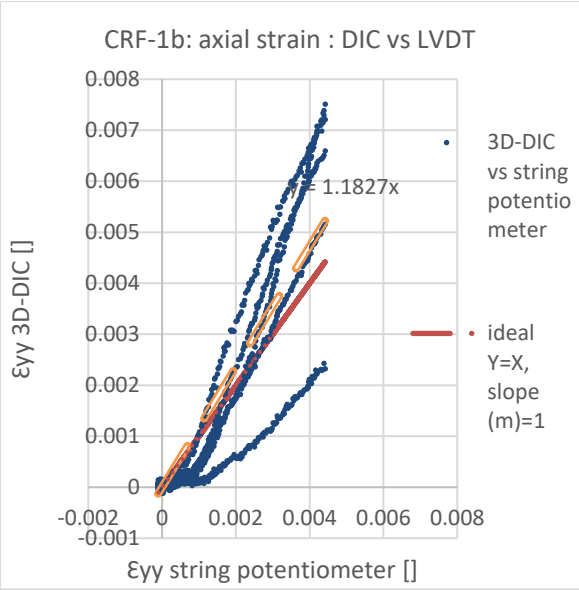
CRF-1b: axial strain : DIC vs LVDT
y = 1.1827x
Εyy 3D-DIC []
Εyy string potentiometer []
3D-DIC vs string potentiometer
ideal Y=X, slope (m)=1

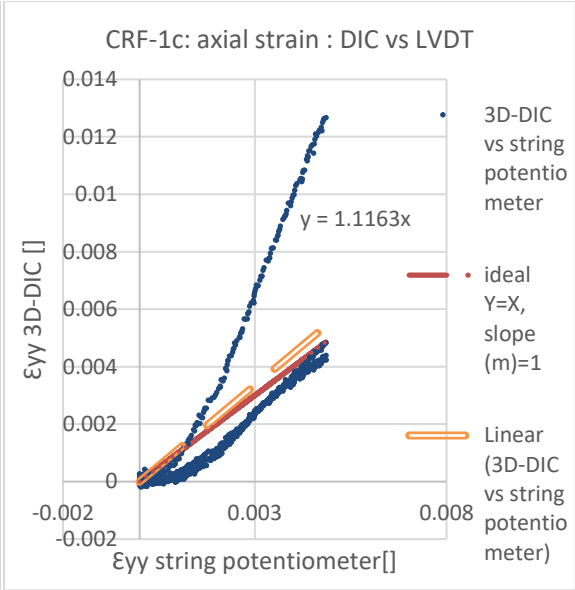
CRF-1c: axial strain : DIC vs LVDT
y = 1.1163x
Εyy 3D-DIC []
Εyy string potentiometer[]
3D-DIC vs string potentiometer
ideal Y=X, slope (m)=1
Linear (3D-DIC vs string potentiometer)

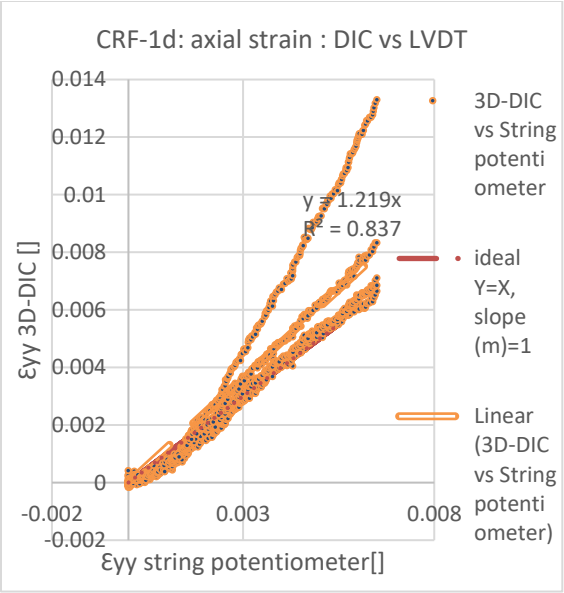
CRF-1d: axial strain : DIC vs LVDT
y = 1.219x
R² = 0.837
Εyy 3D-DIC []
Εyy string potentiometer[]
3D-DIC vs String potentiometer
ideal Y=X, slope (m)=1
Linear (3D-DIC vs String potentiometer)

Appendix of Chapter 5

RocData

4.5% CRF UCS and Triaxial Plotting

Project Summary

File Name RocData 4.5% CRF
File Version 5.007

Project Title 4.5% CRF UCS and Triaxial Plotting
Date Created 6/19/2017, 3:28:20 PM

General Settings

Stress Units MPa
Strength Criterion Mohr-Coulomb

Failure Criterion

	cohesion (MPa)	ϕ (°)	----	tensile strength (MPa)	σ_c (MPa)	alpha (°)
4.5% CRF	0.761122	45.903		0	3.76	80.68

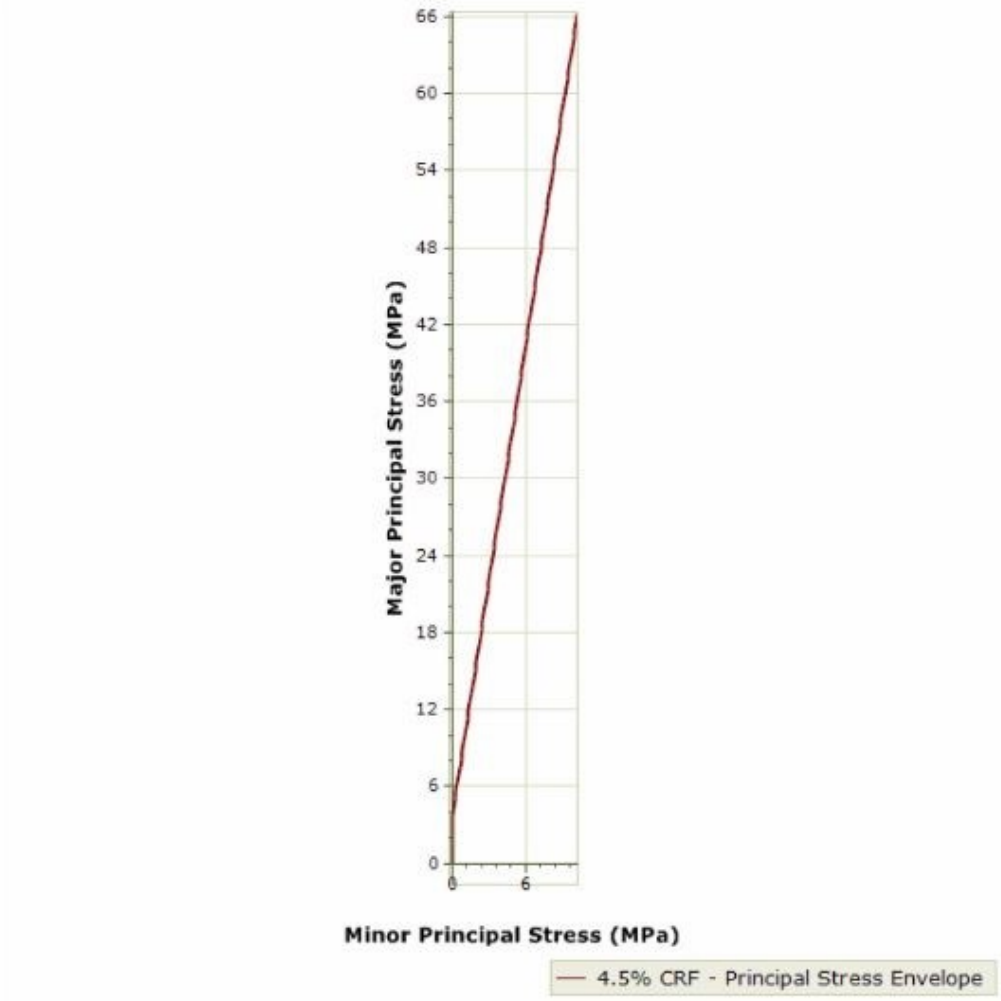
66
60
54
48
42
36
30
24
18
12
6
0
Major Principal Stress (MPa)
0
6
Minor Principal Stress (MPa)
4.5% CRF - Principal Stress Envelope

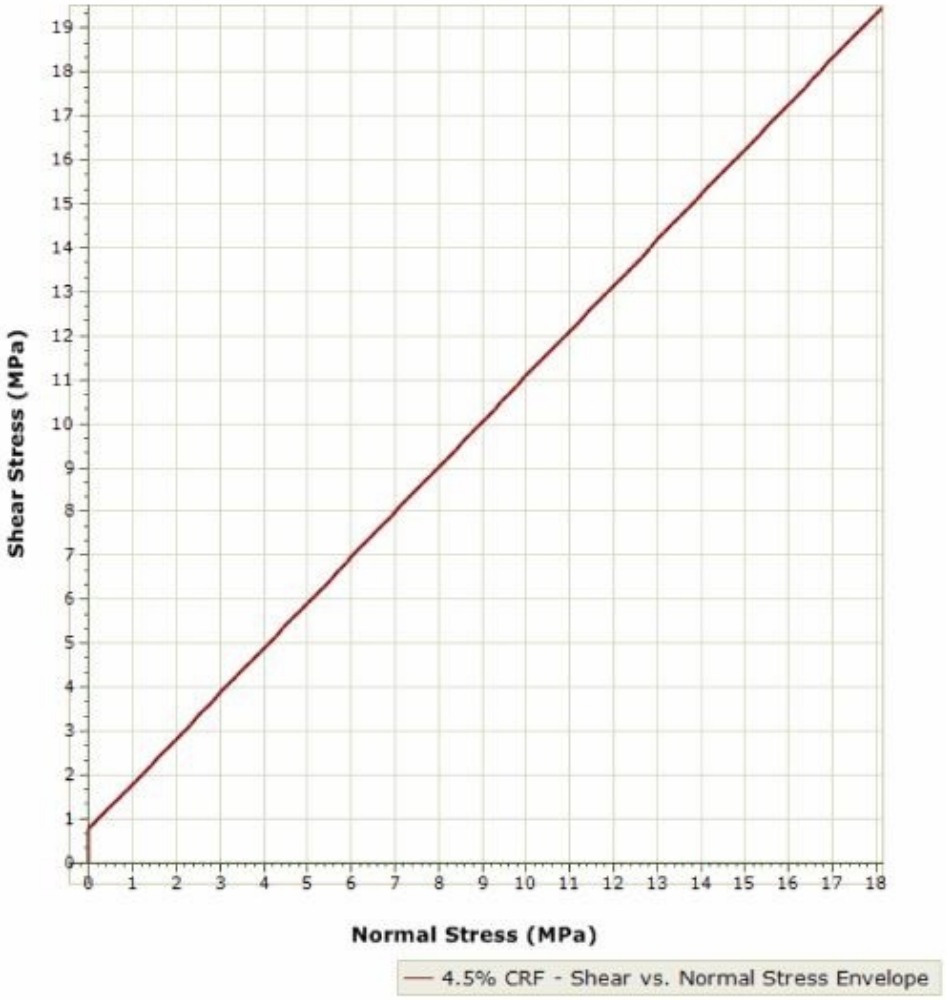

Lab Data

Curve Fit Results

	ϕ (°)	cohesion (MPa)	σ_t (MPa)	residuals
4.5% CRF	45.9	0.76	0	1.27

Curve Fit Method

	fit algorithm	error summation	error type
4.5% CRF	Levenberg Marquardt	vertical	absolute

Data Points

	σ_3 (MPa)	σ_1 (MPa)	Exclude
4.5% CRF	0	3.39	no
	0.74	8.55	no
	1.05	10.93	no
	1.49	12.16	no

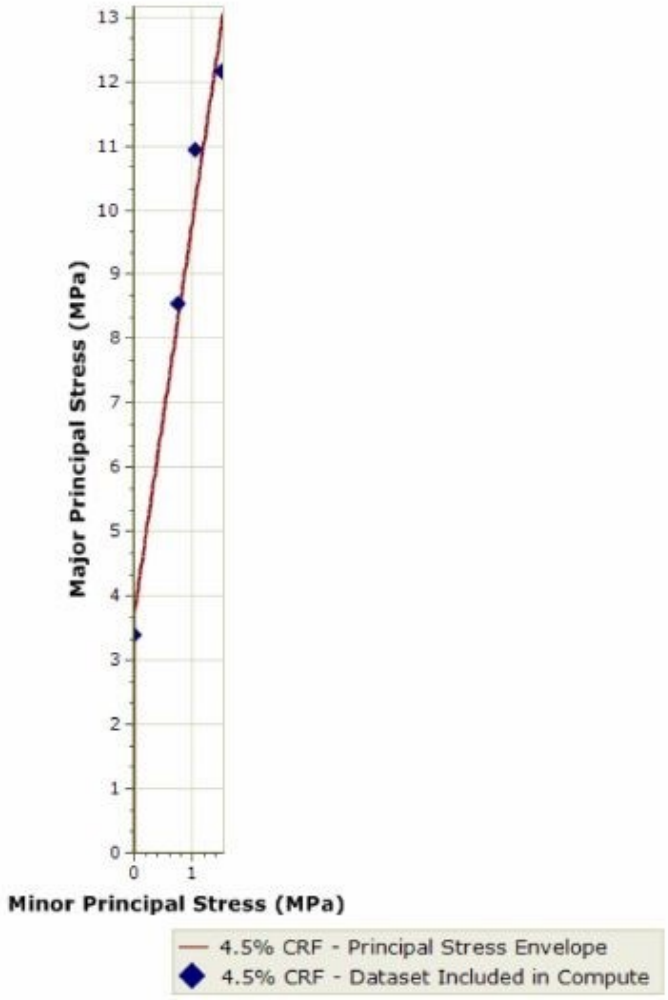

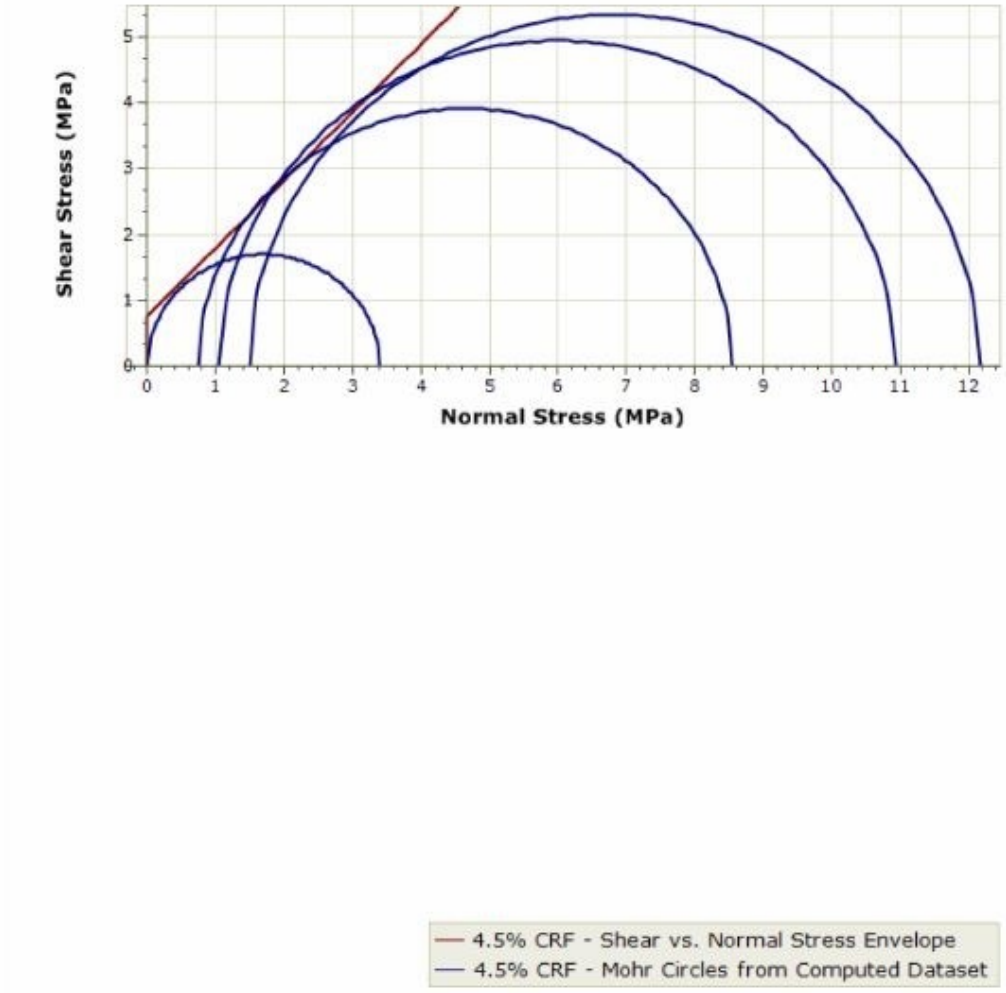
Shear Stress (MPa)
Normal Stress (MPa)
0
1
2
3
4
5
6
7
8
9
10
11
12
4.5% CRF - Shear vs. Normal Stress Envelope
4.5% CRF - Mohr Circles from Computed Dataset

RocData

10.5% CRF UCS and Triaxial plotting

Project Summary

File Name RocData 10.5% CRF Ei value=2GPa
File Version 5.006

Project Title 10.5% CRF UCS and Triaxial plotting
Date Created 7/31/2017, 1:30:17 PM

General Settings

Stress Units MPa
Strength Criterion Mohr-Coulomb

Failure Criterion

	cohesion (MPa)	ϕ (°)	----	tensile strength (MPa)	σ_c (MPa)	alpha (°)
10.5% CRF	2.16321	42.78		0	9.9	79.18

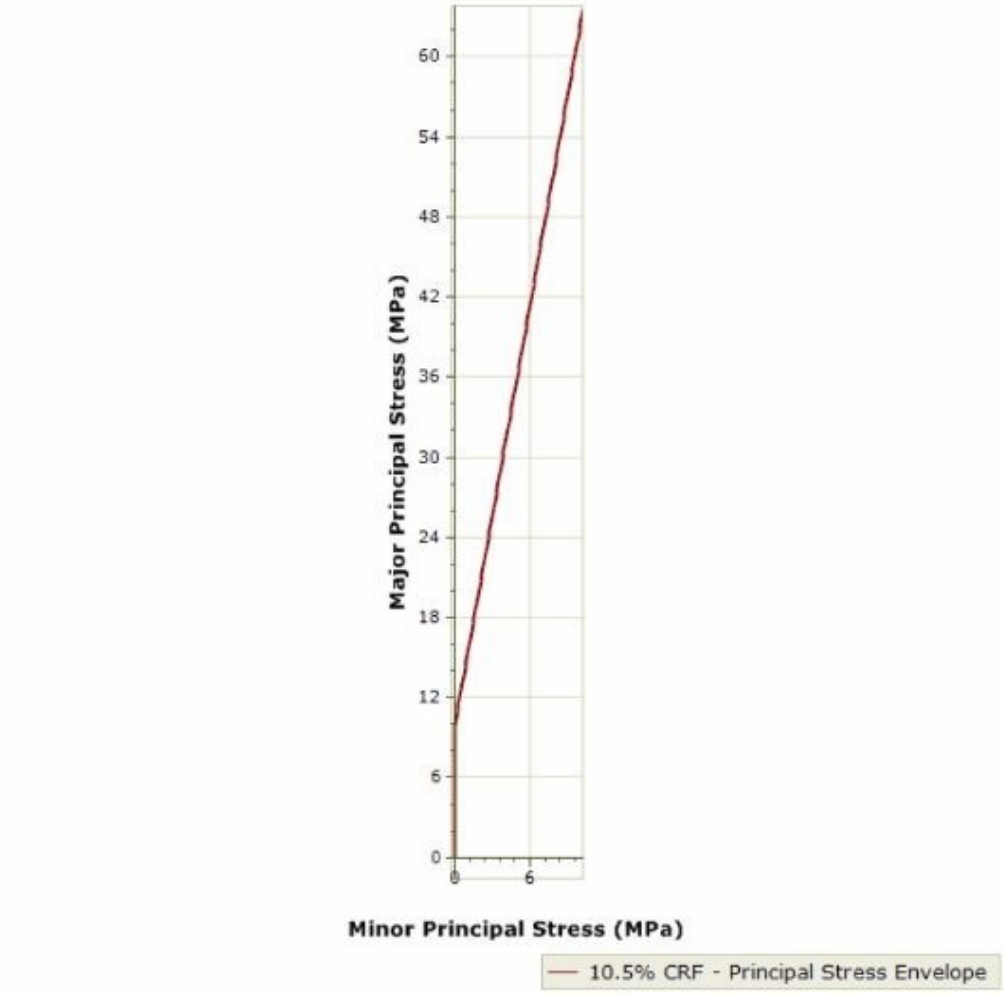
Major Principal Stress (MPa)
60
54
48
42
36
30
24
18
12
6
0
0
6
Minor Principal Stress (MPa)
10.5% CRF - Principal Stress Envelope

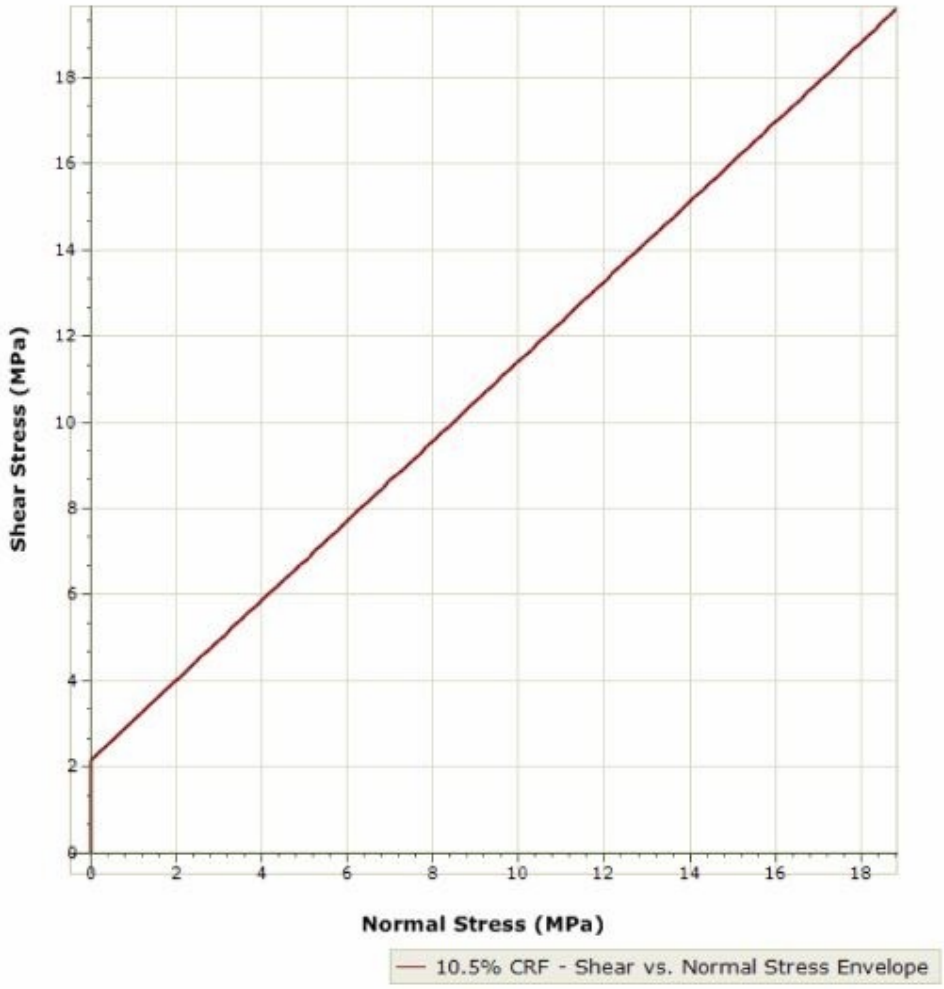

Lab Data

Curve Fit Results

	ϕ (°)	cohesion (MPa)	σ_t (MPa)	residuals
10.5% CRF	42.78	2.16	0	4.55

Curve Fit Method

	fit algorithm	error summation	error type
10.5% CRF	Levenberg Marquardt	vertical	absolute

Data Points

	σ_3 (MPa)	σ_1 (MPa)	Exclude
10.5% CRF	0	9.22	no
	1.49	19.41	no
	2.57	22.24	no
	3.49	28.25	no

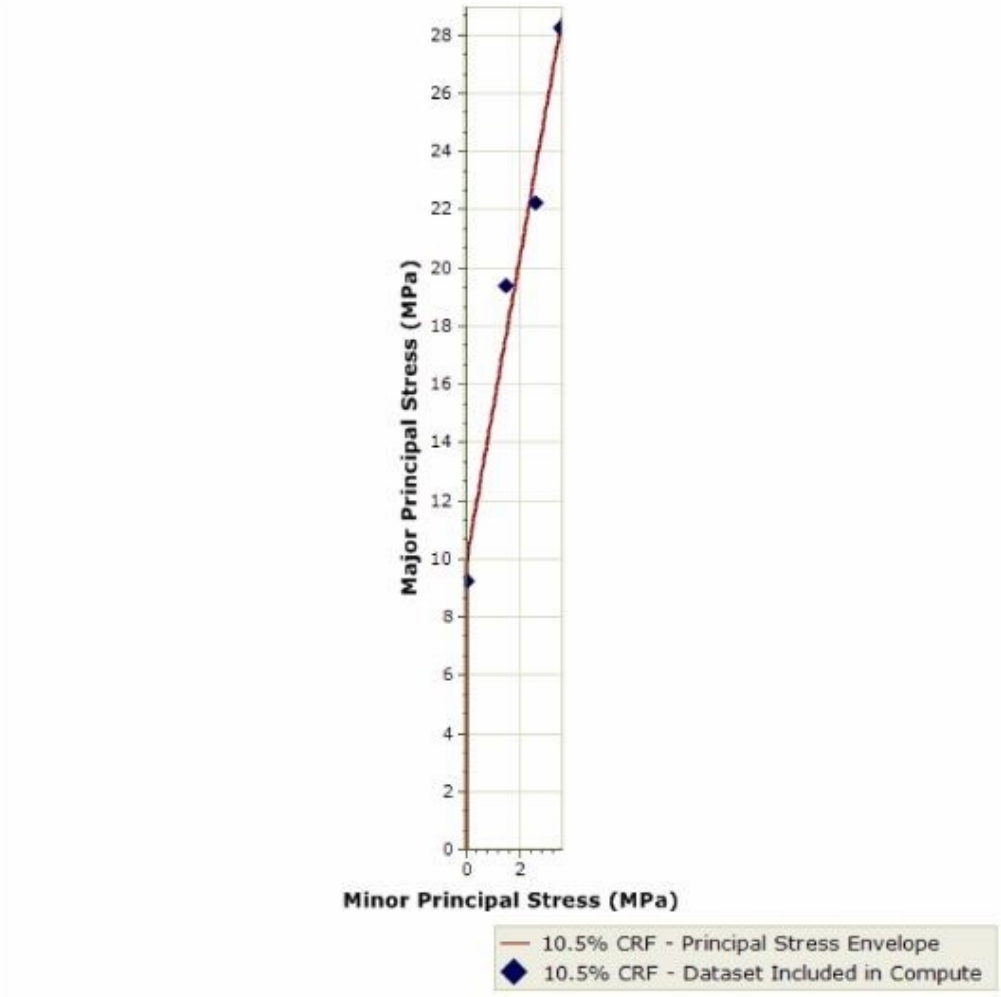

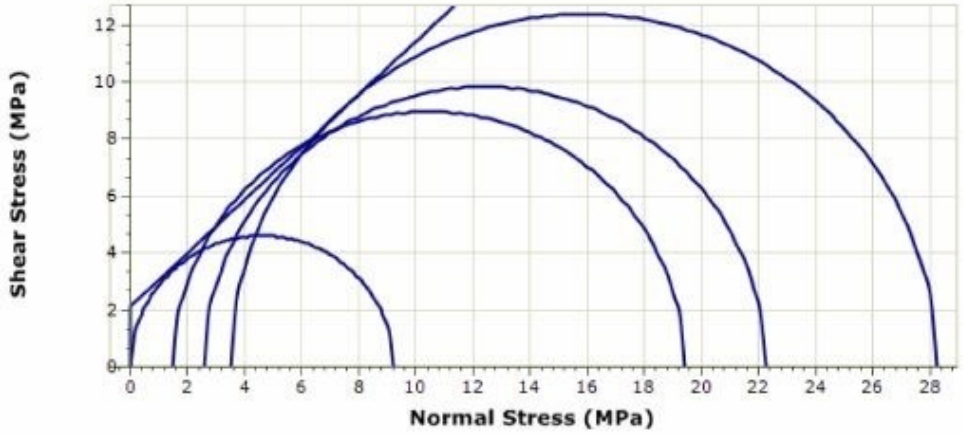

10.5% CRF - Shear vs. Normal Stress Envelope
10.5% CRF - Mohr Circles from Computed Dataset